Czech Technical University in Prague
Faculty of Civil Engineering
Department of Mechanics

Ing. Edita Dvořáková

Isogeometric analysis of beam structures

Doctoral thesis

Ph.D. Programme: Civil Engineering

Branch of study: Structural and Transportation Engineering

Supervisor: prof. Dr. Ing. Daniel Rypl

Supervisor - specialist: prof. Dr. Ing. Bořek Patzák

Prague, February 2022

CZECH TECHNICAL UNIVERSITY IN PRAGUE
Faculty of Civil Engineering
Thákurova 7, 166 29 Praha 6

DECLARATION

Ph.D. student's name: Ing. Edita Dvořáková

Title of the doctoral thesis: Isogeometric analysis of beam structures

I hereby declare that this doctoral thesis is my own work and effort written under the guidance of the supervisors Daniel Rypl and Bořek Patzák.
All sources and other materials used have been quoted in the list of references.

The doctoral thesis was written in connection with research on the projects: SGS16/038/OHK1/1T/11, SGS17/043/OHK1/1T/11, SGS18/037/OHK1/1T/11, SGS19/032/OHK1/1T/11, SGS20/038/OHK1/1T/11, and SGS21/037/OHK1/1T/11

In Prague on .....

.....
signature

Acknowledgements

I would like to thank Daniel Rypl, for the help with the thesis and plenty of valuable notes and advice. Thank you goes also to Bořek Patzák, for all the guidance, support and encouragement. Thank Martin Horák for always having time to help. In the spirit of the motto "the journey is the destination", I would like to acknowledge all my colleagues, friends, coffee girls and running mates for making the studies one of my favourite times of life. Last but not least, thank my family, who supported me through my whole studies.

Název: Izogeometrická analýza nosníkových konstrukcí

Autor: Ing. Edita Dvořáková

Katedra: Katedra mechaniky

Školitel: prof. Dr. Ing. Daniel Rypl

Školitel-specialista: prof. Dr. Ing. Bořek Patzák

Abstrakt Izogeometrická analýza je nová koncepce v metodě konečných prvků, která byla navržena k překlenutí propasti mezi Computer-aided design (CAD) systémy a konečně-prvkovými (MKP) řešiči. CAD modely převážně používají splinové bázové funkce, zatímco standardní MKP řešiče jsou obvykle založeny na polynomiálních bázových funkcích. Tento rozdíl znemožňuje přímou komunikaci mezi CAD a MKP modely a transformace z jednoho do druhého vedou ke ztrátám přesnosti a značné časové náročnosti. V izogeometrické analýze se spline bázové funkce používají jak pro popis geometrie, tak pro aproximace neznámých, a proto lze mezi CAD a MKP modely sdílet stejnou reprezentaci geometrie.

Tato práce se zaměřuje na aplikace izogeometrické analýzy na konstrukce se zakřivenou geometrií. Jsou zde uvedeny formulace několika izogeometrických nosníkových prvků a demonstrována jejich výkonnost. Originálním přínosem práce je nová metoda řešící popis koncentrovaných zatížení pro nosníky s přímou i zakřivenou geometrií. Získané výsledky prokazují schopnost a přiměřenost metody a motivují k dalšímu výzkumu tohoto tématu.

Klíčová slova: izogeometrická analýza, NURBS, zakřivené nosníky, koncentrované zatížení

Title: Isogeometric analysis of beam structures

Author: Ing. Edita Dvořáková

Department: Department of Mechanics

Supervisor: prof. Dr. Ing. Daniel Rypl

Supervisor-specialist: prof. Dr. Ing. Bořek Patzák

Abstract Isogeometric analysis is a new concept in finite element method (FEM) which has been proposed to bridge the gap between the computer-aided design (CAD) systems and the FEM solvers. The CAD models use mostly the spline basis functions, while the standard FEM solvers are usually based on the polynomial basis functions. This difference prevents direct communication between the CAD and FEM models and the transformations from one to another lead to accuracy losses and significant time consumption. In isogeometric analysis, the spline basis functions are used for both geometry description and unknown approximations and thus the same geometry representation may be shared between CAD and FEM models.

This thesis focuses on the applications of isogeometric analysis to structures with complex curved geometries. Formulations of several isogeometric beam elements are presented and their performance is demonstrated. The original contribution of the thesis is a novel method addressing the resolution of concentrated loadings for beams with both straight and curved geometry. The obtained results demonstrate the capability and adequacy of the method and empower further research on this topic.

Keywords: isogeometric analysis, NURBS, curved beams, concentrated loadings

CONTENTS

CHAPTER

ONE

INTRODUCTION

The current civil engineering design depends predominantly on two essential technologies. Firstly, it is a computer-aided design (CAD) technology that serves as an instrument for an architect to precisely describe and share his ideas. Using CAD, the architect can basically build the structure virtually and pass the model to a structural engineer, who in the second indispensable part of the design process uses finite element analysis (FEA). Finite element solvers allow for the assessment of the designed structure. Based on the calculations, it can be decided whether (and under which circumstances) the structure is reliable or not. Both CAD and FEA together, help to bring the structure, which initially exists only in the architect's imagination, to life.

Both technologies have been introduced in the middle of 20^{th} century [1–4] and significant developments have been done in both fields over the past decades. However, due to the independent development, there are fundamental differences in the geometry description causing the inability of automatic mutual communication. With the rising expectations on the accuracy and efficiency of the overall design process, this gap is increasingly perceived as a problem. Moreover, several research areas with promising theoretical results (e.g. optimization or contact mechanics) fail to be fully implemented in the practice, either due to the lack of communication between CAD and FEA or because of the approximation errors in a finite element model.

To provide a seamless connection between CAD and FEA, isogeometric analysis (IGA) was introduced by T. Hughes [5] in 2005. This new methodology proposes to proceed with the analysis directly on a CAD model thus the geometry approximation differences are eliminated. Additionally, due to the shared geometry description, the communication between design and analysis is straightforward. The use of a single model for both processes is facilitated by switching from polynomials standardly used in FEA for geometry and unknown approximations to the CAD basis functions - "splines".

Despite the promising prospects of the isogeometric approach, its implementation is not always straightforward. Usually, the the procedures used in standard FEA need to be adjusted or even the new ones developed. As the strong effort of many research groups has been taken since its introduction, IGA has been successfully applied to a

wide range of engineering problems and in many cases, it has shown superior performance over standard FEA. Optimization problems [6] profit from the easy communication between the design and the analysis stages. The exact geometrical model (as far as the CAD model is concerned) is especially convenient for the analysis of contact problems [7], as well as in the analysis of fluids [8], and fluid-structure interactions [9]. Modeling of curved geometries such as beams [10–14] and shells [15, 16] also undoubtedly benefits from the exact CAD geometrical description.

This thesis is focused on the application of IGA to the analysis of beam structures. Thanks to the isogeometric approach, the arbitrarily-curved geometries can be analyzed with no loss of accuracy caused by the geometry approximation. Moreover, basis functions used in IGA provide higher continuity than C^0 typically provided by polynomials used in standard FEA. This is especially convenient for Bernoulli beam formulations, where at least C^1 continuity is required [17].

Timoshenko theory-based isogeometric beam elements have been studied quite extensively. The main topic of most of the works concerning Timoshenko beams is numerical locking, which is a well-known problem of Timoshenko theory in standard FEA and can be also observed in IGA. In [11] the problem of locking phenomena is documented on an example of NURBS-based Timoshenko beam element and treatment based on discrete shear gap method (DSG) is proposed. Strategies of selective reduced integration and $\bar{\mathrm{B}}$ method are studied in [10]. Authors claim that the attractivity of selective reduced integration caused by simple implementation and low computational cost is outweighed by the difficult generalization of the integration rules for arbitrary polynomial order and continuity. Their implementation of $\bar{\mathrm{B}}$ method-based element was derived using concept presented in [18] and showed promising results in alleviating a locking. In [19, 20] the possibilities of the collocation method are studied for both displacement-based and mixed formulations. In the context of collocation methods, the authors proved that mixed formulations are locking-free while locking in the displacement-based formulation must be avoided using higher-order approximation. Coupling of membrane and bending actions in strongly curved beams is studied in [21]. A single-variable formulation of Timoshenko beam using deflection as primary unknown is provided in [22]. Only a few works consider a geometrically nonlinear analysis of curved beams [22–25].

An isogeometric approach can also facilitate the analysis of Bernoulli beams. While the use of Bernoulli elements in standard FEA is limited due to the necessity of satisfying higher inter-element continuity than usually provided C^0, the required continuity along an entire computational domain is naturally provided by NURBS basis functions used in IGA. Nonlinear dynamic analysis of spatial Bernoulli beams studied in [26] neglects the torsional actions. Element considering translational displacements as well as the torsional rotation can be found in [13] and the further extension of this concept to geometrically nonlinear analysis of beams is provided in [14]. Planar flexible beam structures with snap-back are studied in [27]. The influence of large curvatures on the analysis is covered in [28].

Although the advantages brought to the analysis of curved beams by an exact and smooth geometrical description are indisputable, further investigation is needed in

some areas. Bernoulli beam formulations suffer from the difficulties of enforcement of rotational boundary conditions or rigid connections between patches. A possible solution to this problem is addressed e.g. in [29], where a polar decomposition of the deformation of the first and last segments of the control polygon is used to introduce directly the end rotations as degrees of freedom. In some cases, the problem with enforcement of a rotational boundary condition can be solved by modeling the whole domain using a single patch where continuity is easily provided. Nevertheless, the continuous basis functions fail to represent the discontinuities in the numerical solution when a beam is subjected to the effect of concentrated loading within a patch. This failure is present in both Bernoulli and Timoshenko beam formulations and is hardly acceptable in engineering practice since a traditional deformation method for beams is capable of delivering exact internal force diagrams.

With consideration of the recent achievements in the isogeometric analysis of curved beams, the following goals of the presented thesis have been set:

1. Implement linear and nonlinear isogeometric formulations for both straight and curved beam geometries.

2. Evaluate the performance of different locking-removal techniques.

3. Propose a method for overcoming the problem of concentrated loadings.

While the first two goals are using the results provided in the available publications, the possibilities for improvement of the numerical response under concentrated loading within the domain for isogeometric elements have not been addressed before. Nevertheless, all the steps are necessary for deep insight and a full understanding of the studied problematics.

In the presented thesis, a brief introduction to the finite element analysis is provided first, followed by the introduction of NURBS basis functions and a discussion of the specifics of isogeometric analysis using the NURBS basis. In the third chapter, both Timoshenko and Bernoulli beam formulations are provided along with the numerical examples on which the performance of the implemented formulations is evaluated. Moreover, implementation including the development of an input file generator and an interactive design tool prototype is discussed within this chapter. In the fourth chapter, the problem of concentrated loading is demonstrated and possible solutions, including a novel method, are proposed. Finally, the conclusions are drawn in the last chapter.

CHAPTER

TWO

ISOGEOMETRIC ANALYSIS

Isogeometric analysis has been developed with the aim to break the barrier between CAD and FEA. Sharing one, and only one, geometrical model between the design and the analysis came up to be a key idea. The decision had to be made, whether to preserve the CAD model and use it also for the analysis or vice versa. The first option has appeared to be more convenient as there are several very efficient and highly-developed technologies available for the geometrical representation in the CAD industry. Moreover, these technologies are able to exactly describe shapes which could be only approximated with the polynomial approximation typically used for the FEA.

Probably the most widespread and developed technology for CAD data representation are Non-Uniform Rational B-Splines (NURBS) [30, 31]. Over years many efficient and numerically stable algorithms have been developed to generate and manipulate NURBS objects. For their ability to exactly represent various curved shapes, including all conic sections, and for their predominancy in the CAD industry, NURBS have been chosen as the basis for the isogeometric analysis in this work.

Isogeometric analysis can be seen as an alternative to the standard Finite element analysis (FEA). The analysis procedures are analogical for both methods; the major difference between IGA and FEA lies in the basis functions used for the analysis. Therefore in this section, the brief introduction to FEA is given first, followed by the description of NURBS basis functions. Finally, the consequences of the use of different basis functions for the analysis are discussed.

2.1. Finite element analysis

Finite element method (FEM) is the most widespread numerical method used to solve engineering problems. It is applicable to a vast range of problems, e.g. static and dynamic structural analysis, the analysis of fluids and fluid-structure interactions, or transport problems. In addition to the general applicability, FEM is also relatively simple to implement, which makes the method very attractive for use in practice. The main idea of FEM is a discretization of the problem domain into disjunctive subdo-

mains (elements) and use of approximation functions with limited support.

In this work, the introduction to FEM based structural analysis is provided. The derivation starts from the principle of the virtual displacements stating that a system is in equilibrium if, for any virtual displacement vector $\delta\boldsymbol{u}$ satisfying kinematic boundary conditions and for a compatible virtual deformation vector $\delta\boldsymbol{\varepsilon}$, the virtual work of internal forces δW_{int} is equal to the virtual work of external forces δW_{ext} which can be expressed as

$$\underbrace{\int_V \delta\boldsymbol{\varepsilon}^T\boldsymbol{\sigma}dV}_{\delta W_{int}} = \underbrace{\int_V \delta\boldsymbol{u}^T\bar{\boldsymbol{X}}dV + \int_{\Gamma_p} \delta\boldsymbol{u}^T\bar{\boldsymbol{p}}d\Gamma_p}_{\delta W_{ext}}, \tag{2.1}$$

where $\boldsymbol{\sigma}$ is the stress vector, $\bar{\boldsymbol{X}}$ is the vector of body loads, and $\bar{\boldsymbol{p}}$ is the vector of boundary loads. Voight notation is adopted here [32]. The boundary Γ of the domain V can be divided into the part subjected to the boundary loads Γ_p and part with enforced kinematic constraints Γ_u. Assuming geometrically linear behavior, strain vector and displacement vector are tied by geometric relations in form

$$\boldsymbol{\varepsilon} = \boldsymbol{\partial}^T\boldsymbol{u}, \tag{2.2}$$

where $\boldsymbol{\partial}$ is the differential operator matrix. Further, linear constitutive relations between stress and strain vectors are assumed

$$\boldsymbol{\sigma} = \boldsymbol{D}\boldsymbol{\varepsilon}, \tag{2.3}$$

where $\boldsymbol{D}$ is material stiffness matrix.

Consequently, domain V is divided into the disjunctive subdomains V^e, where the approximation of displacement $\boldsymbol{u}^e$ in terms of a linear combination of the basis functions $\boldsymbol{N}^e$ and nodal values $\boldsymbol{r}^e$ is assumed

$$\boldsymbol{u}^e = \boldsymbol{N}^e\boldsymbol{r}^e. \tag{2.4}$$

Basis functions $\boldsymbol{N}^e$ must satisfy the conditions of continuity and completeness. By applying geometric relations (2.2) the relations for strain and virtual strain are expressed as

$$\boldsymbol{\varepsilon}^e = \boldsymbol{\partial}^T\boldsymbol{u}^e = \boldsymbol{\partial}^T\boldsymbol{N}^e\boldsymbol{r}^e = \boldsymbol{B}^e\boldsymbol{r}^e, \tag{2.5}$$

$$\delta\boldsymbol{\varepsilon}^e = \boldsymbol{\partial}^T\delta\boldsymbol{u}^e = \boldsymbol{\partial}^T\boldsymbol{N}^e\delta\boldsymbol{r}^e = \boldsymbol{B}^e\delta\boldsymbol{r}^e, \tag{2.6}$$

where $\boldsymbol{B}^e = \boldsymbol{\partial}^T\boldsymbol{N}^e$ is a matrix containing the derivatives of the basis functions.

By substitution of the relations (2.5, 2.6) to the principle of virtual displacements (2.1) and by replacing the integral over the domain by the sum of the integrals over the individual subdomains (elements) the following relation is obtained

$$\sum_{e=1}^{n}\left\{\int_{V^e}\delta\boldsymbol{r}^{eT}\boldsymbol{B}^{eT}\boldsymbol{D}\boldsymbol{B}^e\boldsymbol{r}^e\,dV^e - \int_{V^e}\delta\boldsymbol{r}^{eT}\boldsymbol{N}^{eT}\boldsymbol{X}^e\,dV^e - \int_{\Gamma_p^e}\delta\boldsymbol{r}^{eT}\boldsymbol{N}^{eT}\boldsymbol{p}^e\,d\Gamma_p^e\right\} = \boldsymbol{0}, \tag{2.7}$$

where $\delta\boldsymbol{r}^e$ can be factored out

$$\sum_{e=1}^{n}\left\{\delta\boldsymbol{r}^{eT}\left(\int_{V^e}\boldsymbol{B}^{eT}\boldsymbol{D}\boldsymbol{B}^e\boldsymbol{r}^e\,dV^e - \int_{V^e}\boldsymbol{N}^{eT}\boldsymbol{X}^e\,dV^e - \int_{\Gamma_p^e}\boldsymbol{N}^{eT}\boldsymbol{p}^e\,d\Gamma_p^e\right)\right\} = \boldsymbol{0}. \tag{2.8}$$

Subsequently, local vectors $\boldsymbol{r}^e$ and $\delta\boldsymbol{r}^e$ can be expressed using localization matrix $\boldsymbol{L}^e$ and global vectors $\boldsymbol{r}$ and $\delta\boldsymbol{r}$ as $\boldsymbol{r}^e = \boldsymbol{L}^e\boldsymbol{r}$ and $\delta\boldsymbol{r}^e = \boldsymbol{L}^e\delta\boldsymbol{r}$, respectively, which yields

$$\delta\boldsymbol{r}^T \sum_{e=1}^{n} \boldsymbol{L}^{eT} \left\{ \int_{V^e} \boldsymbol{B}^{eT}\boldsymbol{D}\boldsymbol{B}^e\boldsymbol{L}^e\boldsymbol{r}\, dV^e - \int_{V^e} \boldsymbol{N}^{eT}\boldsymbol{X}^e\, dV^e - \int_{\Gamma_p^e} \boldsymbol{N}^{eT}\boldsymbol{p}^e\, d\Gamma_p^e \right\} = \boldsymbol{0}. \tag{2.9}$$

The above equation has to be satisfied for all $\delta\boldsymbol{r} \neq 0$ and thus

$$\sum_{e=1}^{n} \boldsymbol{L}^{eT} \left\{ \int_{V^e} \boldsymbol{B}^{eT}\boldsymbol{D}\boldsymbol{B}^e\boldsymbol{L}^e\boldsymbol{r}\, dV^e - \int_{V^e} \boldsymbol{N}^{eT}\boldsymbol{X}^e\, dV^e - \int_{\Gamma_p^e} \boldsymbol{N}^{eT}\boldsymbol{p}^e\, d\Gamma_p^e \right\} = \boldsymbol{0}. \tag{2.10}$$

By factoring out $\boldsymbol{r}$ the final equation is obtained

$$\underbrace{\sum_{e=1}^{n} \boldsymbol{L}^{eT} \overbrace{\int_{V^e} \boldsymbol{B}^{eT}\boldsymbol{D}\boldsymbol{B}^e\, dV^e}^{\boldsymbol{K}^e} \boldsymbol{L}^e}_{\boldsymbol{K}^g} \boldsymbol{r} - \underbrace{\sum_{e=1}^{n} \boldsymbol{L}^{eT} \overbrace{\left\{ \int_{V^e} \boldsymbol{N}^{eT}\boldsymbol{X}^e\, dV^e + \int_{\Gamma_p^e} \boldsymbol{N}^{eT}\boldsymbol{p}^e\, d\Gamma_p^e \right\}}^{\boldsymbol{f}^e}}_{\boldsymbol{f}^g} = \boldsymbol{0}, \tag{2.11}$$

where $\boldsymbol{K}^e$ is the element stifness matrix, $\boldsymbol{f}^e$ is the element load vector, and $\boldsymbol{K}^g$ is the global stifness matrix, $\boldsymbol{f}^g$ is the global load vector.

2.2. B-spline and NURBS approximation

A special subset of NURBS functions are B-spline functions which are piecewise polynomials. NURBS functions are rational B-spline functions generated by weighting B-spline functions. From a geometric point of view NURBS entity in d–dimensional space is just a projection of B-spline entity in $(d+1)$–dimensional space. This way the conic sections such as elliptical entities can be described exactly.

In the following description, a one-dimensional domain in the parametric space is considered. In isogeometric analysis, the domain is firstly divided into patches, which are further divided into knot spans. The parametric space is local to patches. The vast number of academic problems can be modelled using only a single patch. Knot spans are often called elements in IGA as the numerical quadrature is usually carried out at the knot span level and this terminology is also adopted in this work. The partitioning of a patch into knot spans is defined by a knot vector

$$\Xi = \{\xi_1, ..., \xi_{n+p+1}\}, \tag{2.12}$$

which is a non-decreasing set of parametric coordinates of knots $\xi_i \in \mathbb{R}$, where i is the knot index. The size of a knot vector is equal to $n + p + 1$, where n is the number of basis functions used to construct a NURBS curve and p is the approximation degree. Note that in CAD terminology approximation degree differs from approximation order $o = p + 1$, nevertheless, in isogeometric analysis, these terms are often used synonymously ($o = p$) and this terminology is also adopted in this work.

Equally spaced knots in the parametric space form uniform knot vectors. On the contrary, knot vectors are called non-uniform, when the spacing differs. The repetition of the knot values is referred to as a knot multiplicity. This feature significantly influences the properties of the basis, as the continuity of basis functions between the knot spans is affected (see Section 2.3.3 for an illustrative example). When the first and the last knot values are repeated $p + 1$ times, the knot vector is said to be open [30]. An open knot vector features the interpolatory basis functions at the endpoints of the interval, while the basis functions are not, in general, interpolatory at interior knots. In this work, only open knot vectors are considered, as they are the standard in the CAD industry.

2.2.1. Basis functions

The formulation of B-spline functions starts with piecewise constant functions

$$N_{i,0}(\xi) = \begin{cases} 1 & \text{if } \xi_i \leq \xi < \xi_{i+1} \\ 0 & \text{otherwise} \end{cases}, \tag{2.13}$$

where ξ_i is the i^{th}-knot coordinate and ξ is a parametric coordinate that runs through the entire patch. The p^{th}-degree B-spline functions $N_{i,p}(\xi)$ are obtained using the Cox-de Boor recursion formula [30]

$$N_{i,p}(\xi) = \frac{\xi - \xi_i}{\xi_{i+p} - \xi_i} N_{i,p-1}(\xi) + \frac{\xi_{i+p+1} - \xi}{\xi_{i+p+1} - \xi_{i+1}} N_{i+1,p-1}(\xi). \tag{2.14}$$

From the above, it is evident that B-spline functions are piecewise polynomials. To construct a NURBS function $R_i^p(\xi)$ a particular weight w_i is assigned to each B-spline function and the NURBS function is generated as

$$R_i^p(\xi) = \frac{N_{i,p}(\xi) w_i}{\sum_{j=1}^{n} N_{j,p}(\xi) w_j}. \tag{2.15}$$

Note, that B-spline functions are a specific subset of the NURBS functions, which is obtained when all weights are equal.

From the presented formulas it is obvious that p^{th}-order NURBS basis functions can be automatically constructed for given knot vector Ξ and degree p. The examples of quadratic, cubic, and quartic B-spline basis functions over one patch divided into five knot spans are illustrated in Figure 2.1. All the examples consider an open knot vector with equally spaced interior knots. Important features of all NURBS basis functions can be observed. Firstly, NURBS basis constitutes a partition of unity

$$\forall \xi : \quad \sum_{i=1}^{n} R_i^p(\xi) = 1 \tag{2.16}$$

over the entire domain. Also, in contrast with standard FEA polynomial functions, NURBS functions are point-wise non-negative

$$\forall \xi : \quad R_i^p(\xi) \geq 0. \tag{2.17}$$

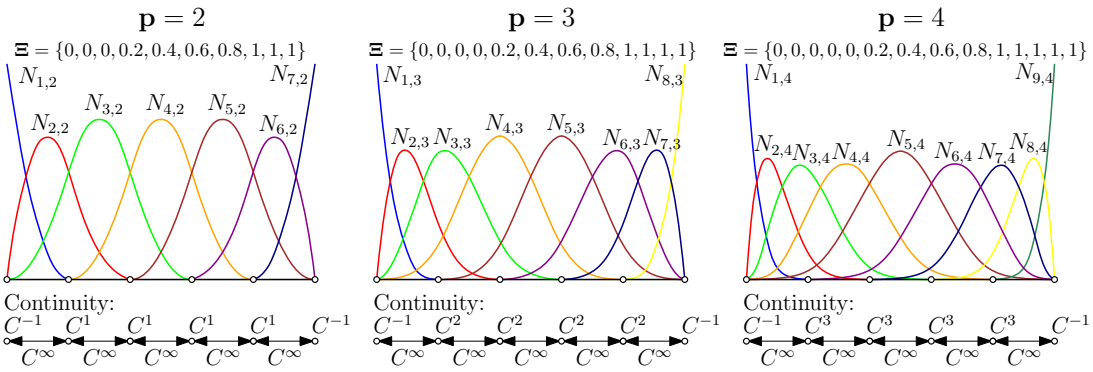

Figure 2.1.: Quadratic, cubic and quartic B-spline basis functions over one patch divided into five knot spans.

Moreover, the support of NURBS basis functions is always spanning over $p+1$ consecutive knot spans. Although the support seems to decrease at the patch boundaries, it is still $p+1$ knot spans including the knot spans with zero measure. Finally, one of the most important features of NURBS basis functions is inter-element continuity. Each basis function possesses up to a C^{p-1} continuity across the simple (not repeated) knots, while C^∞ continuity is provided over the individual knot spans. Many geometries can be described using just a single patch, so higher continuity can be provided along an entire computational domain. This feature significantly differentiates the NURBS basis functions from the standard FEA basis functions, where only the C^0 continuity across the element boundaries is typically provided. The continuity aspects of the NURBS basis functions are discussed in detail in Section 2.3.3.

2.2.2. Derivatives of basis functions

The derivatives of B-splines can be expressed in terms of the B-splines of lower order bases. The first derivative of the i–th B-spline function is given by

$$\frac{d}{d\xi}N_{i,p}(\xi) = \frac{p}{\xi_{i+p}-\xi_i}N_{i,p-1}(\xi) - \frac{p}{\xi_{i+p+1}-\xi_{i+1}}N_{i+1,p-1}(\xi). \tag{2.18}$$

Consequently, the generalization to the higher derivatives yields

$$\frac{d^k}{d^k\xi}N_{i,p}(\xi) = \frac{p}{\xi_{i+p}-\xi_i}\frac{d^{k-1}}{d^{k-1}\xi}N_{i,p-1}(\xi) - \frac{p}{\xi_{i+p+1}-\xi_{i+1}}\frac{d^{k-1}}{d^{k-1}\xi}N_{i+1,p-1}(\xi), \tag{2.19}$$

where k is a derivative order. The expression purely in terms of lower order functions can be derived by expanding (2.19) by means of (2.18). This formula including the efficient implementation can be found in [30].

Derivatives of NURBS basis functions can be expressed in terms of the derivatives of their non-rational counterparts (B-spline functions)

$$\frac{d}{d\xi}R_i^p(\xi) = w_i\frac{W(\xi)N'_{i,p}(\xi) - W'(\xi)N_{i,p}(\xi)}{(W(\xi))^2}, \tag{2.20}$$

where $(')$ denotes the derivative with respect to ξ and

$$W'(\xi) = \sum_{j=1}^{n} N'_{j,p}(\xi) w_j. \tag{2.21}$$

The formula for the higher order derivatives of NURBS basis functions [30] yields

$$\frac{d^k}{d^k\xi} R_i^p(\xi) = \frac{A_i^{(k)}(\xi) - \sum_{j=1}^{k} \binom{k}{j} W^{(j)}(\xi) \frac{d^{(k-j)}}{d\xi^{(k-j)}} R_i^p(\xi)}{W(\xi)}, \tag{2.22}$$

where $(\cdot)^{(k)}$ denotes the k^{th} derivative with respect to ξ and

$$A_i^{(k)}(\xi) \quad = \quad w_i \frac{d^k}{d\xi^k} N_{i,p}(\xi). \tag{2.23}$$

Note, that the sum on i does not apply in the previous formula (2.23). The binomial coefficient is defined as

$$\binom{k}{j} = \frac{k!}{j!(k-j)!}. \tag{2.24}$$

2.2.3. B-spline and NURBS curves

The NURBS curve is represented as a linear combination of NURBS basis functions and Cartesian coordinates of the control points $\boldsymbol{P}$. In consequence of the generally non-interpolatory nature of the NURBS basis functions, the control points generally do not lay on the curve. The linear interpolation of the control points is called a control polygon. This is in contrast to standard FEA where geometry and unknown approximation are interpolatory at nodes. The NURBS curve $\boldsymbol{C}(\xi)$ formed by n control points is constructed using corresponding basis functions R_i^p as

$$\boldsymbol{C}(\xi) = \sum_{i=1}^{n} R_i^p(\xi) \boldsymbol{P_i}. \tag{2.25}$$

An example of the B-spline curve constructed using four quadratic basis functions is depicted in Figure 2.2.

2.2.4. Key algorithms

There are many standardized algorithms for manipulating NURBS objects. In this section, the key algorithms necessary for isogeometric analysis are discussed. These mechanisms play an important role when it comes to mesh enrichment. All the presented algorithms enrich the initial basis without changing a curve geometrically or parametrically. Thus the original geometrical model is preserved.

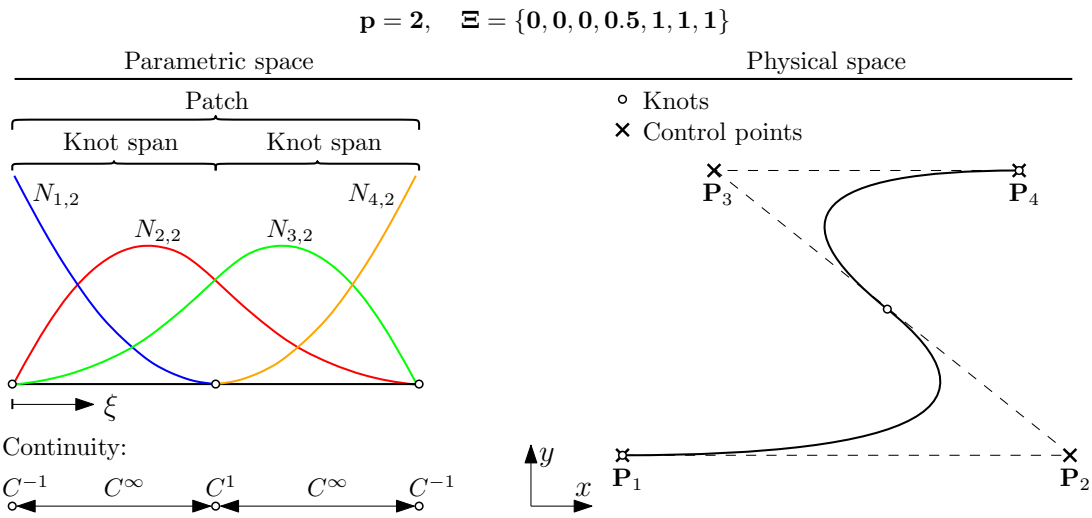

Figure 2.2.: Quadratic B-spline basis functions over one patch divided into two knot spans (left) and corresponding B-spline curve given by the control points $\boldsymbol{P_i}$(right).

Knot insertion

As already said, the NURBS curve is uniquely defined by a set of control points and NURBS basis functions R_i^p. Basis functions are given by the degree p and the knot vector $\Xi = \{\xi_1, ..., \xi_{n+p+1}\}$. By inserting a knot $\bar{\xi} \in (\xi_1, \xi_{n+p+1})$ into an existing knot vector Ξ, a new knot vector $\bar{\Xi}$ is formed. This new knot vector along with the fixed degree p can be used for generating a set of new basis functions $\bar{R}_i^p$. Consequently, it is necessary to recalculate the control points in order to maintain a parametric and geometric representation of the curve. The new set of control points $\boldsymbol{Q_i}$ can be determined by solving a system of linear equations

$$\sum_{i=1}^{n} R_i^p(\xi)\boldsymbol{P_i} = \sum_{j=1}^{n+1} \bar{R}_j^p(\xi)\boldsymbol{Q_j}. \tag{2.26}$$

The efficient solution of this system of equations along with the corresponding algorithm can be found in [30]. Note, that the same procedure can be used to increase a knot multiplicity by inserting a knot value already present in the knot vector. Knot insertion for simple quadratic NURBS curve is illustrated in Fig 2.3.

It is possible to formulate an efficient algorithm allowing to insert multiple knots at once. This procedure is referred to as knot refinement. The opposite procedure to knot insertion is knot removal. From the analysis point of view, this algorithm is not typically used; thus, the algorithm is not discussed here.

Degree elevation

As each p^{th} degree NURBS curve is a piecewise polynomial curve, it can be exactly described using basis functions of the higher polynomial degree $p + 1$. To keep the

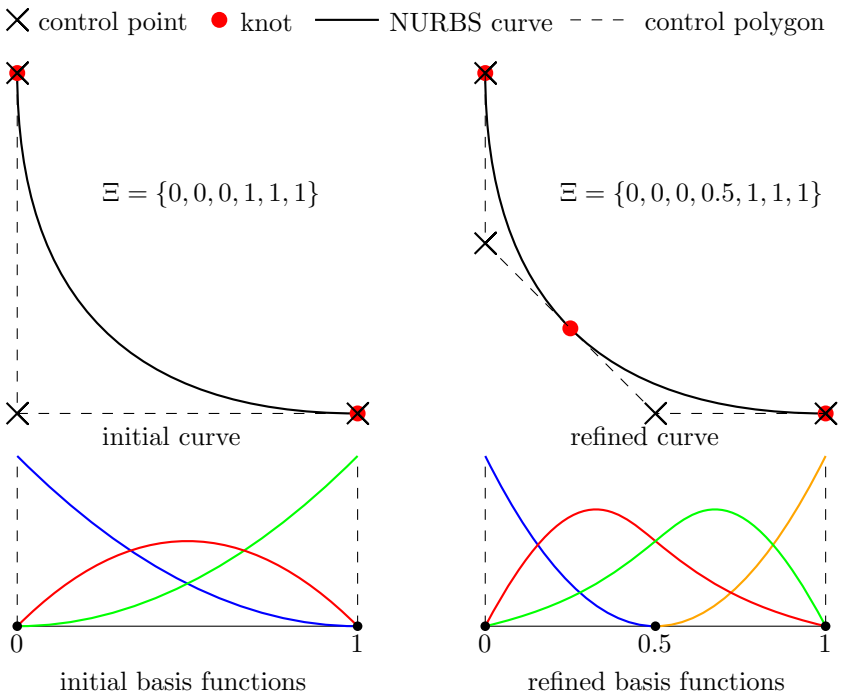

Figure 2.3.: Quadratic NURBS curve and basis functions before and after knot insertion at $\xi = 0.5$.

same parametric and geometric representation of the curve $C(\xi)$, it is necessary to determine new control points $\boldsymbol{Q}_j$ and a knot vector $\bar{\Xi}$ satisfying condition

$$C(\xi) = \sum_{i=1}^{n} R_i^p(\xi)\boldsymbol{P_i} = \sum_{j=1}^{m} \bar{R}_j^{p+1}(\xi)\boldsymbol{Q_j}. \tag{2.27}$$

Solution of this system of equations as well as the corresponding algorithm can be again found in [30]. Note that the initial continuity in interior knots is preserved during degree elevation. Degree elevation for simple quadratic NURBS curve is illustrated in Fig 2.4. Similarly to the knot reduction, the procedure of degree reduction [30] is not discussed here.

2.3. Remarks on NURBS-based analysis

The major difference between standard FEA and IGA is the use of the different basis functions. The numerical solution is obtained using the procedures described in Section 2.1. In this section, important consequences brought to the analysis with the use of NURBS basis functions are discussed.

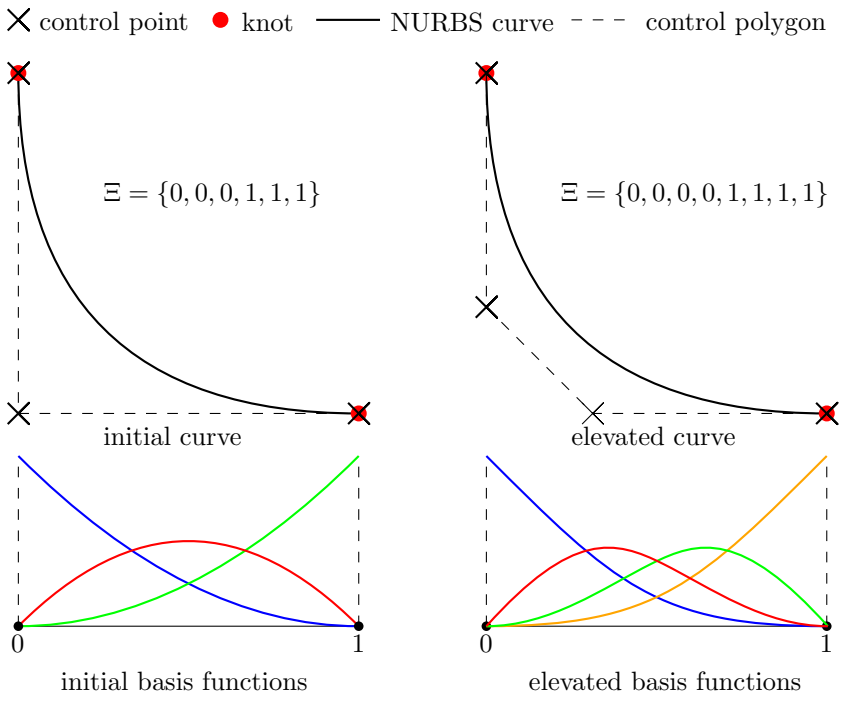

Figure 2.4.: Quadratic NURBS curve and basis functions before and after elevation to cubic degree.

2.3.1. Refinement strategies

One of the main benefits of isogeometric analysis is that all the available refinement strategies preserve the initial model both geometrically and parametrically. This feature enables automatic basis enrichment. Both refinement strategies of standard FEA, namely *h*- and *p*-refinement, can be used. An analogy to the standard *h*-refinement is the knot insertion, discussed in 2.2.4. By inserting a new knot value, the basis is enriched thanks to the subdivision into more knot spans. The *p*-refinement can be achieved by using the degree elevation, described in 2.2.4. By increasing the degree of the used basis functions, a richer basis is achieved.

In addition, a special feature referred to as *k*-refinement is available. The *k*-refinement is based on the feature that the degree elevation and knot insertion are not commutative. Particularly, it is not the same whether the *h*-refinement precedes *p*-refinement or whether it is the other way around. When both approaches are proceeded (while resulting in the same number of elements and the same order) the first case leads to the higher number of basis functions and the lower inter-element continuity. The more advantageous approach, degree elevation preceding knot insertion, is called *k*-refinement. See Fig. 2.5 for an illustrative example, where the initial domain of one knot span and two linear basis functions is subsequently refined to the domain of two knot spans and quadratic basis.

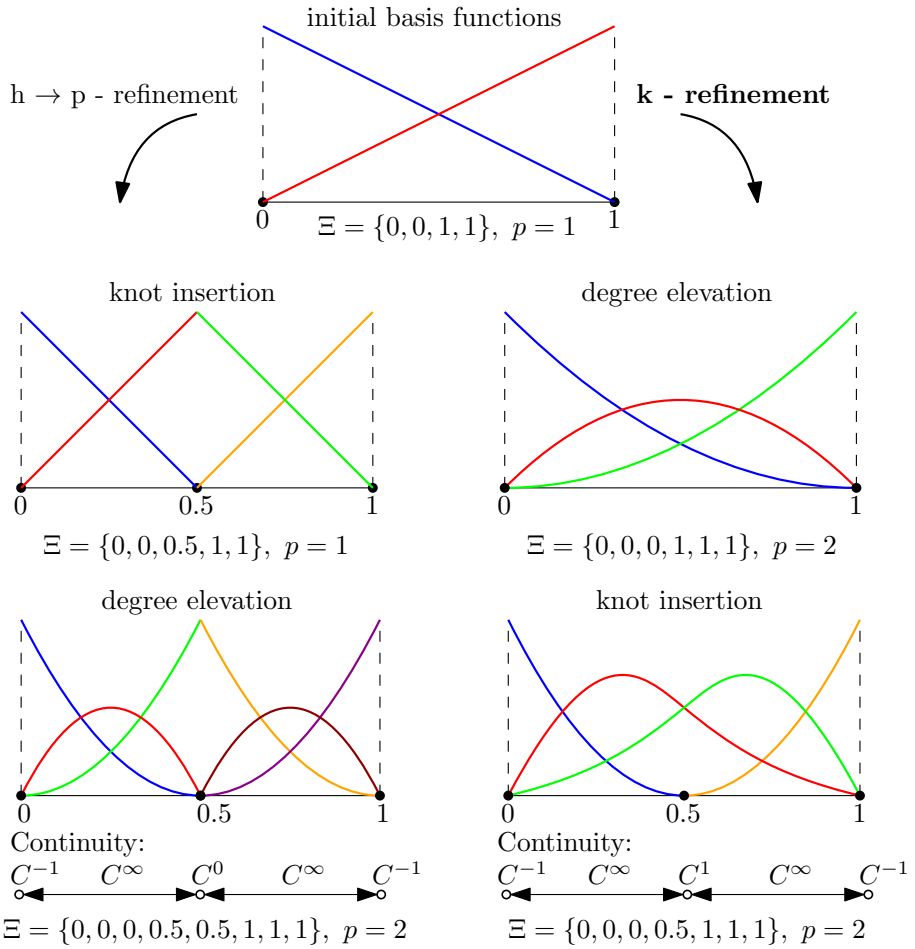

Figure 2.5.: Comparison of k-refinement with knot insertion followed by degree elevation. Before refinement - one knot span, order $p = 1$; after refinement - two knot spans, order $p = 2$. K-refinement results in higher inter-element continuity and lower number of basis functions.

2.3.2. Quadrature

In finite elements widely used Gaussian quadrature exactly integrates polynomial functions. Nevertheless in IGA, Gaussian quadrature is not exact and the integration is only approximate. Typically, the integration is carried out at knot span level and the integration rule is set up to exactly integrate B-spline functions of desired degree and used also for NURBS functions of the same degree. The sufficiency of such an approach can be shown by negligible differences in results while the number of Gauss points is adaptively increasing.

Due to the inter-element continuity, it can be concluded, that using the rule described above, the elements are overintegrated and the approach can be highly inefficient [33]. It has been shown that a number of Gauss points needed to integrate B-spline functions depends more on the number of basis functions over the patch than on the basis degree p. This is due to the smoothness across element boundaries which results in fewer degrees of freedom over the entire patch. This fact is exploited in so-called "half-point rule" proposed in [33]. This rule spans the entire patch and results in up to twice a lower number of Gauss points. One of the biggest drawbacks of the proposed rule is the necessity to recompute the number and positions of Gauss points when the number of knot spans changes. Another rule, which has been proposed in [34], is independent of the number of knot spans, but there have to be made special considerations on element boundaries. An alternative approach has been proposed in [35], where Gauss and Gauss-Lobatto rules are proposed for quadratic and cubic approximation. In the presented work, the quadrature is carried out at the knot span level for the reliability and simplicity of such an approach.

2.3.3. Continuity aspects

As already mentioned in Section 2.2.1, one of the most important features of NURBS basis functions is inter-element continuity. Traditional FEM polynomial basis provides typically only C^0 continuity between the elements. NURBS basis with not repeated interior knots naturally provides C^{p-1} continuity between the knot spans within a patch, while C^0 continuity is present between the patches. As the single patch model can be used for the vast range of problems, higher continuity can be achieved along the entire computational domain.

The lower continuity than C^{p-1} can be achieved between individual knot spans by increasing the knot multiplicity using the knot insertion discussed in Section 2.2.4. Across the knot with multiplicity m_i, the basis functions are C^{p-m_i} continuous. When the knot multiplicity $m_i = p$, the C^0 continuity is obtained and the basis becomes interpolatory at the particular knot ξ_i. A patch can be split into two absolutely independent patches by increasing the multiplicity to $m_i = p + 1$ resulting in C^{-1} continuity.

Similarly to the FEM, by assigning the same control point to the boundaries of neighbouring patches, C^0 continuity between patches is achieved. The interpolatory nature of the basis functions is available only between the patches or at the knots with enforced C^0 continuity. An illustrative example is given in Figure 2.6, where an example of cubic basis functions with a non-uniform knot vector is depicted.

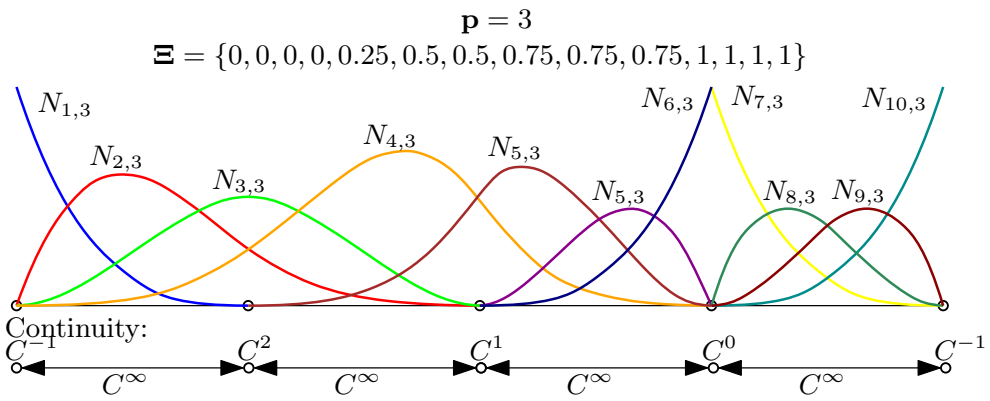

Figure 2.6.: Cubic B-spline basis functions over one patch divided into four knot spans with non-uniform knot vector.

2.3.4. FEA vs IGA codes

In standard FEA, the typical workflow of linear structural analysis is as follows. Firstly, the input data are read and the global matrices and vectors ($\boldsymbol{K}$, $\boldsymbol{f}$, ...) are allocated and initialized. This is followed by a loop through all the elements, where the contributions to $\boldsymbol{K}$ and $\boldsymbol{f}$ are assembled from individual element contributions evaluated using numerical integration. Solution of the governing equations (discretized equilibrium equations) yields displacement vector. This step is followed by post-processing internal variables (such as strains or stresses). Finally, the results are written to the output file.

To implement isogeometric analysis within standard finite element code, several changes have to be introduced. Obviously, the input file has to be enriched by additional data needed by IGA. Additionally to the control points coordinates (analogical to the nodal coordinates) and degree, the knot vector needs to be defined for the construction of the NURBS basis. IGA can benefit from the fact, that even initial mesh is geometrically exact and the refinement algorithms discussed in Section 2.2.4 keep both geometry and parametrization. Thus, an automatic refinement within the IGA code can be utilized, while only the initial mesh and required refinement are provided. In FEM, the h-refinement requires a generation of new mesh and p-refinement is often limited by a set of available elements and requires a generation of additional nodes.

Another difference between FEA and IGA code comes from different domain decomposition. While standard FEA evaluates characteristic terms by looping over elements and subsequently looping over integration points, in the case of the IGA model, these two loops run within another loop over patches. The routines evaluating basis functions and their derivatives must be modified. It could be also convenient to change the generation of output files to make clear the connection between control points and the corresponding patches. Finally, the available post-processing routines (e.g. internal variables calculation, graphical output) may need modification, mostly due to the non-interpolatory nature of the control point values. For more information on implementation aspects see e.g. [36, 37].

2.3.5. Enforcement of constraints

Non-interpolatory nature of NURBS basis functions affects how the boundary conditions are enforced. The prescription of kinematic constraints at the patch boundaries, where the basis functions are interpolatory, is straightforward. It can be achieved simply by setting the prescribed value of the solution vector at the corresponding control point like in standard FEM. On the other hand, to enforce such a constraint within a patch, special treatment of such a boundary condition is needed.

In this work, the above-mentioned boundary conditions are enforced using the Lagrange multipliers method. This approach enhances the potential energy W by an additional term enforcing the required constraints

$$W = W^{int} + W^{ext} + \sum_k \lambda_k \bar{r}^k, \tag{2.28}$$

where λ_k is the Lagrange multiplier for the k^{th} constraint. Due to the non-interpolatory nature of NURBS basis functions, constraint $\bar{r}^k$ must be expressed as a linear combination of the control point values using NURBS basis functions or its derivatives (evaluated at the particular position). The stationary conditions of W subsequently yield $m + k$ equations for m unknown displacements and k unknown Lagrange multipliers.

CHAPTER

THREE

ISOGEOMETRIC ANALYSIS OF BEAMS

Curved geometries are widely used in structural engineering for their load-carrying efficiency. In practice, curved beams are often modelled using a higher amount of straight elements, which leads to lower accuracy and a higher computational cost. Formulations of curved elements exist, but they are typically limited to constant curvature geometry. Use of NURBS formulation often allows exact geometry description for arbitrarily-curved beam geometries and brings superior accuracy to an analysis [11, 38].

As in standard FEA, beam elements can be divided into two major groups based on the kinematic assumptions: (1) Bernoulli theory suitable for thin beams neglecting the shear effect and (2) Timoshenko theory taking into account both bending and shear effects.

3.1. Timoshenko beam

In this section, two-dimensional Timoshenko beam theory is introduced briefly and two- and three-dimensional isogeometric Timoshenko curved beam formulations are provided. Timoshenko elements are suitable especially for thick structures, where both bending and shear effects must be taken into account. Additionally, with the appropriate locking treatment, these elements are applicable also for thin, bending-dominated structures. For their applicability to both thick and thin structures, Timoshenko elements are frequently used.

In the following, basic assumptions are illustrated on a straight beam. Considering two-dimensional beam in xy plane, the Timoshenko theory starts from the following assumptions:

- Load acts only in the plane of the beam.
- Cross-sectional dimensions remain unchanged after deformation.
- Plane cross-sections initially orthogonal to the centerline remain planar after deformation.

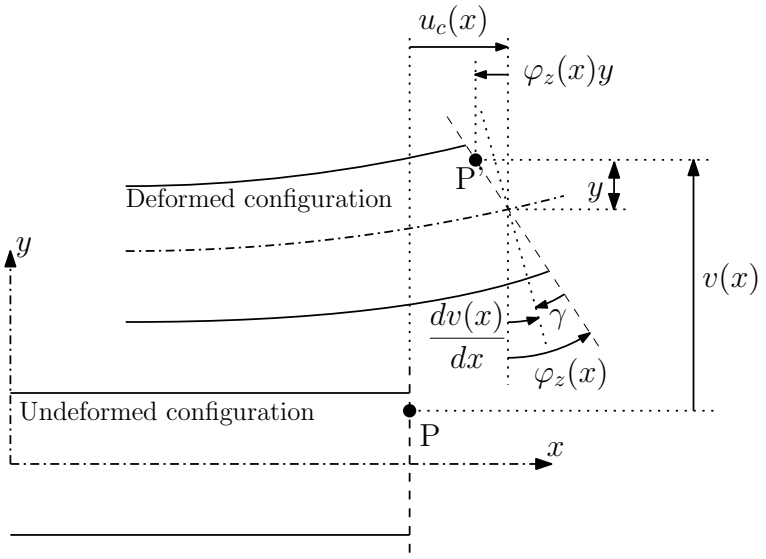

Figure 3.1.: Kinematics of a two-dimensional straight Timoshenko beam.

The kinematics of the cross-section is illustrated in Figure 3.1. The first assumption implies the independence of the solution of z coordinate. The second implies the constant deflection along the height of the beam

$$v(x,y) \quad = \quad v(x). \tag{3.1}$$

Finally, using the third assumption we can write

$$u(x,y) \quad = \quad u_c(x) - \varphi_z(x)y, \tag{3.2}$$

where u_c is the elongation of the centerline in the direction of the x-axis and φ_z is the cross-sectional rotation. The non-zero deformations are

$$\varepsilon_x(x,y) \quad = \quad \frac{\partial u(x,y)}{\partial x} = \frac{du_c(x)}{dx} - \frac{d\varphi_z(x)}{dx}y = \varepsilon_c(x) - \kappa_z(x)y, \tag{3.3}$$

$$\gamma_{xy}(x) \quad = \quad \frac{\partial v(x,y)}{\partial x} + \frac{\partial u(x,y)}{\partial y} = \frac{dv(x)}{dx} - \varphi_z(x). \tag{3.4}$$

For the presented formulations it is more convenient to express normal deformation of the centerline ε_c and curvature κ_z separately as $\boldsymbol{\varepsilon} = \{\varepsilon_c, \gamma_{xy}, \kappa_z\}^T$. An operator matrix $\boldsymbol{\partial}$ (2.2) results from the previous relations written in the matrix form

$$\boldsymbol{\varepsilon}(x) = \left\{ \begin{array}{c} \varepsilon_c(x) \\ \gamma_{xy}(x) \\ \kappa_z(x) \end{array} \right\} = \underbrace{\left[\begin{array}{ccc} \frac{d}{dx} & 0 & 0 \\ 0 & \frac{d}{dx} & -1 \\ 0 & 0 & \frac{d}{dx} \end{array} \right]}_{\boldsymbol{\partial}^T} \left\{ \begin{array}{c} u_c(x) \\ v(x) \\ \varphi_z(x) \end{array} \right\}. \tag{3.5}$$

In beam analysis, it is common to work with internal forces instead of stresses. Normal force N, shear force Q, and bending moment M are defined as

$$N(x) = \int_A \sigma_x(x,y)\, dA, \tag{3.6}$$

$$Q(x) = \int_A \tau_{xy}(x)\, dA, \tag{3.7}$$

$$M(x) = \int_A \sigma_x(x,y) y\, dA, \tag{3.8}$$

where A is the area of the cross-section. Assuming a linear elastic material, by substituting from (3.3) the following relations for internal forces are gradually obtained

$$N(x) = \int_A E(\varepsilon_c(x) - \kappa_z(x) y)\, dA = EA\varepsilon_c(x), \tag{3.9}$$

$$Q(x) = \int_A G\left(\frac{\partial v(x)}{\partial x} - \varphi_z(x)\right) dA = kGA\gamma_{xy}(x), \tag{3.10}$$

$$M(x) = \int_A E(\varepsilon_c(x) - \kappa_z(x) y) y\, dA = EI\kappa_z(x), \tag{3.11}$$

where E is Young's modulus, G is shear modulus, k is shear coefficient, and I is moment of inertia. Constant cross-sectional and material characteristics are considered here. The above equations assume that axes x, y are central axes so that the following condition holds

$$\int_A y\, dA = S_z = 0, \tag{3.12}$$

thus

$$\int_A \kappa_z(x) y\, dA = 0, \tag{3.13}$$

$$\int_A \varepsilon_c(x) y\, dA = 0. \tag{3.14}$$

Constitutive relations (3.9-3.11) can be expressed in matrix form as

$$\left\{ \begin{array}{c} N(x) \\ Q(x) \\ M(x) \end{array} \right\} = \underbrace{\left[\begin{array}{ccc} EA & 0 & 0 \\ 0 & kGA & 0 \\ 0 & 0 & EI \end{array} \right]}_{\boldsymbol{D}} \left\{ \begin{array}{c} \varepsilon_c(x) \\ \gamma_{xy}(x) \\ \kappa_z(x) \end{array} \right\}, \tag{3.15}$$

where $\boldsymbol{D}$ is a constitutive matrix.

3.1.1. Two-dimensional curved formulation

The formulation of curved Timoshenko beam element follows the work by Bouclier et al. [10]. The notation used in [10] is adopted here. There are three independent unknowns: tangential (longitudinal) displacement u_t, normal (transverse) displacement

u_n and rotation θ. For membrane, transverse shear and bending strains we have

$$\varepsilon_m(s) = u_t'(s) - \frac{u_n(s)}{R(s)}, \tag{3.16}$$

$$\gamma_s(s) = \frac{u_t(s)}{R(s)} + u_n'(s) - \theta(s), \tag{3.17}$$

$$\chi_b(s) = \theta'(s), \tag{3.18}$$

where $s \in \langle 0, L \rangle$ runs along the centerline of a beam of length L and prime indicates a derivative with respect to s. For simplicity, the dependence on (s) will be omitted in the following text. A radius of curvature R is defined as

$$R = \frac{1}{x'y'' - y'x''}, \tag{3.19}$$

where x and y are coordinates of the position vector of the centerline. The geometrical relations (3.16-3.18) can be expressed using a matrix notation as

$$\boldsymbol{\varepsilon} = \begin{Bmatrix} \varepsilon_m \\ \gamma_s \\ \chi_b \end{Bmatrix} = \begin{bmatrix} \frac{\partial}{\partial s} & -\frac{1}{R} & 0 \\ \frac{1}{R} & \frac{\partial}{\partial s} & -1 \\ 0 & 0 & \frac{\partial}{\partial s} \end{bmatrix} \begin{Bmatrix} u_t \\ u_n \\ \theta \end{Bmatrix} = \boldsymbol{\partial}^T \boldsymbol{u}. \tag{3.20}$$

Note that by omitting the terms which are divided by radius of curvature R, the straight beam formulation derived in the previous section can be recovered.

On each element the unknowns u_t, u_n, and θ are expressed as the linear combination of approximation functions and the vector of control points' values $\boldsymbol{r}^e$

$$\boldsymbol{u}^e = \boldsymbol{N}^e \boldsymbol{r}^e. \tag{3.21}$$

In the context of the presented work NURBS approximation is used. In practical formulations, the same approximation is used for u_t, u_n, and θ. From (3.20) a strain vector on element is evaluated as

$$\boldsymbol{\varepsilon}^e = \boldsymbol{\partial}^T \boldsymbol{u}^e = \boldsymbol{\partial}^T \boldsymbol{N}^e \boldsymbol{r}^e = \boldsymbol{B}^e \boldsymbol{r}^e. \tag{3.22}$$

A constitutive matrix $\boldsymbol{D}$ derived in (3.15) is used. An element stiffness matrix $\boldsymbol{K}^e$ defined in (2.11) is evaluated as

$$\boldsymbol{K}^e = \int_{L^e} \boldsymbol{B}^{eT} \boldsymbol{D} \boldsymbol{B}^e \, ds. \tag{3.23}$$

using the Gaussian quadrature involving $(p+1)$ Gauss points over each knot span.

3.1.2. Three-dimensional curved formulation

The formulation of the three-dimensional beam element [12] is derived in local coordinate system $(\boldsymbol{t}(s), \boldsymbol{n}(s), \boldsymbol{b}(s))$, where $\boldsymbol{t}, \boldsymbol{n}, \boldsymbol{b}$ are tangent, normal and binormal vectors

(see Fig. 3.2). The orthonormal unit triad $(\boldsymbol{t}, \boldsymbol{n}, \boldsymbol{b})$ is called Frenet-Serret frame and is given by the position vector $\boldsymbol{s}(s)$ as

$$\boldsymbol{t} = \frac{d\boldsymbol{s}(s)}{ds}, \tag{3.24}$$

$$\boldsymbol{n} = \frac{\frac{d^2\boldsymbol{s}(s)}{ds^2}}{\left|\left|\frac{d^2\boldsymbol{s}(s)}{ds^2}\right|\right|}, \tag{3.25}$$

$$\boldsymbol{b} = \boldsymbol{t} \times \boldsymbol{n}. \tag{3.26}$$

For Timoshenko beam in three-dimensional space there are six independent unknowns: tangential displacement u_t, normal displacement u_n, binormal displacement u_b and rotations θ_t, θ_n, θ_b (see Fig. 3.2).

The membrane strain ε_m, shear strains γ_n and γ_b, torsional strain χ_t, and bending strains χ_n and χ_b are given as

$$\varepsilon_m = u_t' - \kappa u_n, \tag{3.27}$$

$$\chi_t = \theta_t' - \kappa\theta_n, \tag{3.28}$$

$$\gamma_n = \kappa u_t + u_n' - \tau u_b - \theta_b, \tag{3.29}$$

$$\chi_n = \kappa\theta_t + \theta_n' - \tau\theta_b, \tag{3.30}$$

$$\gamma_b = \tau u_n + u_b' + \theta_n, \tag{3.31}$$

$$\chi_b = \tau\theta_n + \theta_b'. \tag{3.32}$$

The above equations can be expressed using matrix notation

$$\boldsymbol{\varepsilon} = \begin{Bmatrix} \varepsilon_m \\ \chi_t \\ \gamma_n \\ \chi_n \\ \gamma_b \\ \chi_b \end{Bmatrix} = \begin{bmatrix} \frac{\partial}{\partial s} & -\kappa & 0 & 0 & 0 & 0 \\ 0 & 0 & 0 & \frac{\partial}{\partial s} & -\kappa & 0 \\ \kappa & \frac{\partial}{\partial s} & -\tau & 0 & 0 & -1 \\ 0 & 0 & 0 & \kappa & \frac{\partial}{\partial s} & -\tau \\ 0 & \tau & \frac{\partial}{\partial s} & 0 & 1 & 0 \\ 0 & 0 & 0 & 0 & \tau & \frac{\partial}{\partial s} \end{bmatrix} \begin{Bmatrix} u_t \\ u_n \\ u_b \\ \theta_t \\ \theta_n \\ \theta_b \end{Bmatrix} = \boldsymbol{\partial}^T \boldsymbol{u}. \tag{3.33}$$

A geometrical matrix $\boldsymbol{B}^e$ is derived by replacing the unknowns u_t, u_n, u_b and θ_t, θ_n, θ_b by the linear combination of approximation functions and the vector of nodal values $\boldsymbol{r}^e$ on each element. Curvature κ is given as

$$\kappa = \left|\left|\frac{d^2\boldsymbol{s}(s)}{ds^2}\right|\right| \tag{3.34}$$

and torsion τ as

$$\tau = \frac{d\boldsymbol{n}(s)}{ds}\boldsymbol{b}(s). \tag{3.35}$$

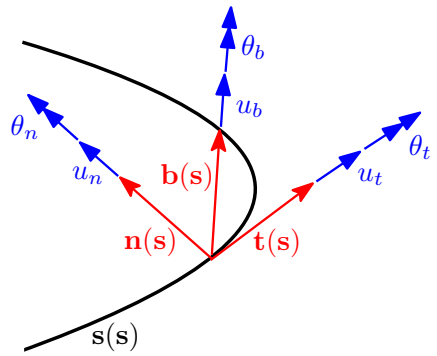

Figure 3.2.: Local coordinate system and degrees of freedom of a three-dimensional curved beam element.

Assuming a linear elastic material the constitutive matrix $\boldsymbol{D}$ is given by constitutive relations

$$\begin{Bmatrix} N \\ M_t \\ Q_n \\ M_n \\ Q_b \\ M_b \end{Bmatrix} = \underbrace{\begin{bmatrix} EA & 0 & 0 & 0 & 0 & 0 \\ 0 & GI_k & 0 & 0 & 0 & 0 \\ 0 & 0 & GA_n & 0 & 0 & 0 \\ 0 & 0 & 0 & EI_n & 0 & 0 \\ 0 & 0 & 0 & 0 & GA_b & 0 \\ 0 & 0 & 0 & 0 & 0 & EI_b \end{bmatrix}}_{\boldsymbol{D}} \begin{Bmatrix} \varepsilon_m \\ \chi_t \\ \gamma_n \\ \chi_n \\ \gamma_b \\ \chi_b \end{Bmatrix}, \tag{3.36}$$

where I_k is the torsional moment, I_n, I_b are the moments of inertia, A_b, A_n are the shear areas. Similarly to the two-dimensional formulation, the element stiffness matrix $\boldsymbol{K}^e$ is evaluated using Gaussian quadrature.

3.1.3. Numerical locking

Analysis of Timoshenko beams suffers from numerical locking [11]. As well as in standard finite elements both membrane and shear locking occur for shear-deformable element formulations when the modelled structure is thin. This behavior significantly deteriorates the convergence of the numerical solution. This problem occurs when displacements and rotation are treated independently and the same order of interpolation is used for both of them. For example, for two-dimensional beam, it can be seen from Equations for shear and bending strains (3.17-3.18) that the formula for bending strain results in a lower order term than the formula for shear strain, but actually this should be vice-versa. Moreover, from the formula for the shear strain (3.17) $\gamma_s = \frac{u_t}{R} + u_n' - \theta$ it is obvious that zero shear strain cannot be satisfied along entire patch when the same interpolation order of unknowns is used because of field-inconsistency [39].

The problem of numerical locking impacts especially the low-order elements. There have been many studies on locking phenomena in standard elements (see for example [40, 41]) and several approaches to overcome this issue have been proposed, such

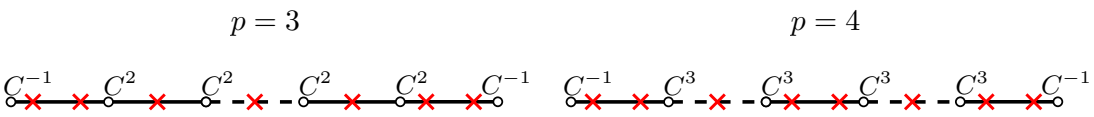

Figure 3.3.: Reduced integration schemes for cubic and quartic NURBS basis functions with C^{p-1} continuity across knots.

as the use of higher-order basis [42], reduced integration [43–45], or use of different approximation order for each of the fields [46, 47].

Standard locking removal methods have been modified for use in isogeometric analysis and their performance has been analyzed. Similarly to the standard elements, the use of a higher-order NURBS basis can alleviate locking [11]. The reduced integration, popular locking-treatment in standard FEM for its computational efficiency and easy implementation, is not convenient for IGA, as the optimal reduced integration rule depends on the choice of approximation order and continuity and such a rule is hard to be determined. Nevertheless, some improved integration rules have been proposed in several studies [10, 39, 48, 49]. Good results have been obtained using Discrete shear gap (DSG) method [10, 11] or $\bar{\mathrm{B}}$ method [10] which can be used independently of the choice of approximation. Reduced integration, DSG method, and $\bar{\mathrm{B}}$ method are also studied in the presented work.

Reduced Integration

Reduced integration is widely used to remove shear locking in standard finite elements by integrating the contribution of shear terms using a lower number of integration points. On straight beams, this leads to the same results as using the assumed strain method or enriched approximation. In the case of isogeometric analysis, the existence of higher inter-element continuity has to be taken into account. For the comparison of locking removal techniques within this work, an extension of the integration schemes proposed by Adam et al. [39] is considered. For cubic and quartic NURBS basis functions with C^{p-1} continuity across knots used within this work, the following rules are suggested:

- $\boldsymbol{C^2}$ **cubic**: a one-point integration rule with an additional point on each boundary element.
- $\boldsymbol{C^3}$ **quartic**: a one-point integration rule with an additional point on each boundary element and another additional point on the middle element.

See Figure 3.3 for the illustration of the integration schemes. These rules can be easily extended for the higher-order approximations, nevertheless, an extension to the basis with variable inter-element continuity within a patch has not been proposed.

Discrete Shear Gap

This method, originally developed for the standard finite elements [50], has been extended by Echter and Bischoff [11] for isogeometric analysis. The procedure for two-

dimensional beam formulation is introduced in the following text. The approach can be divided into several steps yielding the modified $\boldsymbol{B}$ matrix.

The equations for strains

$$\varepsilon_m = u_t' - \frac{u_n}{R}, \tag{3.37}$$

$$\gamma_s = \frac{u_t}{R} + u_n' - \theta \tag{3.38}$$

can not be satisfied (in discretized form for equal order approximation) due to the field inconsistency. The idea is not to satisfy them pointwise but in an integral sense. With a shear strain as an example, by integrating (3.38)

$$\int_0^{s_i} \gamma_s \, ds = \int_0^{s_i} \left(\frac{u_t}{R} + u_n' - \theta \right) \, ds = u_n^{\gamma^i} \tag{3.39}$$

so called shear gap $u_n^{\gamma^i}$ can be evaluated at collocation point s_i. Collocation points s_i are calculated as Greville abscissae of the control points [51]. Next, shear gap values at collocation points are transformed into equivalent control points' variables $\tilde{u}_n^{\gamma^i}$

$$\tilde{\boldsymbol{u}}_n^{\gamma} = \boldsymbol{A}^{-1} \boldsymbol{u}_n^{\gamma}, \qquad A_{ij} = R_j(s_i), \tag{3.40}$$

where $R_j(s_i)$ is the j^{th}-basis function evaluated at i^{th}-collocation point. The modified shear deformation γ_s^{mod} is then computed from (3.39). In a discretized form, it can be expressed as a linear combination of derivatives of basis functions and values of shear gaps at control points

$$\gamma_s^{mod} = \sum_{i=1}^{n} R_i' \tilde{u}_n^{\gamma^i}. \tag{3.41}$$

This equation is then used instead of (3.38) in strain-displacement relations

$$\boldsymbol{\varepsilon} = \boldsymbol{B}^{DSG} \boldsymbol{r}. \tag{3.42}$$

Finally, matrix $\boldsymbol{B}^{DSG}$ is used to evaluate stiffness matrix $\boldsymbol{K}$ (3.23).

Similar steps are applied to the membrane strain. An analogous procedure is also used in the case of three-dimensional beam formulation. Note, that this modification has to be performed on the patch level, as collocation points are located along the patch. This prevents evaluating the individual contribution on a knot-span level and the implementation of a beam element needs to be modified. Moreover, the inverse of $\boldsymbol{A}$ leads to a generally full stiffness matrix where sparsity is lost.

$\bar{\mathrm{B}}$ method

The main idea of the $\bar{\mathrm{B}}$ method is to project membrane strain ε_m and shear strain γ_s onto a basis of lower order. Lower-order basis functions are generated using the modified knot vector obtained from the knot vector of actual approximation by removing the first ($\xi_1 = 0$) and the last ($\xi_{p+n+1} = 1$) knot. Such an approach results in $\bar{n} = n - 1$ basis functions of degree $\bar{p} = p - 1$.

Considering a membrane strain as an example, the procedure starts with L_2 projection [52]

$$\int_L \bar{N}_j(\varepsilon_m - \bar{\varepsilon}_m)\, dL = 0, \tag{3.43}$$

where $\bar{N}_j$ are the functions of the lower order basis ($j = 1, 2, \ldots, \bar{n}$) and $\bar{\varepsilon}_m$ is the projected membrane strain, which can be written in discretized form as

$$\bar{\varepsilon}_m = \sum_{i=1}^{\bar{n}} \bar{N}_i \bar{\varepsilon}_m^i. \tag{3.44}$$

The corresponding degrees of freedom $\bar{\varepsilon}_m^i$ can be solved by substituting (3.44) into (3.43). Finally, the modified strain is obtained using (3.44) as

$$\bar{\varepsilon}_m = \sum_{i,j=1}^{\bar{n}} \bar{N}_i M_{ij}^{-1} \int_L \bar{N}_j \varepsilon_m\, dL, \tag{3.45}$$

where $\boldsymbol{M}$ is the "mass" matrix of the lower order basis defined as

$$M_{ij} = \int_L \bar{N}_i \bar{N}_j\, dL. \tag{3.46}$$

By expressing a membrane strain ε_m in a discretized form using geometrical relations, a modified strain can be expressed as

$$\bar{\varepsilon}_m = \sum_{i=1}^{\bar{n}} \bar{N}_i \boldsymbol{M}^{-1} \bar{\boldsymbol{B}}_m \boldsymbol{r}. \tag{3.47}$$

The membrane contribution to stiffness matrix $\boldsymbol{K}_m$ is then calculated as

$$\boldsymbol{K}_m = EA\, \bar{\boldsymbol{B}}_m^T \boldsymbol{M}^{-1} \bar{\boldsymbol{B}}_m. \tag{3.48}$$

The analogical procedure can be followed also for the shear strain γ_s. Note that this procedure leads to a stiffness matrix where the sparsity is lost, which significantly influences the computational cost.

3.2. Bernoulli beam element

In this section, two-dimensional Bernoulli beam theory is introduced briefly and formulation of isogeometric spatial curved Bernoulli beam element accounting also for nonlinear effects is provided. Bernoulli elements are suitable for thin, bending-dominated structures; the effect of shear is neglected. Bernoulli kinematics assume that the orthogonality of the cross-section to the centerline is preserved after deformation. All other assumptions introduced in Section (3.1) are applicable also for Bernoulli beams.

Figure 3.4 illustrates the kinematics of the cross-section of the beam in xy plane. From the kinematic assumptions, it follows that the rotation of the cross-section φ_z

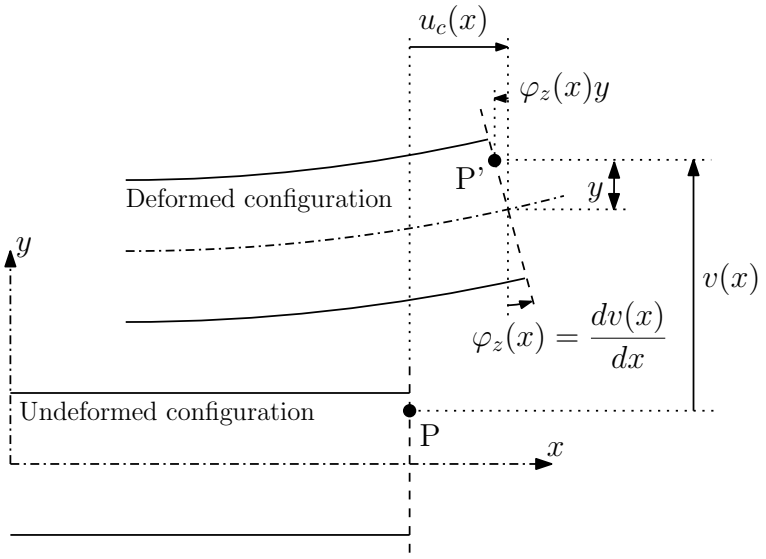

Figure 3.4.: Kinematics of a two-dimensional straight Bernoulli beam.

about the z axis is no longer independent, but equals to the deflection derivative

$$\varphi_z(x) = \frac{dv(x)}{dx}. \tag{3.49}$$

The only nonzero strain is normal strain ε_x, which is calculated as

$$\varepsilon_x(x,y) = \frac{\partial u(x,y)}{\partial x} = \frac{du_c(x)}{dx} - \frac{d^2v(x)}{dx^2}y, \tag{3.50}$$

where u_c is the displacement of the centerline in the direction of the x-axis. The normal strain ε_x is related to normal stress σ_x by a constitutive relation. Assuming a linear, elastic material, the constitutive relation yields

$$\sigma_x(x,y) = E(x)\varepsilon_x(x,y) = E(x)\left(\frac{du_c(x)}{dx} - \frac{d^2v(x)}{dx^2}y\right), \tag{3.51}$$

where E is the Young's modulus. Considering a strain vector in a form $\boldsymbol{\varepsilon} = \{\varepsilon_c, \kappa_z\}^T$, an operator matrix $\boldsymbol{\partial}$ (2.2) yields

$$\boldsymbol{\varepsilon}(x) = \left\{ \begin{array}{c} \varepsilon_c(x) \\ \kappa_z(x) \end{array} \right\} = \underbrace{\left[\begin{array}{cc} \frac{d}{dx} & 0 \\ 0 & \frac{d^2}{dx^2} \end{array} \right]}_{\boldsymbol{\partial}^T} \left\{ \begin{array}{c} u_c(x) \\ v(x) \end{array} \right\}. \tag{3.52}$$

Assuming y axis being the neutral axis, the normal force N and the bending moment M are given as

$$N(x) = \int_A \sigma_x(x,z)\, dA = EA\frac{du_c(x)}{dx} = EA\varepsilon_c(x), \tag{3.53}$$

$$M(x) = \int_A \sigma_x(x,z)y\, dA = -EI\frac{d^2v(x)}{dx^2} = EI\kappa_z(x), \tag{3.54}$$

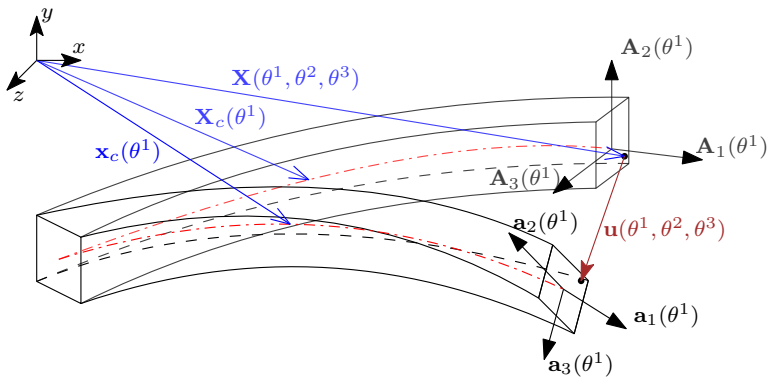

Figure 3.5.: Illustration of the beam in its undeformed and deformed configurations.

where A is a cross-sectional area and I is a moment of inertia. By expressing the above relations in a matrix form, a constitutive matrix $\boldsymbol{D}$ can be defined

$$\left\{ \begin{array}{c} N(x) \\ M(x) \end{array} \right\} = \underbrace{\left[\begin{array}{cc} EA & 0 \\ 0 & EI \end{array} \right]}_{\boldsymbol{D}} \left\{ \begin{array}{c} \varepsilon_c(x) \\ \kappa_z(x) \end{array} \right\}. \tag{3.55}$$

3.2.1. Spatial geometrically-nonlinear formulation

The formulation of the three-dimensional beam element presented by Bauer et al. [14] is based on Bernoulli beam theory and accounts for the geometrically nonlinear behavior. The element has four degrees of freedom at each control point: three global displacements u, v, and w and the additional degree of freedom corresponding to rotation around the centerline ψ. The rotational degree of freedom enables the element to develop a torsion (warping effects are neglected here) and also to model initially twisted beams.

Geometric description

In the following, the standard notation using upper-case and lower-case letters for the undeformed and deformed configuration, respectively, is adopted, for example $\boldsymbol{X}$ ($\boldsymbol{x}$). The beam formulation (see Figure 3.5) starts from a three-dimensional approximation that is subsequently reduced to the displacements of the centerline using Bernoulli kinematic assumptions. The centerline is given by the position vector $\boldsymbol{X}_c$ ($\boldsymbol{x}_c$). The position vector of the centerline is described as a linear combination of the control points coordinates $\hat{\boldsymbol{X}}^i$ and the corresponding basis functions R_i^p

$$\boldsymbol{X}_c = \sum_i R_i^p \hat{\boldsymbol{X}}^i, \tag{3.56}$$

$$\boldsymbol{x}_c = \sum_i R_i^p \hat{\boldsymbol{x}}^i. \tag{3.57}$$

Deformed position vector is given as

$$\hat{\boldsymbol{x}}^i = \hat{\boldsymbol{X}}^i + \hat{\boldsymbol{u}}^i, \tag{3.58}$$

where $\hat{\boldsymbol{u}}^i$ is a vector of displacements corresponding to global degrees of freedom (u, v, w).

Additionally to the centerline, the cross-section orientation is described by a moving trihedral given by the base vectors $\boldsymbol{A}_i$ $(\boldsymbol{a}_i)$ with $i \in \{1, 2, 3\}$. A position vector $\boldsymbol{X}(\boldsymbol{x})$ of an arbitrary point of a beam can be expressed as

$$\boldsymbol{X}(\theta^1, \theta^2, \theta^3) = \boldsymbol{X}_c(\theta^1) + \theta^2 \boldsymbol{A}_2(\theta^1) + \theta^3 \boldsymbol{A}_3(\theta^1), \tag{3.59}$$

$$\boldsymbol{x}(\theta^1, \theta^2, \theta^3) = \boldsymbol{x}_c(\theta^1) + \theta^2 \boldsymbol{a}_2(\theta^1) + \theta^3 \boldsymbol{a}_3(\theta^1), \tag{3.60}$$

where θ^i are the convective contravariant coordinates of coordinate system, see Figure 3.5.

The first components of a moving trihedral $\boldsymbol{A}_1$ and $\boldsymbol{a}_1$ are aligned with normalized tangents $\boldsymbol{T}$ and $\boldsymbol{t}$, respectively, and are computed as

$$\boldsymbol{A}_1 = \sum_i R^p_{i,1} \hat{\boldsymbol{X}}^i, \tag{3.61}$$

$$\boldsymbol{a}_1 = \sum_i R^p_{i,1} \hat{\boldsymbol{x}}^i, \tag{3.62}$$

where $(\cdot)_{,i}$ denotes the derivative with respect to the coordinate θ^i. The remaining components $\boldsymbol{A}_\alpha$ with $\alpha \in \{2, 3\}$ are orthogonal to the tangent of the centerline (resp. $\boldsymbol{A}_1$) and are described by the reference trihedral, given by $\boldsymbol{A}^0_\alpha$, $\boldsymbol{T}_0$, as

$$\boldsymbol{A}_\alpha = \bar{\boldsymbol{R}}_{\boldsymbol{T}}(\Psi) \boldsymbol{\Lambda}(\boldsymbol{T}_0, \boldsymbol{T}) \boldsymbol{A}^0_\alpha, \tag{3.63}$$

where Ψ is an initial rotation about a tangent of a beam, and $\boldsymbol{\Lambda}$ and $\bar{\boldsymbol{R}}_{\boldsymbol{T}}$ are the two key operations used for the alignment of a moving trihedral illustrated in Figure 3.6. While the mapping matrix $\boldsymbol{\Lambda}(\boldsymbol{T}_0, \boldsymbol{T})$ aligns the reference trihedral given by the tangent $\boldsymbol{T}_0$ to the tangent $\boldsymbol{T}$ at the current (udeformed) position, the rotation matrix $\bar{\boldsymbol{R}}_{\boldsymbol{T}}(\Psi)$ rotates the aligned reference trihedral about $\boldsymbol{T}$ with given rotation Ψ. The rotation $\Psi = \Psi(\theta^1)$ is calculated using basis functions and values $\hat{\Psi}^i$ assigned to the control points. The Euler-Rodriguez formula [53] is used to define both the mapping matrix $\boldsymbol{\Lambda}$ and the rotation matrix $\bar{\boldsymbol{R}}_{\boldsymbol{T}}$.

Analogical procedures denoted as $\boldsymbol{\Lambda}(\boldsymbol{T}, \boldsymbol{t})$ and $\bar{\boldsymbol{R}}_{\boldsymbol{t}}(\psi)$ are used to align the moving trihedral of the undeformed to the deformed configuration. The base vectors $\boldsymbol{a}_\alpha$ of the deformed configuration are given as

$$\boldsymbol{a}_\alpha = \bar{\boldsymbol{R}}_{\boldsymbol{t}}(\psi) \boldsymbol{\Lambda}(\boldsymbol{T}, \boldsymbol{t}) \boldsymbol{A}_\alpha, \tag{3.64}$$

where $\psi = \psi(\theta^i)$ is a rotational degree of freedom evaluated at the current position θ^i. The base vectors of the undeformed continuum $\boldsymbol{G}_i$ are defined as $\boldsymbol{G}_i = \boldsymbol{X}_{,i}$ leading to

$$\boldsymbol{G}_1(\theta^1, \theta^2, \theta^3) = \boldsymbol{A}_1(\theta^1) + \theta^2 \boldsymbol{A}_{2,1}(\theta^1) + \theta^3 \boldsymbol{A}_{3,1}(\theta^1), \tag{3.65}$$

$$\boldsymbol{G}_2(\theta^1) = \boldsymbol{A}_2(\theta^1), \tag{3.66}$$

$$\boldsymbol{G}_3(\theta^1) = \boldsymbol{A}_3(\theta^1) \tag{3.67}$$

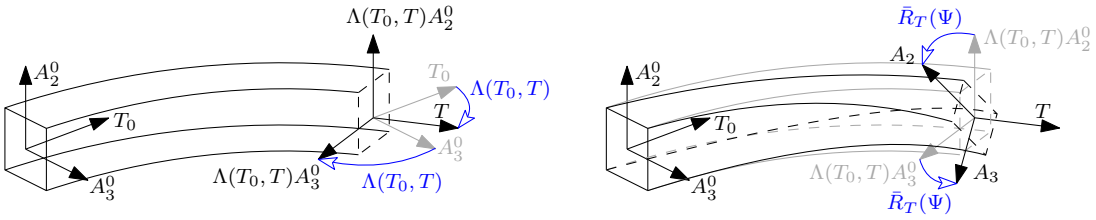

Figure 3.6.: The $\boldsymbol{\Lambda}(\boldsymbol{T}_0, \boldsymbol{T})$ and $\bar{\boldsymbol{R}}_{\boldsymbol{T}}(\Psi)$ operations used for the alignment of the cross-section at the current position.

with analogical equations for the base vectors $\boldsymbol{g}_i = \boldsymbol{x}_{,i}$ of the undeformed configuration. In the sequel, dot products $\boldsymbol{G}_i \cdot \boldsymbol{G}_j$ ($\boldsymbol{g}_i \cdot \boldsymbol{g}_j$) and $\boldsymbol{A}_i \cdot \boldsymbol{A}_j$ ($\boldsymbol{a}_i \cdot \boldsymbol{a}_j$) are denoted as G_{ij} (g_{ij}) and A_{ij} (a_{ij}), respectively.

Green-Lagrange strain tensor

The Green-Lagrange strain tensor $\boldsymbol{E}$ calculated for the curvilinear coordinate system is defined [54] as

$$E_{ij} = \frac{1}{2}\left(g_{ij} - G_{ij}\right), \tag{3.68}$$

and for the orthogonal base vectors, the transformation to the Cartesian coordinate system denoted with $(\tilde{\cdot})$ is given by

$$\tilde{E}_{ij} = \frac{E_{ij}}{\|\boldsymbol{G}_i\|_2 \|\boldsymbol{G}_j\|_2}, \tag{3.69}$$

where $\|(\cdot)\|_2$ is the Euclidean norm. By substituting geometric relations into the strain tensor, the individual components of the tensor can be derived. During the derivation, additional simplifications are made assuming that only a slender beam is considered ($b, h << L$ where b and h are cross-sectional dimensions and L is a length of the beam) resulting in the following equations for the diagonal term E_{11}

$$\begin{aligned} E_{11} \;=\; & \underbrace{\frac{1}{2}(a_{11} - A_{11})}_{\epsilon} + \theta^2 \underbrace{\boldsymbol{a}_{2,1} \cdot \boldsymbol{a}_1 - \boldsymbol{A}_{2,1} \cdot \boldsymbol{A}_1}_{\kappa_{21}} \\ & + \theta^3 \underbrace{\boldsymbol{a}_{3,1} \cdot \boldsymbol{a}_1 - \boldsymbol{A}_{3,1} \cdot \boldsymbol{A}_1}_{\kappa_{31}}. \end{aligned} \tag{3.70}$$

The remaining diagonal terms $E_{\alpha\alpha}$ as well as the shear term E_{23} are equal to zero. This yields from the Bernoulli assumptions (undeformable cross–section). The off-diagonal terms E_{12}, E_{13} yield

$$E_{1\alpha} \;=\; \frac{1}{2}\theta^\beta \underbrace{(a_{\beta,1} \cdot a_\alpha - (A_{\beta,1} \cdot A_\alpha)}_{\kappa_{\beta\alpha}}, \tag{3.71}$$

where $(\alpha, \beta) \in \{(2,3),(3,2)\}$.

Constitutive equations

The energetically conjugated stress tensor to the Green-Lagrange strain tensor is the second Piola-Kirchhoff tensor $\boldsymbol{S}$. Elastic isotropic material is considered within this work together with St. Venant-Kirchhoff material model. As the beam formulation is reduced to the centerline and Bernoulli theory is assumed, the shear forces $\tilde{S}_{23}$ and $\tilde{S}_{32}$ and normal forces $\tilde{S}_{22}$, $\tilde{S}_{33}$ vanish and the full constitutive relation can be reduced to

$$\begin{bmatrix} \tilde{S}^{11} \\ \tilde{S}^{12} \\ \tilde{S}^{13} \end{bmatrix} = \underbrace{\begin{bmatrix} E & 0 & 0 \\ 0 & G & 0 \\ 0 & 0 & G \end{bmatrix}}_{\boldsymbol{D}} \begin{bmatrix} \tilde{E}^{11} \\ \tilde{E}^{12} \\ \tilde{E}^{13} \end{bmatrix}, \tag{3.72}$$

where E is Young's modulus, G is the shear modulus and $\boldsymbol{D}$ is a reduced elasticity matrix.

Principle of Virtual Work

The system is in equilibrium when the overall virtual work of the system is equal to zero

$$\delta W = -\delta W_{int} + \delta W_{ext} = 0. \tag{3.73}$$

The internal end external virtual work of the system are given by

$$\delta W_{int} = \int_V \boldsymbol{S} : \delta \boldsymbol{E} dx, \tag{3.74}$$

$$\delta W_{ext} = \int_{\Gamma_p} \boldsymbol{t} : \delta \boldsymbol{u} dx + \int_V \rho_0 \boldsymbol{B} : \delta \boldsymbol{u} dx. \tag{3.75}$$

The external virtual work depends on the boundary tractions $\boldsymbol{t}$, body forces $\boldsymbol{B}$ and material density ρ_0.

By substituting expressions for the virtual Green-Lagrange strain tensor obtained from (3.68) into constitutive relations (3.72) and performing linearization the nonlinear equilibrium equations in the form $\boldsymbol{F}^{int}\boldsymbol{r} = \boldsymbol{F}^{ext}$ are obtained. They are solved using the Newton-Raphson method. Linearization of the above equation leads to

$$\sum_s K_{rs} \Delta u_s = -R_r, \tag{3.76}$$

where Δu_s are the displacement increments and

$$R_r = -(F_r^{int} + F_r^{ext}) \tag{3.77}$$

$$= \frac{\partial W_{int}}{\partial u_r} + \frac{\partial W_{ext}}{\partial u_r}, \tag{3.78}$$

$$K_{rs} = \frac{\partial R_r}{\partial u_s} = \frac{\partial^2 W_{int}}{\partial u_r \partial u_s}. \tag{3.79}$$

The fully derived equations for the presented beam formulation including a stress post-processing of the initially curved beams can be found in [14].

3.3. Implementation

All the presented beam formulations have been implemented in order to evaluate their performance and to enable further research. Two different platforms for the analysis have been used, namely, Matlab [55] and OOFEM [56].

3.3.1. Matlab

Matlab is a platform for programming and numeric computations. This environment has been chosen as the main tool for the initial implementation and for the evaluation of the newly developed methods. The main reasons for the use of Matlab are the simplicity of the implementation and the robustness of the system.

Two-dimensional Timoshenko beam formulation with locking treatment and Bernoulli beam formulation are implemented using Matlab. NURBS package [57] for Octave [58] is used for handling NURBS. The refinement algorithms are implemented within the code, thus only the initial mesh with analysis data (such as material and cross-section characteristics, boundary conditions and required refinement) need to be specified on the input. Note that the specification of the initial mesh (given by a knot vector, an approximation order, and control points' coordinates and weights) determines the initial basis and geometry. The subsequent use of refinement algorithms preserves the geometry, while the basis is enriched.

All the elements implemented within the Matlab follow a similar framework. The definition of the input data is followed by the generation of the desired basis using refinement algorithms. Along with the mesh refinement, necessary localization matrices and vectors keeping the boundary conditions are assembled. Consequently, a constitutive matrix is calculated using the cross-sectional and material characteristics defined on the input. Despite the fact, that all the problems analyzed in this thesis involve only one-patch geometries, the implementation assumes a general number of patches. In general, the patch stiffness matrix and patch load vector are evaluated within a cycle through knot spans nested within a cycle through patches. Functions for the evaluation of element matrices and vectors contain another cycle - through integration points. The evaluation of the stiffness matrix is slightly modified in the case of DSG-based and $\bar{\mathrm{B}}$-based element as the stiffness matrices are evaluated at the patch level.

After assembly of the global stiffness matrix and right-hand side vector, the problem is solved using Matlab built-in function for the solution of the linear system of equations. Additionally to the calculation of the control point values, post-processing routines for the deformed shape visualisation and internal forces evaluation are implemented.

Obviously, an adequate extension of the described framework is necessary to support a geometrically nonlinear Bernoulli beam element. The nonlinear system of equations is solved in incremental steps using displacement control. Moreover, the attributes which are constant during the run of the analysis are calculated in advance and stored in order to make the implementation more efficient.

3.3.2. OOFEM

In order to provide the implemented elements to a wider range of users, both two- and three-dimensional Timoshenko beam formulations including the discussed locking treatment (reduced integration, $\bar{\mathrm{B}}$ method, and DSG method) were implemented within the existing finite element code OOFEM. For easier data input, an automatic generator of the input file directly from CAD system has been developed. Moreover, the simple visualisation of the results within CAD was implemented for a two-dimensional beam element resulting in a prototype of the interactive design tool.

Implementation in OOFEM follows the framework already implemented within the code [36]. Thanks to an object-oriented design, generic methods such as stiffness matrix evaluation are inherited and reused, and only element-specific methods need to be provided. A separate class was defined for each implemented element to provide an implementation of a specific strain-displacement matrix $\boldsymbol{B}$, set up integration rules, etc. As the Timoshenko beam formulation assumes a local coordinate system, new classes supporting the methods for the interpolation along the curve in two and three dimensions were developed. A mesh after required refinement needs to be provided in the input file, as the refinement algorithms are not implemented within the code.

A connection with CAD system Rhinoceros (Rhino) [59] was developed to facilitate an easier generation of an input file. The geometry representation in Rhino is based on NURBS, moreover, Rhino enables plug-in development and use of built-in tool Grasshopper [60]. Grasshopper is a visual programming interface within Rhino that can directly access NURBS geometry and even perform some operations on geometry, such as mesh refinement. In addition, visual programming is intelligible even to a user with no programming background, so the user can define additional analysis data at this level.

The developed input file generator allows choosing a NURBS curve geometry modelled in Rhino. The geometry data are automatically passed to the Grasshopper where additional analysis data (required refinement, element type, boundary conditions, material, and cross-section characteristics) need to be specified. Once all the analysis data are collected, the input file for OOFEM is automatically generated using the python script within Grasshopper together with other available Grasshopper tools.

As the possibility of seamless connection between CAD and FEA is the major benefit of IGA, a prototype of an interactive design tool was developed. This goal can be achieved even without the use of the isogeometric approach (see e.g. [61]); nevertheless, the costly transformations between CAD and FEM are necessary for such a workflow. The workflow of the developed tool is illustrated in Figure 3.7. The python script within the implemented input file generator discussed above was extended in order to directly pass the input file to OOFEM and run the analysis. When the analysis is finished, the results in a form of NURBS representation of displacements and post-processed internal variables are uploaded back to the Grasshopper, where the visualization of the results is carried out. Schematic illustration of Grasshopper environment with results visualized in Rhino can be seen in Figure 3.8.

A very important feature of the developed tool is, that the Grasshopper (and in turn also OOFEM) recomputes the results immediately when something changes. No

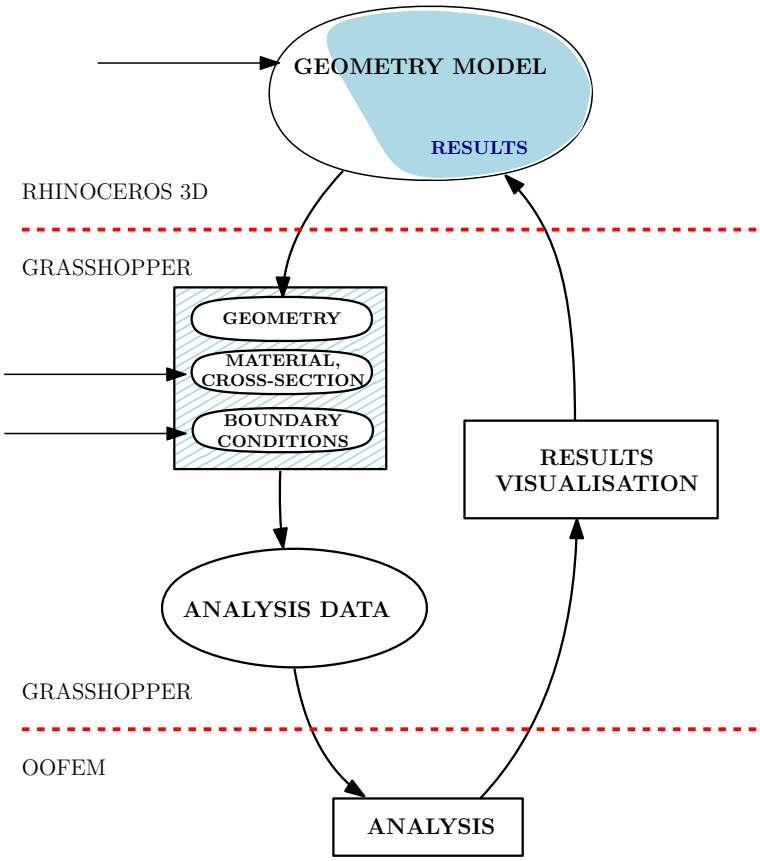

Figure 3.7.: Schema of the interactive design tool.

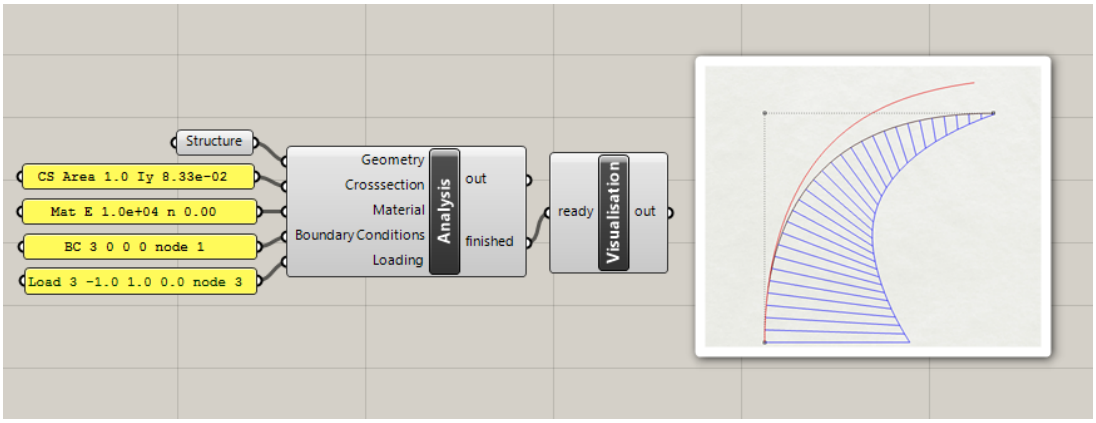

Figure 3.8.: The interactive design tool.

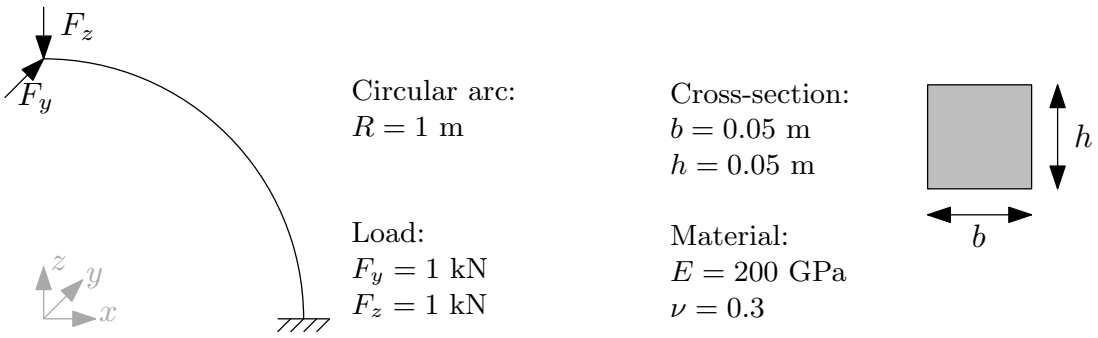

Figure 3.9.: Circular cantilever geometry.

matter whether the user adjusts the geometry or changes the boundary conditions, the results are interactively updated. This provides immediate knowledge about the behavior of the designed structure already in the conceptual design phase and eases the process of finding optimal design.

3.4. Numerical examples

Several benchmark examples have been selected to demonstrate the implementation of the presented elements. Timoshenko beam formulation including discussed locking treatment is verified using both two-dimensional and fully three-dimensional examples. The fundamental example of the circular cantilever is used also for the verification of the implementation of the Bernoulli beam. Additionally, a complex benchmark problem is assessed to verify the Bernoulli beam implementation including geometrically nonlinear effects.

3.4.1. Timoshenko beam

Circular cantilever

In order to evaluate the correctness of the implementation, a simple problem of a circular cantilever beam was assessed. Two load cases were studied: in-plane force load and out-of-plane force load, see Figure 3.9. The first load case was evaluated using both two- and three-dimensional formulations yielding the same results. The three-dimensional formulation is necessary for the second load case. Cubic NURBS with C^2 continuity across knot spans were used for the geometry and unknowns approximation. Timoshenko beam formulation without locking treatment (FI) was compared to the formulations with discussed locking removal techniques: reduced integration (RI), DSG method (DSG), and $\bar{\mathrm{B}}$ method (BBAR). Moreover, the quartic approximation with no locking treatment was used to demonstrate the ability of higher-order NURBS basis functions to alleviate the locking. Additionally to the isogeometric elements, the results using standard FEM straight beam element with cubic approximation [62] (FEM)

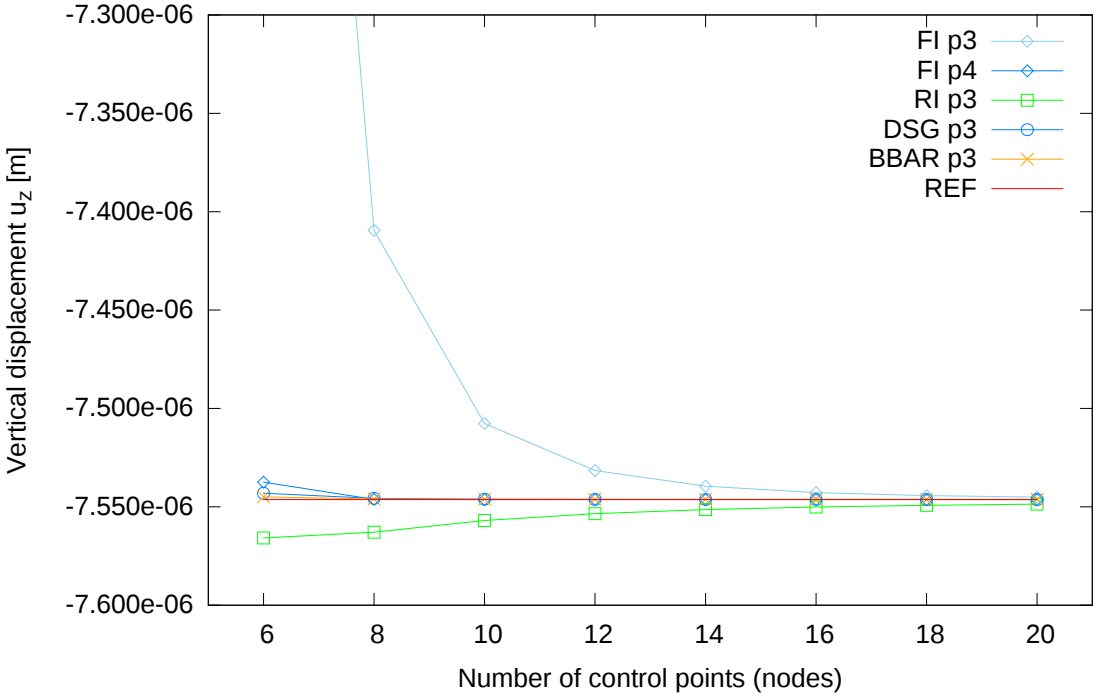

Figure 3.10.: Circular cantilever, in-plane load: Numerical locking of NURBS beam element with no locking treatment compared to locking removal techniques.

available in OOFEM, which is naturally locking free, were included. The reference solutions were calculated by means of the principle of virtual forces. The vertical tip displacement for the first load case is

$$\begin{aligned} u_z &= \int_0^{\frac{\pi}{2}} \frac{1}{EA} N\bar{N} + \frac{1}{GA_n} Q_n \bar{Q}_n + \frac{1}{EI_b} M_b \bar{M}_b \, d\alpha \\ &= \int_0^{\frac{\pi}{2}} \frac{1}{EA} cos\alpha(-cos\alpha) + \frac{1}{GA_n} sin\alpha(-sin\alpha) + \frac{1}{EI_b} cos\alpha(-cos\alpha) \, d\alpha \\ &= \frac{\pi}{4}\left(\frac{1}{EA} + \frac{1}{GA_n} + \frac{1}{EI_b}\right) \\ &= -7.5463 \cdot 10^{-6} \text{ m}. \end{aligned} \tag{3.80}$$

Out-of-plane displacement for the second load case is

$$\begin{aligned} u_y &= \int_0^{\frac{\pi}{2}} \frac{1}{GA_b} Q_b \bar{Q}_b + \frac{1}{EI_n} M_n \bar{M}_n + \frac{1}{GI_k} M_t \bar{M}_t \, d\alpha \\ &= \int_0^{\frac{\pi}{2}} \frac{1}{GA_b} + \frac{1}{EI_n}(-cos\alpha)(-cos\alpha) + \frac{1}{GI_k}(1 - sin\alpha)(1 - sin\alpha) \, d\alpha \\ &= \frac{\pi}{2GA_b} + \frac{\pi}{4EI_n} + \frac{1}{GI_k}\left(\frac{3\pi}{4} - 2\right) \\ &= 1.1995 \cdot 10^{-5} \text{ m}. \end{aligned} \tag{3.81}$$

The deterioration of the solution caused by numerical locking can be observed in Figure 3.10. The beam element is too stiff especially in the case of the coarse mesh. It

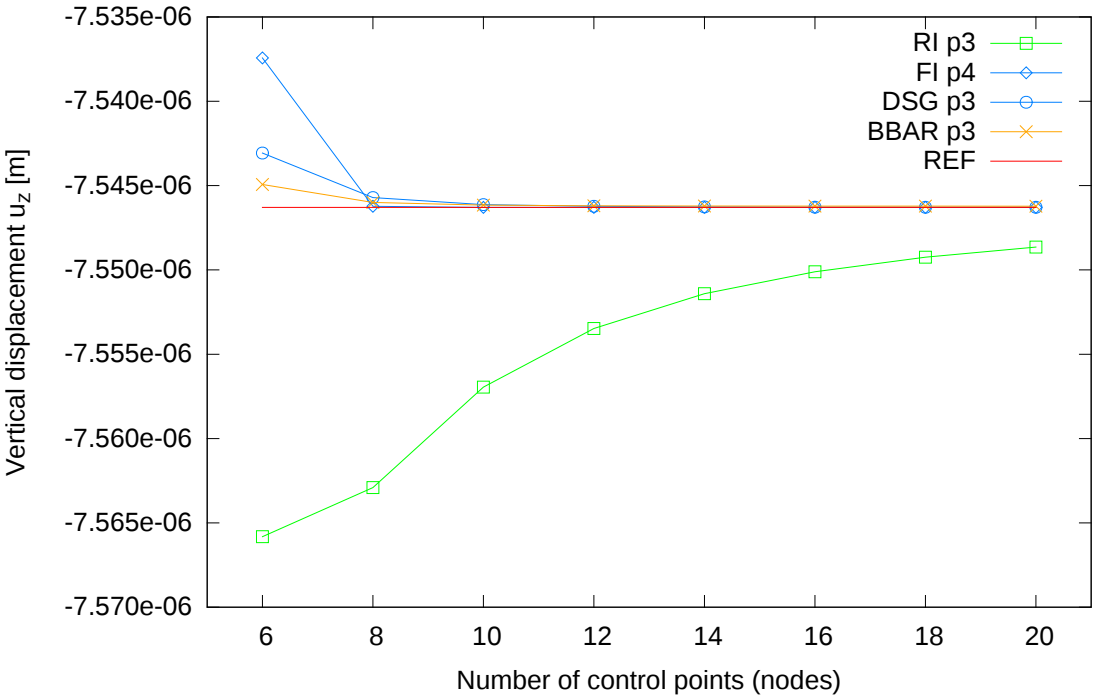

Figure 3.11.: Circular cantilever, in-plane load: Comparison of locking removal techniques.

can be seen, that use of the higher-order approximation significantly alleviate the locking problem. In more detail, this behavior can be studied in Figure 3.11. In the case of the mesh consisting of eight control points and more, the quartic approximation shows even better performance than the formulations with locking treatment where only cubic NURBS basis is used. The comparison of locking treatment can be also observed in Figure 3.11. All the presented methods alleviate locking effects; the best results are obtained using $\bar{\mathrm{B}}$ method. The Discrete shear gap method shows very good performance. The comparison of locking removal techniques to a standard FEM element is plotted in Figure 3.12. As expected, a significantly higher number of nodes has been necessary in order to achieve the accuracy of the isogeometric formulation.

Helix

A problem of helicoidal cantilever [12] was assessed in order to evaluate the performance in a fully three-dimensional case. The geometry is illustrated in Figure 3.16. The helix of radius $R = 2$ m and height $H = 3$ m with hollow circular cross-section is subjected to the constant vertical distributed load $f = 3$ kN/m. Geometry was modelled using cubic and quartic NURBS approximation with C^{p-1} continuity across knot spans.

A convergence of the vertical tip displacement is studied. The reference solution is calculated by means of the principle of virtual forces. The position vector of an arbitrary point on helix centerline can be expressed using angular coordinate $\varphi \in$

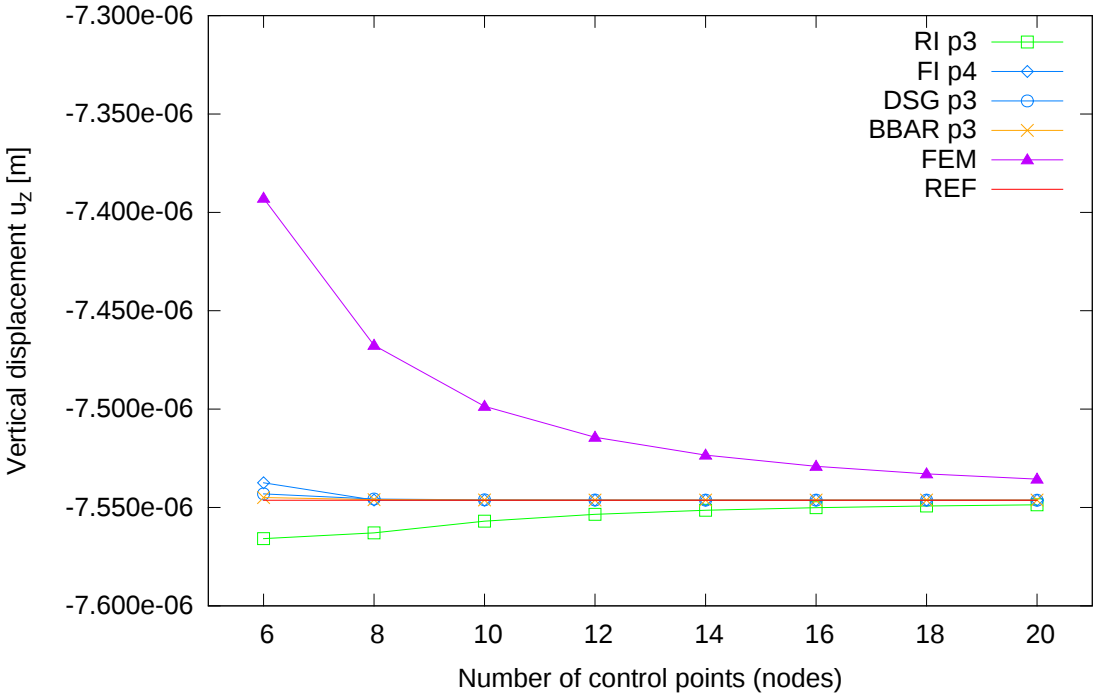

Figure 3.12.: Circular cantilever, in-plane load: Comparison of standard FEM with isogeometric formulations.

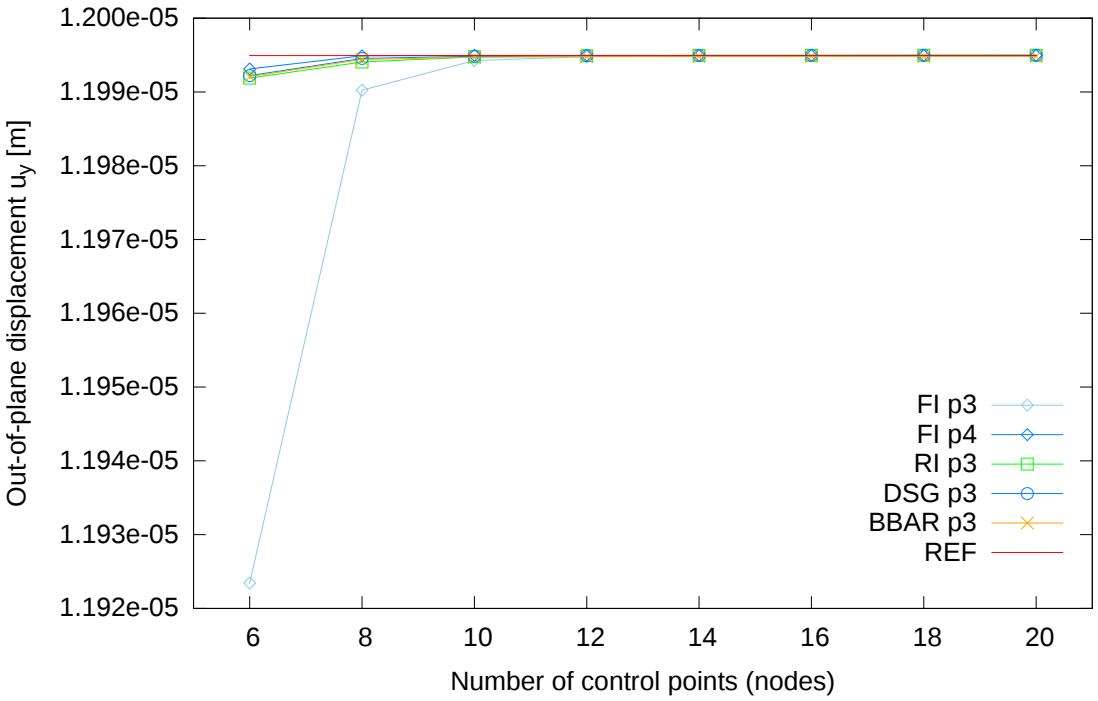

Figure 3.13.: Circular cantilever, out-of-plane load: Numerical locking of NURBS beam element with no locking treatment compared to locking removal techniques.

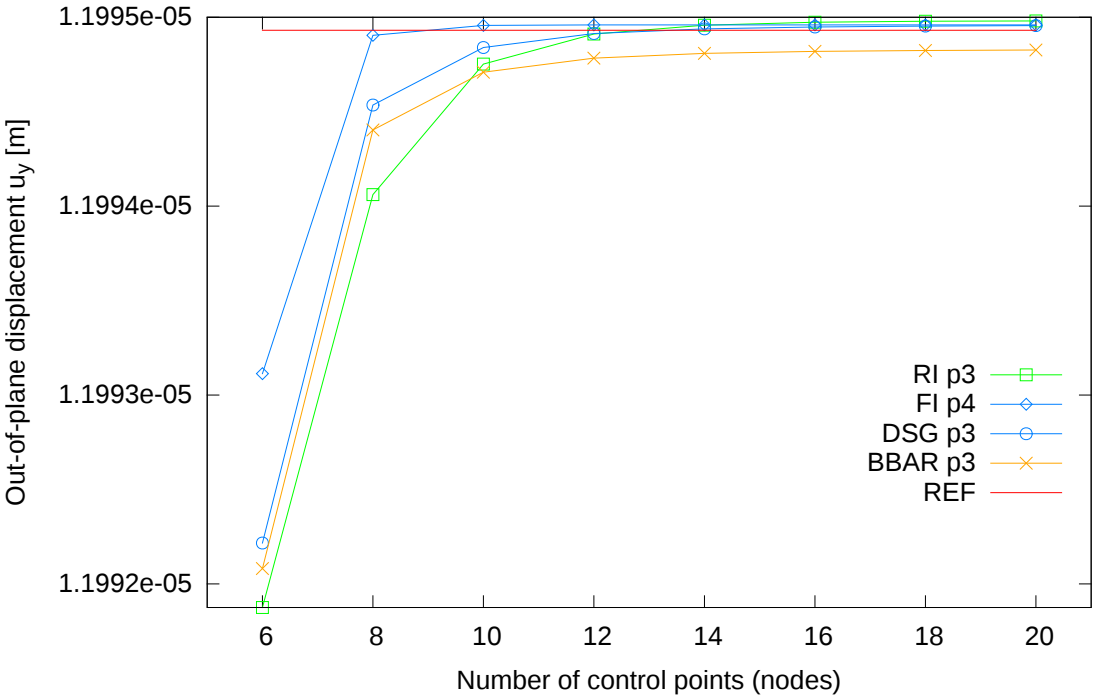

Figure 3.14.: Circular cantilever, out-of-plane load: Comparison of locking removal techniques.

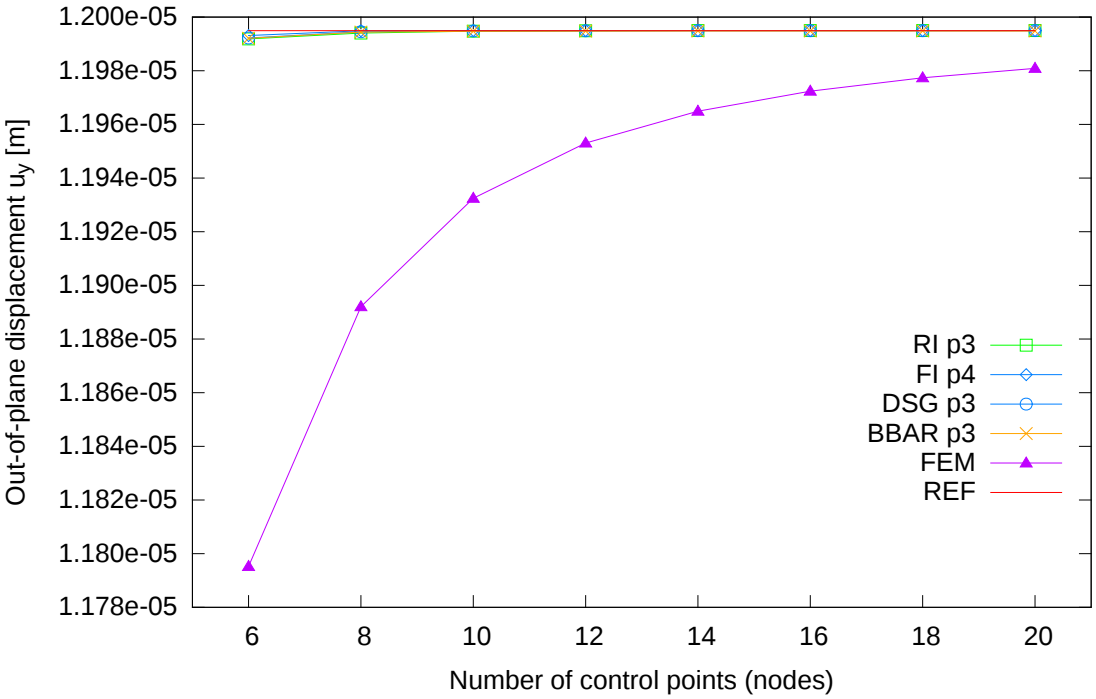

Figure 3.15.: Circular cantilever, out-of-plane load: Comparison of standard FEM with isogeometric formulations.

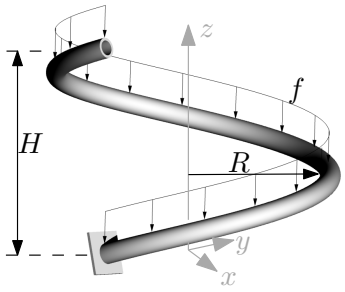

Helicoidal spring:
$R = 2$ m
$H = 3$ m

Load:
$f = 3$ kN/m

Cross-section:
$r_1 = 0.11$ m
$r_2 = 0.15$ m

Material:
$E = 200$ GPa
$\nu = 0.3$

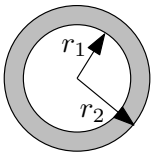

Figure 3.16.: Helicoidal spring geometry.

$\langle 0, 2\pi \rangle$ as

$$\boldsymbol{x}(\varphi) = \left\{ \begin{array}{c} x(\varphi) \\ y(\varphi) \\ z(\varphi) \end{array} \right\} = \left\{ \begin{array}{c} 2cos\varphi \\ 2sin\varphi \\ \dfrac{3\varphi}{2\pi} \end{array} \right\}. \tag{3.82}$$

A differential moment at point with angular coordinate φ caused by differential uniform load $d\boldsymbol{f} = \boldsymbol{f} ds$ acting at point with angular coordinate α is

$$d\boldsymbol{M}(\varphi, \alpha) = \boldsymbol{r}(\varphi, \alpha) \times d\boldsymbol{f} = (\boldsymbol{x}(\alpha) - \boldsymbol{x}(\varphi)) \times d\boldsymbol{f}, \tag{3.83}$$

where in our case $d\boldsymbol{f} = [0, 0, -3000] ds$. The moment vector is then calculated as a sum of differential contributions from φ to the free end ($\varphi = 2\pi$)

$$\boldsymbol{M}_g(\varphi) = \int_{\varphi}^{2\pi} (d\boldsymbol{M}(\varphi, \alpha) J) \; d\alpha, \tag{3.84}$$

where $J = \frac{L}{2\pi}$ is Jacobian of transformation between α and s coordinate. Similarly, a moment vector at point with angular coordinate φ caused by a unit vertical force at a tip of the helix is given as

$$\bar{\boldsymbol{M}}_g(\varphi) = \boldsymbol{r}(\varphi, 2\pi) \times \boldsymbol{F} = (\boldsymbol{x}(2\pi) - \boldsymbol{x}(\varphi)) \times \boldsymbol{F}, \tag{3.85}$$

where $\boldsymbol{F} = [0, 0, 1]$. For simplicity, the dependence on φ will be omitted in the subsequent derivations. Local moments associated to t, n, b are obtained using transformation matrix $\boldsymbol{T}$

$$\boldsymbol{M}_l = \left\{ \begin{array}{c} M_t \\ M_n \\ M_b \end{array} \right\} = \boldsymbol{T}\boldsymbol{M}_g \quad \bar{\boldsymbol{M}}_l = \boldsymbol{T}\bar{\boldsymbol{M}}_g. \tag{3.86}$$

Transformation matrix $\boldsymbol{T}$ is constructed from unit vectors in direction of tangent, normal and binormal vectors. Global internal forces $\boldsymbol{F}_g$ and $\bar{\boldsymbol{F}}_g$ caused by the continuous loading and by unit force, respectively, are given as

$$\boldsymbol{F}_g = \int_{\varphi}^{2\pi} (d\boldsymbol{f} J) \, d\alpha, \tag{3.87}$$

$$\bar{\boldsymbol{F}}_g = \boldsymbol{F}. \tag{3.88}$$

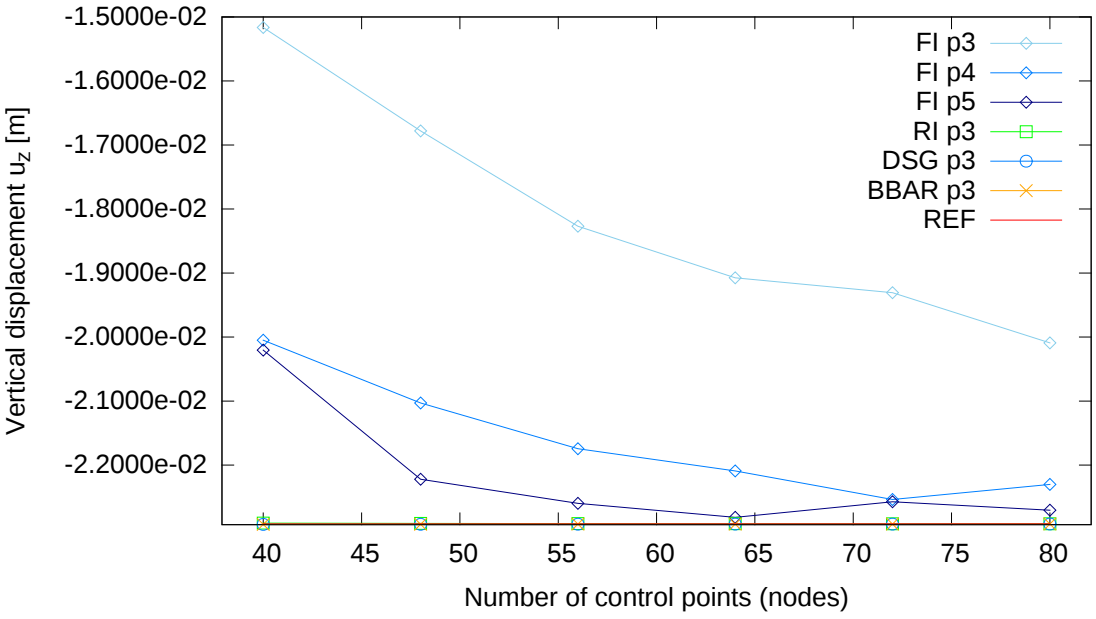

Figure 3.17.: Helicoidal cantilever: Numerical locking of NURBS beam element with no locking treatment compared to locking removal techniques.

Local internal forces are obtained using transformation matrix $\boldsymbol{T}$

$$\boldsymbol{F}_l = \left\{ \begin{array}{c} N \\ Q_n \\ Q_b \end{array} \right\} = \boldsymbol{T}\boldsymbol{F}_g, \quad \bar{\boldsymbol{F}}_l = \boldsymbol{T}\bar{\boldsymbol{F}}_g. \tag{3.89}$$

Finally, a vertical tip displacement is obtained as

$$\begin{aligned} u_z &= \int_0^{2\pi} \left(\frac{1}{EA} N\bar{N} + \frac{1}{GA_n} Q_n \bar{Q}_n + \frac{1}{GA_b} Q_b \bar{Q}_b \right) J \, d\varphi \\ &\quad + \int_0^{2\pi} \left(\frac{1}{GI_k} M_t \bar{M}_t + \frac{1}{EI_n} M_n \bar{M}_n + \frac{1}{EI_b} M_b \bar{M}_b \right) J \, d\varphi \\ &= -2.2920 \cdot 10^{-2} \text{ m}. \end{aligned} \tag{3.90}$$

In Figure 3.17 the numerical locking is documented. A significant error in the solution is observed when the NURBS element with a cubic approximation is used. The possibility of alleviation of the locking effects by the use of a higher approximation degree can be also observed. The performance of the presented locking removal techniques is provided in Figure 3.18. All the presented methods alleviate locking effects; the best results are obtained using discrete shear gap method or $\bar{\text{B}}$ method. According to the expectations, the higher approximation order results in better accuracy. Similarly to the previous example, straight FEM elements do not achieve the accuracy of the isogeometric formulations, see Figure 3.19 for the comparison.

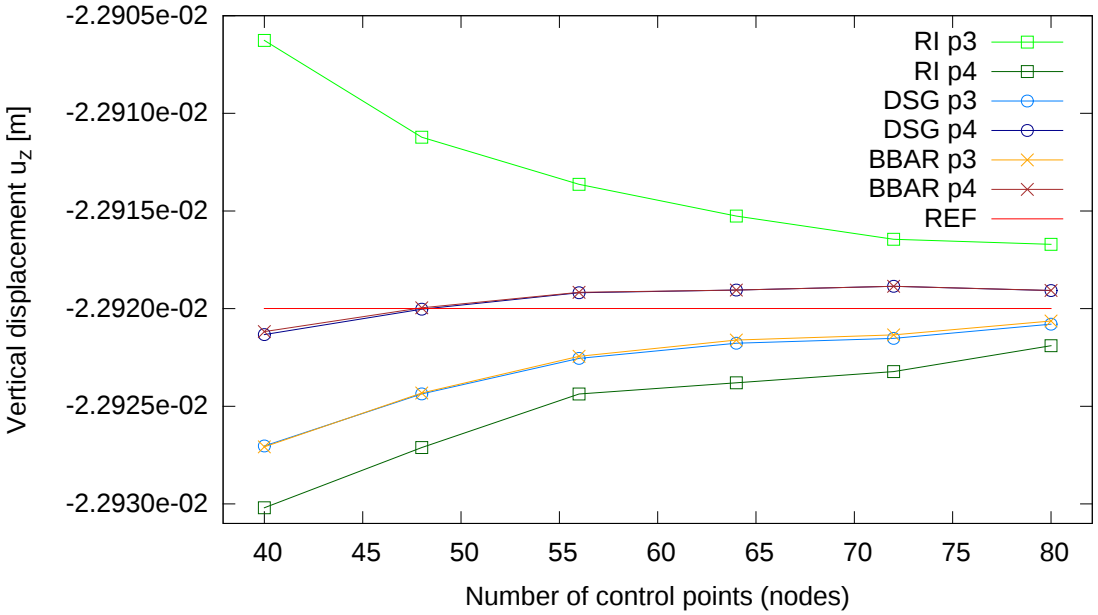

Figure 3.18.: Helicoidal cantilever: Comparison of locking removal techniques.

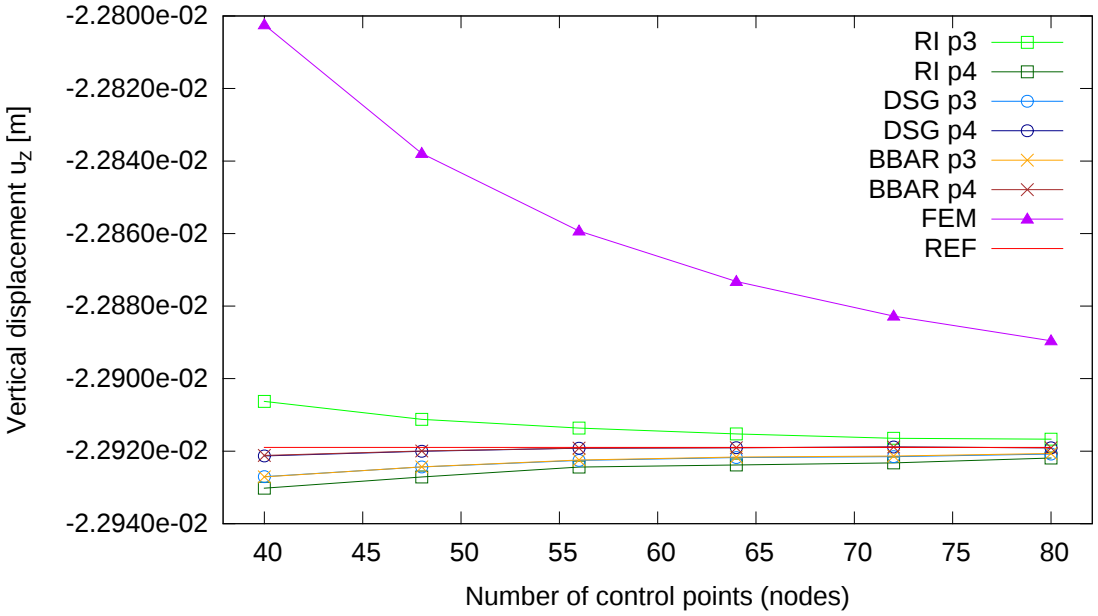

Figure 3.19.: Helicoidal cantilever: Comparison of isogeometric formulations with standard FEM straight beam element.

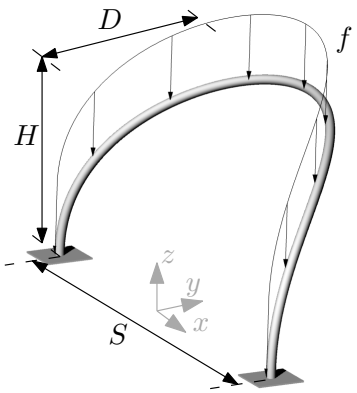

Out of plane arc:
$S = 20$ m
$H = 8.75$ m
$D = 6.38$ m

Load:
$f = 5$ kN/m

Cross-section:
$r_1 = 0.1$ m
$r_2 = 0.2$ m

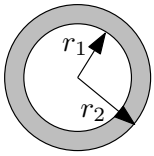

Material:
$E = 200$ GPa
$\nu = 0.3$

Figure 3.20.: Out of plane arc geometry.

Out of plane arc

In the case of the helicoidal cantilever, both the curvature and torsion are constant. A geometry with variable torsion and curvature along the beam length was tested using the out of plane arc problem [12]. An initial geometry is approximated with quartic B-spline functions. The corresponding knot span is $\Xi = \{0,0,0,0,0,1,1,1,1,1\}$. The following control points

$$\begin{aligned} C_1 &= \{0,10,0\}, \\ C_2 &= \{0,10,10\}, \\ C_3 &= \{17,0,10\}, \\ C_4 &= \{0,-10,10\}, \\ C_5 &= \{0,-10,0\} \end{aligned} \tag{3.91}$$

are associated with equal weights $w_i = 1$. These settings result in the arc with height $H = 8.75$ m spanning over span $S = 20$ m, which is pulled out of the plane by $D = 6.38$ m. The beam is subjected to the constant vertical load $f = 5$ kN/m. See Figure 3.20 for the illustration of the problem.

A convergence of the vertical displacement of the middle of the beam is studied; the reference solution is the average of the solutions obtained by formulations with $\bar{\mathrm{B}}$ and DSG locking treatment on a fine mesh approximated with quartic NURBS consisting of 400 control points. The deterioration of the solution due to the numerical locking as well as the alleviation of the locking phenomena by use of the higher-order approximations can be observed in Figure 3.21. A detailed plot is provided in Figure 3.22. The very good performance of $\bar{\mathrm{B}}$ method, as well as DSG method, can be observed. The comparison with standard straight FEM element is given in Figure 3.23.

3.4.2. Bernoulli beam

Circular cantilever

The circular cantilever used for the evaluation of Timoshenko beam elements was also used to verify Bernoulli beam implementation (see Figure 3.9). NURBS of order

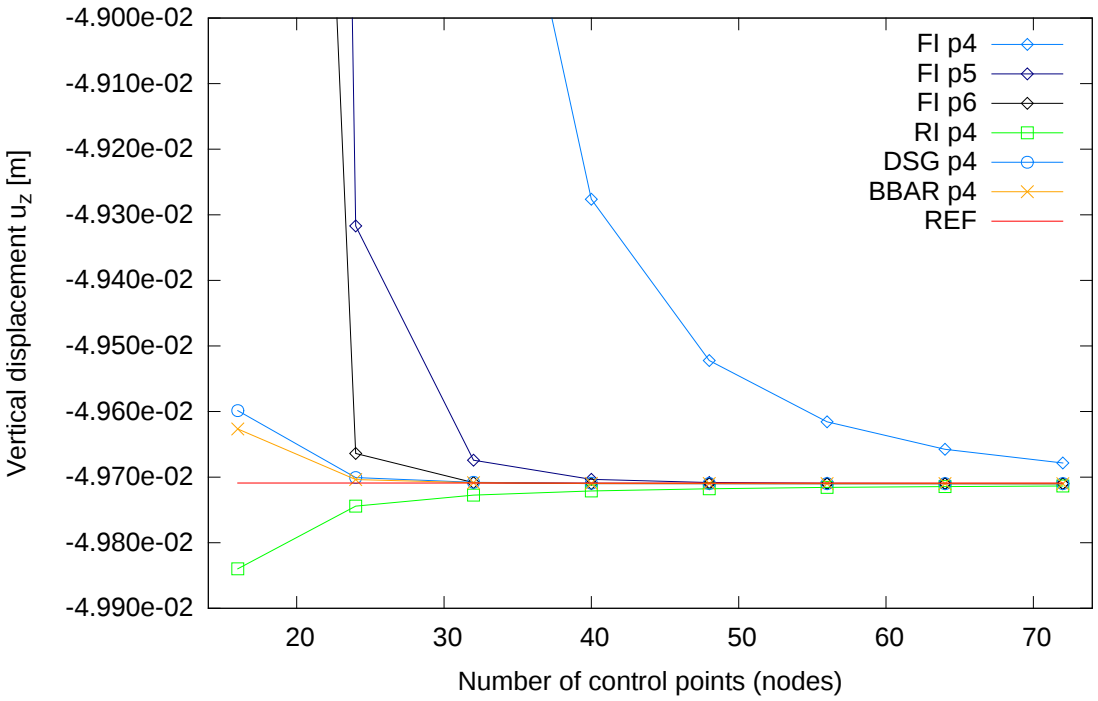

Figure 3.21.: Out of plane arc: Numerical locking of NURBS beam element with no locking treatment compared to locking removal techniques.

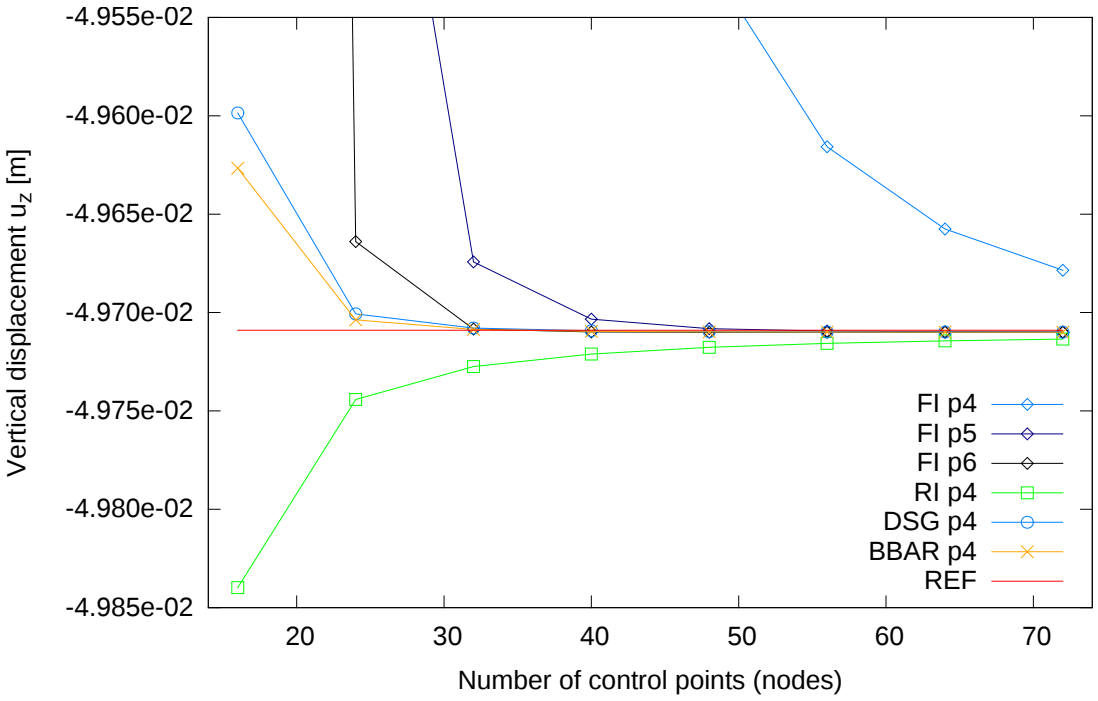

Figure 3.22.: Out of plane arc: Comparison of locking removal techniques.

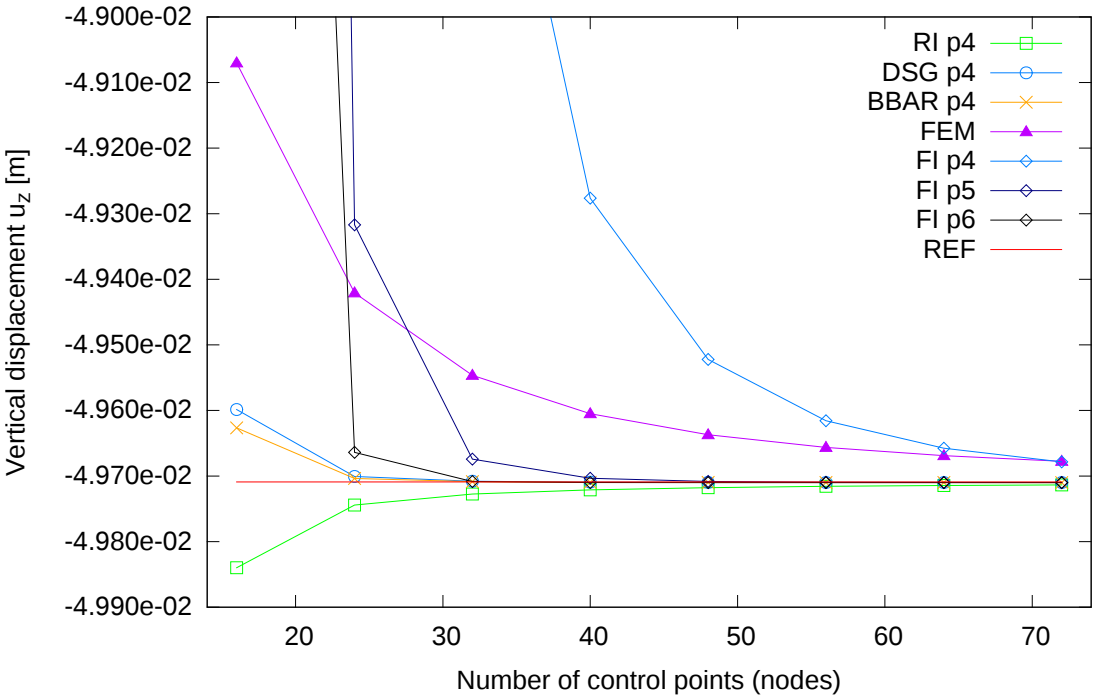

Figure 3.23.: Out of plane arc: Comparison of isogeometric formulations with standard FEM straight beam element.

$p = 3, 4$, and 5 with C^{p-1} continuity across knot spans were used as basis for the geometry and unknowns approximation. The reference solutions were again calculated by means of the principle of virtual forces yielding

$$\begin{aligned} u_z &= \int_0^{\frac{\pi}{2}} \frac{1}{EA} cos\alpha(-cos\alpha) + \frac{1}{EI_b} cos\alpha(-cos\alpha)\, d\alpha \\ &= \frac{\pi}{4}\left(\frac{1}{EA} + \frac{1}{EI_b}\right) \\ &= 7.5414 \cdot 10^{-6}\ \text{m}. \end{aligned} \tag{3.92}$$

for in-plane vertical tip load and

$$\begin{aligned} u_y &= \int_0^{\frac{\pi}{2}} \frac{1}{EI_n}(-cos\alpha)(-cos\alpha) + \frac{1}{GI_k}(1 - sin\alpha)(1 - sin\alpha)\, d\alpha \\ &= \frac{\pi}{4EI_n} + \frac{1}{GI_k}\left(\frac{3\pi}{4} - 2\right) \\ &= 1.1985 \cdot 10^{-5}\ \text{m}. \end{aligned} \tag{3.93}$$

for out-of-plane loading.

Obtained results for in-plane and out-of-plane loading are provided in Figure 3.24 and 3.25, respectively. Very good performance of the element is proven for both load cases. As expected, the higher the approximation order, the higher the accuracy of the solution.

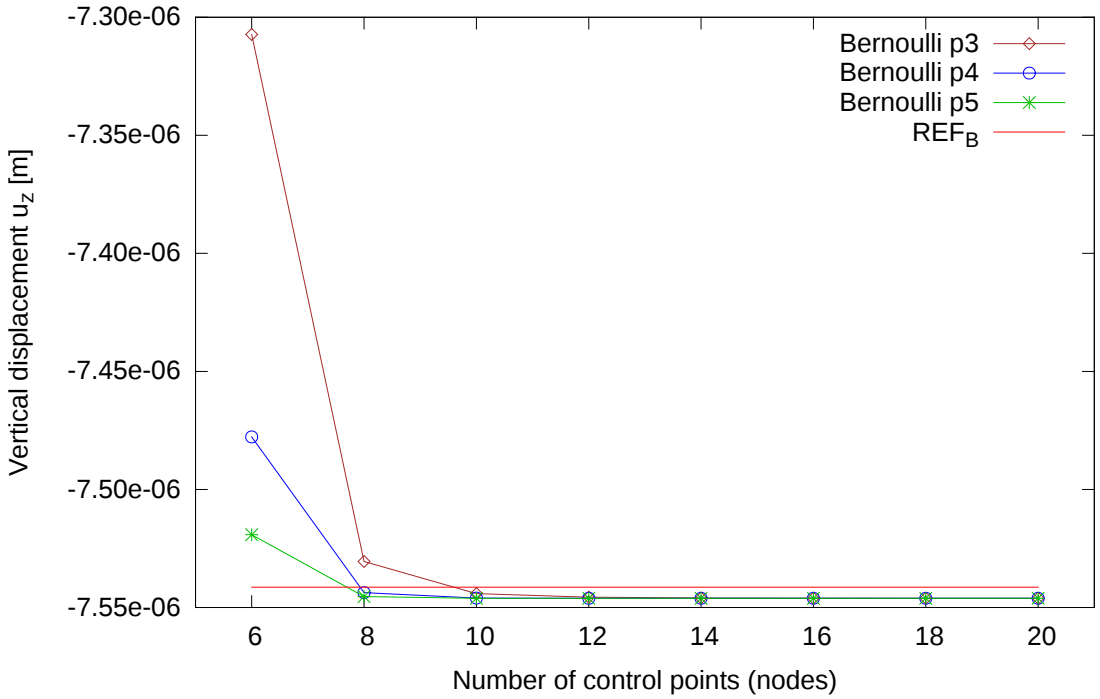

Figure 3.24.: Circular cantilever, in-plane load: Convergence of Bernoulli beam element for degree $p = 3, 4, 5$.

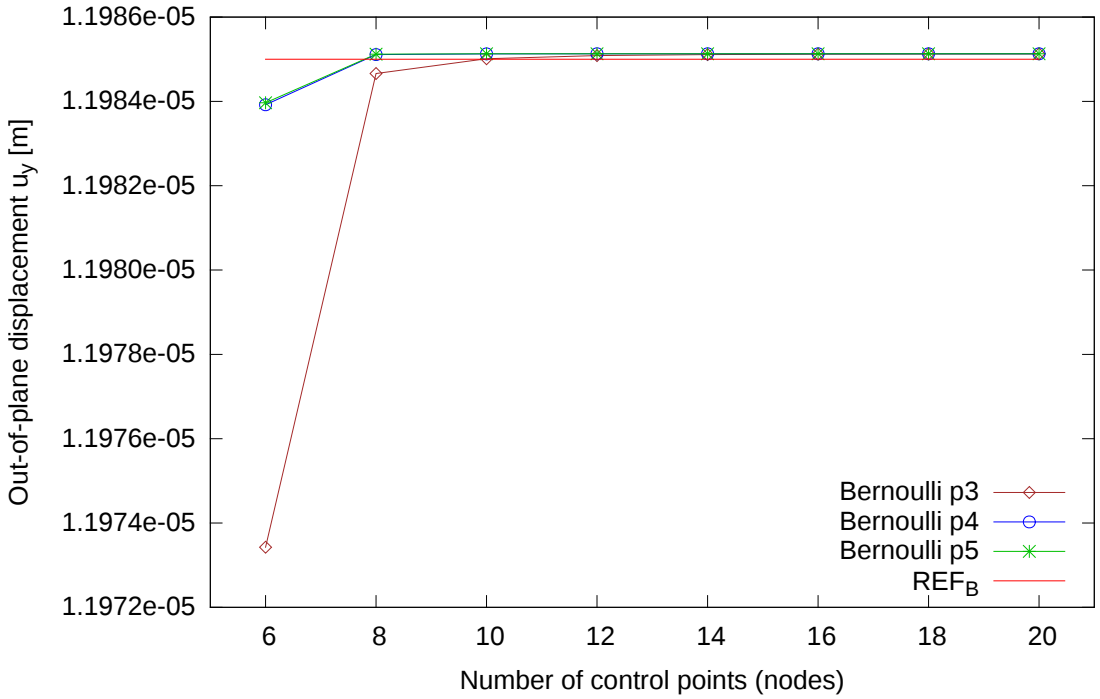

Figure 3.25.: Circular cantilever, out-of-plane load: Convergence of Bernoulli beam element for degree $p = 3, 4, 5$.

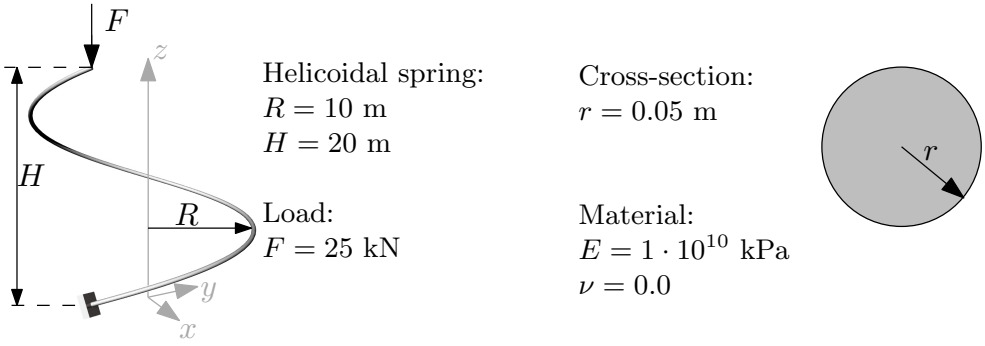

Figure 3.26.: Helicoidal spring geometry.

Helix

Similarly to the Timoshenko beam formulation, a helicoidal cantilever problem was evaluated to test the performance of the element in a fully three-dimensional case. In order to examine also geometrically-nonlinear behavior, a problem illustrated in Figure 3.26 was used for the possibility of comparison with the reference solution [14].

The problem was evaluated using cubic NURBS over 24 knot spans. The comparison of the obtained results with the reference solution is given in Figure 3.27, where the deformed geometry in each of the 20 load steps is also provided. Nicely matching results verify the implementation of the element.

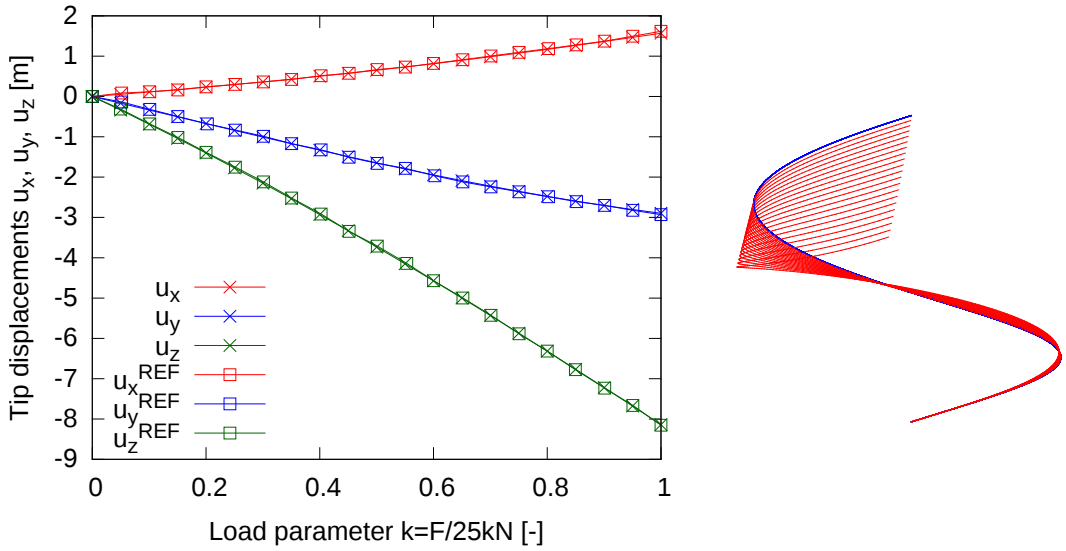

Figure 3.27.: Helicoidal cantilever: Comparison of Bernoulli beam implementation with reference solution [14] (left) and initial and deformed geometry for 20 load steps (right).

CHAPTER

FOUR

RESOLUTION OF CONCENTRATED LOADINGS

NURBS basis functions fail to represent the strong discontinuities in the numerical solution caused, for example, by the effect of a concentrated loading applied within a patch. Although some can argue that concentrated loadings do not exist and should be treated as distributed loads, their use has been established in practical analysis and design. In this section, the problem of concentrated loading is clearly demonstrated and possible solutions are proposed and evaluated using a simple two-dimensional straight Bernoulli beam example. Consequently, the novel method proposed for the solution of the problem of concentrated loadings is extended also for a curved Timoshenko beam element.

4.1. Two-dimensional straight Bernoulli beam

This chapter is based on the author's original work published in [63]. When the concentrated force/moment acts inside a patch, the continuity provided by the NURBS basis functions causes an inability to describe the discontinuities in internal forces. Such behavior is demonstrated using the example of a simply-supported Bernoulli beam subjected to a concentrated unit force/moment in the middle of the span. In the simplest case, only one knot span with a cubic B-spline approximation is used (Figure 4.1). The resulting bending moments for force and moment loads are plotted in Figures 4.2 and 4.3, respectively, where the error over the exact solution is clearly demonstrated.

It is important to emphasize that the cause lies in the continuity of basis functions; thus, the problem can generally not be solved by mesh refinement or degree elevation. This can be observed once again in Figures 4.2 and 4.3, where the results of analysis with a finer mesh and higher approximation order are also provided. It is obvious that the basis functions fail to describe the discontinuity at the knot span subjected to concentrated load; the error propagates to the neighbouring knot spans and beyond. Apparently, the error might be decreased and localized by knot refinement, but an excessive number of knot spans would be necessary for sufficiently good results and

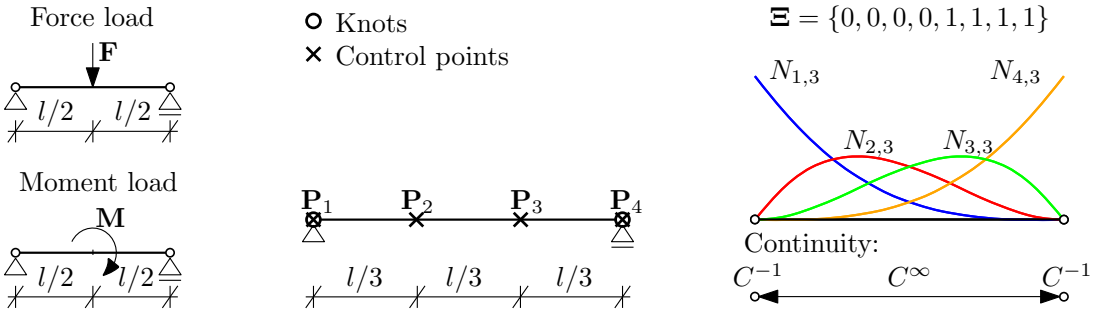

Figure 4.1.: Simply supported beam (Example 1) subjected to a concentrated force/ moment and its parametrization by cubic approximation over one knot span with corresponding B-spline basis functions.

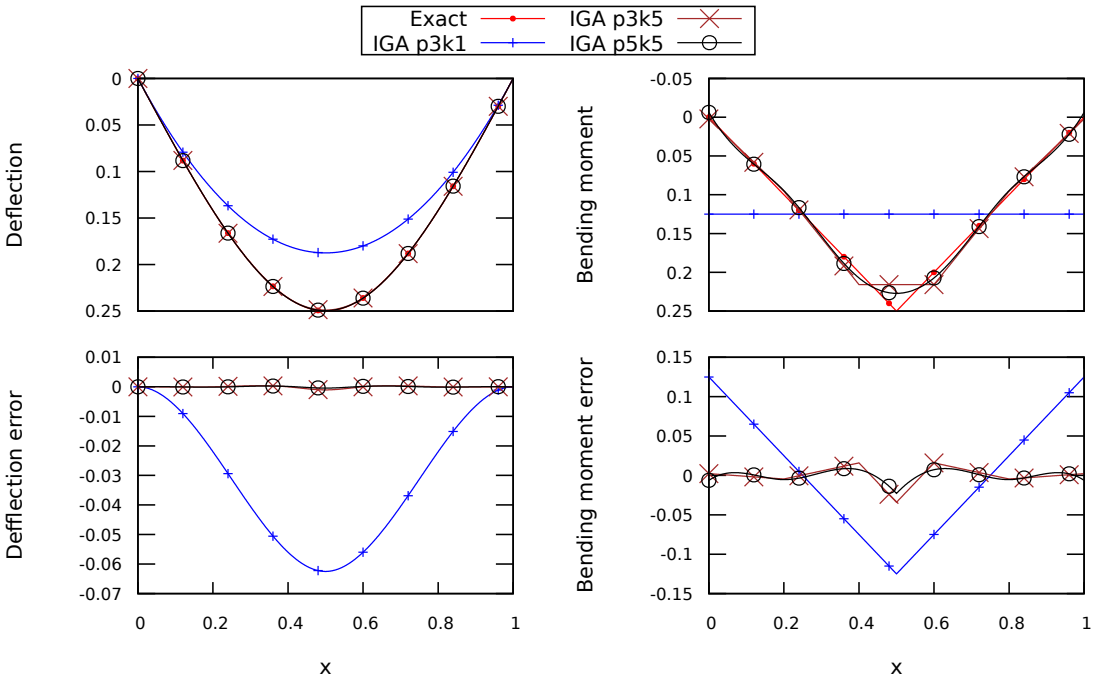

Figure 4.2.: Force load for Example 1 with numerical solution and error with respect to the exact solution for cubic approximation over one knot span (IGA p3k1), cubic approximation over five equidistant knot spans (IGA p3k5), and quintic approximation over five equidistant knot spans (IGA p5k5).

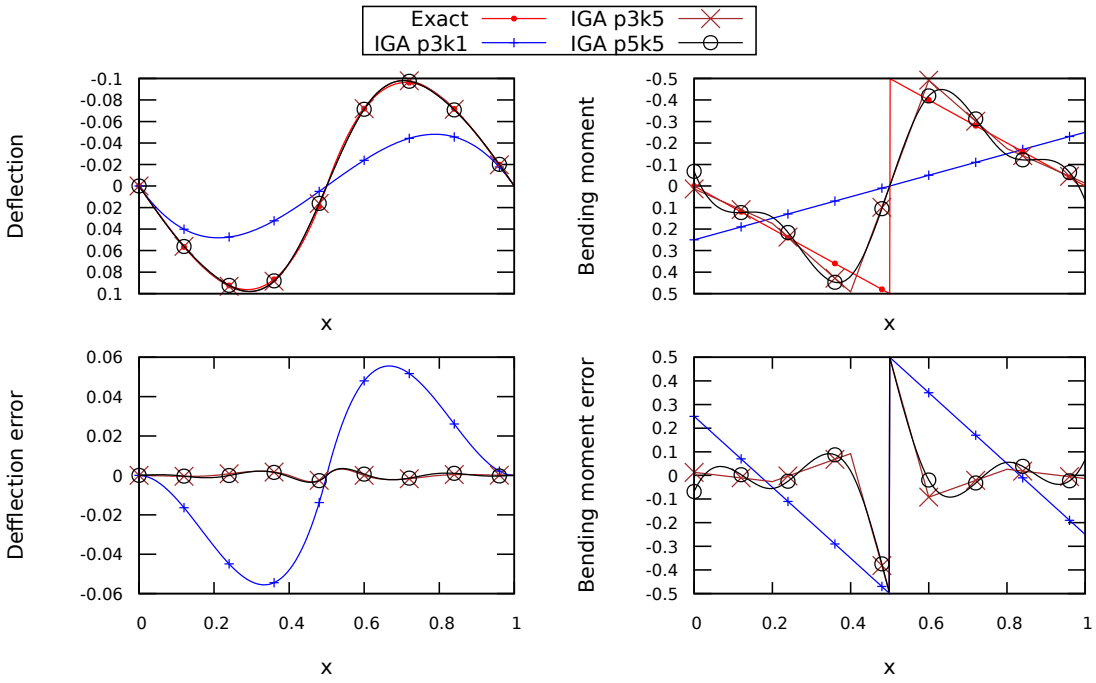

Figure 4.3.: Moment load for Example 1 with numerical solution and error with respect to the exact solution for cubic approximation over one knot span (IGA p3k1), cubic approximation over five knot spans (IGA p3k5), and quintic approximation over five knot spans (IGA p5k5).

the error would still not be eliminated completely.

Two different approaches for overcoming the problem are proposed and discussed in the following text. The first method uses standard procedures for lowering continuity at a particular point; the second is an original approach designed to solve the problem with no alteration of the initial B-spline basis functions. Both methodologies are demonstrated using the same example modelled with a single knot span with cubic approximation subjected to force or moment loadings.

4.1.1. Knot insertion and multiplication

Because the problem stated in the introduction to this section is rooted in continuity, the idea of lowering continuity is straightforward. This goal can be achieved easily with knot insertion and knot multiplication, see Section 2.3.3. The effect of knot insertion and knot multiplication on the approximation used is illustrated in Figure 4.4.

By applying knowledge of continuity aspects to the presented beam problem, the interpolation can be tailored by knot insertion (and multiplication) to match an exact solution. When a beam is subjected to concentrated force, the C^0-continuous bending moment is necessary at the force location. Since the bending moment is proportional to the second derivative of deflection w (3.54), a maximum of C^2-continuous approximation is required at the force location. As illustrated in Figure 4.4, C^2 continuity is

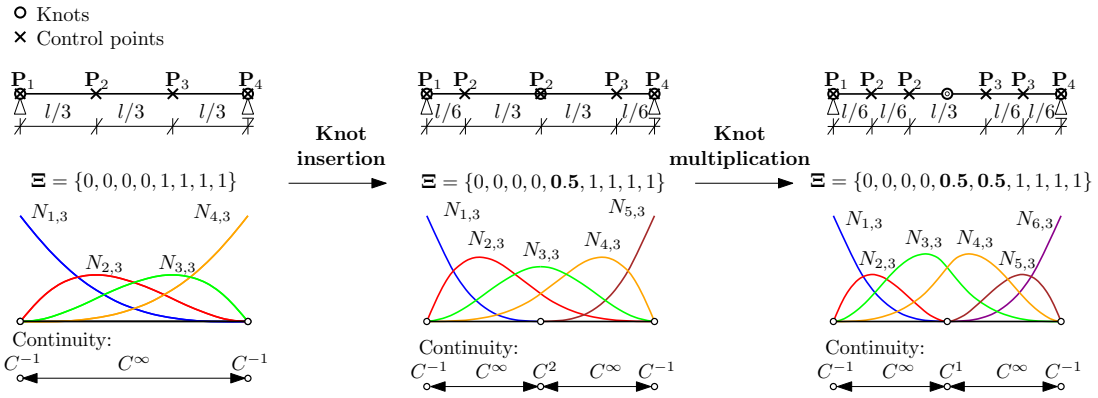

Figure 4.4.: Influence of knot insertion and knot multiplication on cubic NURBS approximation over one knot span.

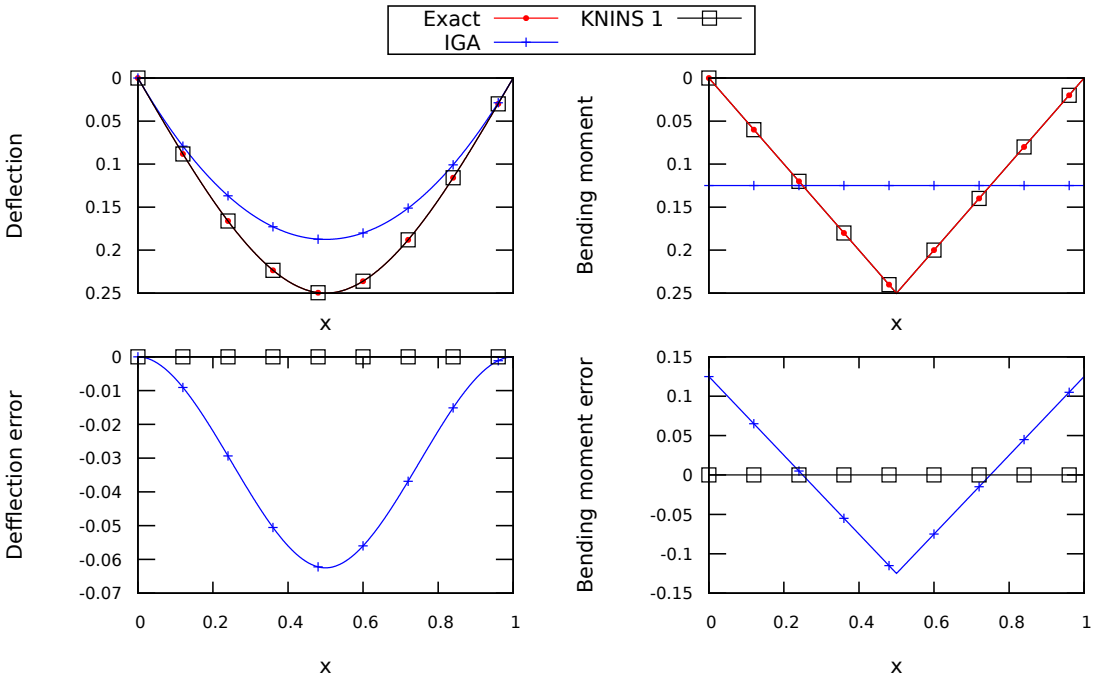

Figure 4.5.: Force load for Example 1 with numerical solution and error over the exact solution for cubic approximation over one knot span (IGA) and cubic approximation over two knot spans with a knot inserted at the location of the concentrated load (KNINS 1).

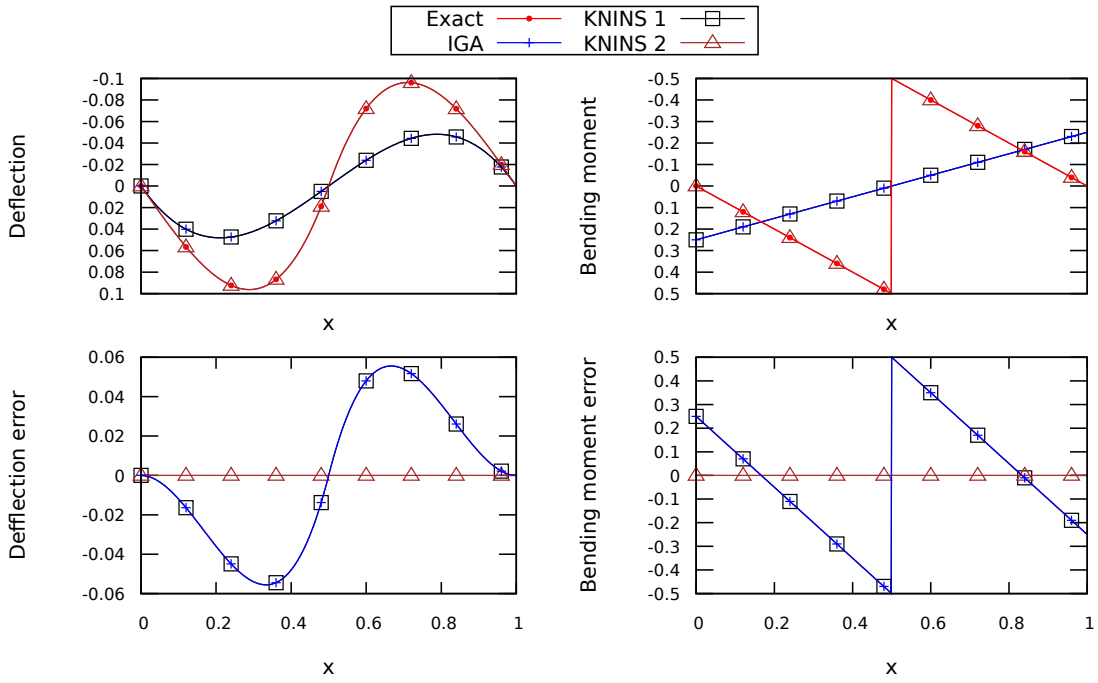

Figure 4.6.: Moment load for Example 1 with numerical solution and error with respect to the exact solution for cubic approximation over one knot span (IGA), cubic approximation over two knot spans with a knot inserted at the location of the concentrated load (KNINS 1), and cubic approximation over two knot spans with a double knot inserted at the location of the concentrated load (KNINS 2).

enforced with a single knot insertion. For the case of moment loading, a strong (C^{-1}) discontinuity in bending moment occurs at the concentrated moment location, thus C^1-continuous deflection approximation is needed. While a single knot insertion is insufficient, increasing the knot multiplicity to $m = 2$ results in the desired C^1 continuity (Figure 4.4). It is shown in Figures 4.5 and 4.6 that the numerical results for both load cases match the exact solutions when the appropriate continuity is enforced.

Note that the position of the newly inserted knot ξ_c in the parametric space must be calculated according to the parametrization. For the linear parametrization used here, parametric coordinate ξ_c is simply given as $\xi_c = J^{-1}x_c$, where x_c is the Cartesian coordinate of the discontinuity location. In general, however, the parametric coordinate ξ_c needs to be calculated from the parametrization $x_c = \sum R_i(\xi_c)x_i$, leading to a scalar nonlinear equation for an unknown ξ_c, which can be solved with the Newton-Raphson method, for example.

The analogical method can be applied to support the case of concentrated force load in a normal direction for straight beams. Additional challenges arise for curved Bernoulli beams with coupled bending and membrane actions, where G^1 continuity (weaker than C^1 continuity) is required to capture jumps in axial strain [29]. A possible solution can be based on approach presented in [29]. However, this approach

lacks an advantage of a single patch model, which can be convenient for example in case of moving load. A novel method proposed to capture jumps in all the strain components is presented in the forthcoming section.

4.1.2. Extended basis

An alternative approach supporting concentrated load is to extend the initial basis by introducing additional problem-specific interpolation functions that allow to capture the discontinuous character of the solution under concentrated forces/moments. This idea was inspired by the extended finite element method (XFEM) [64, 65], which has been already successfully combined with isogeometric analysis in more dimensions, e.g. for the use in fracture mechanics [66]. While XFEM is based on the partition of unity method [67], in the presented strategy, the global functions defined on an entire patch are used. This choice provides the exact description of the solution over an entire domain with no blending at the enrichment boundaries [68]. The computational cost is not excessively high because a patch with a reasonable number of knot spans is considered.

The proposed procedure is to tailor new basis functions based on the knowledge of the discontinuities in the bending moment and normal force caused by the concentrated loads. For each concentrated load c, definition of the additional basis function R_c^* starts with the calculation of the deflection $\bar{v}_c(x)$, which corresponds to the expected bending moment function $\bar{M}_c(x)$ under the unit load. It follows from (3.54) that the deflection can be obtained from the bending moment as

$$\bar{v}_c(x) \quad = \quad \iint -\frac{1}{EI}\bar{M}_c(x)\, dx^2. \tag{4.1}$$

The basis function $R_c^*(x)$ is chosen as the scaled deflection $\bar{v}_c(x)$

$$R_c^*(x) \quad = \quad \frac{\bar{v}_c(x)}{|\bar{v}_c(x)|_{MAX}}, \tag{4.2}$$

where $|\cdot|_{MAX}$ is the maximum of the absolute value of the function. The resulting approximation is obtained by combining the initial B-spline basis functions and the newly derived functions formally expressed in terms of ξ using the mapping between parametric and physical spaces

$$v(\xi) \quad = \quad \sum_{i=1}^{n} R_i(\xi) v_i + \sum_{c=1}^{n_c} R_c^*(x(\xi)) v_c^*, \tag{4.3}$$

where n_c is the number of concentrated loads (additional basis functions).

Coming back to the example of the simply supported beam, the exact bending moment function due to the unit force (Figure 4.7) is given as

$$\bar{M}_c \quad = \quad \begin{cases} x(\xi)\left(1 - \dfrac{x_c}{l}\right) & \text{for } \xi \in \langle 0, \xi_c \rangle\,, \\ \dfrac{(l - x(\xi))x_c}{l} & \text{for } \xi \in \langle \xi_c, 1 \rangle\,, \end{cases} \tag{4.4}$$

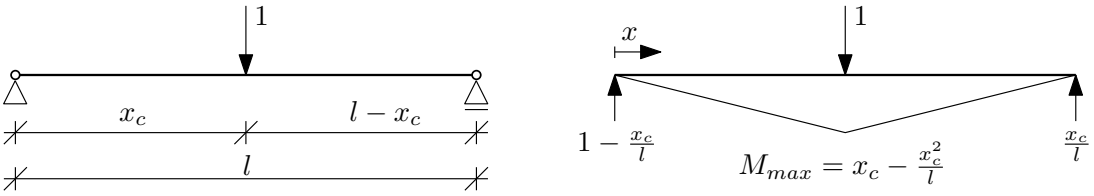

Figure 4.7.: Simply supported beam subjected to the unit force and corresponding bending moment.

where x_c is the position of the unit force and ξ_c is the associated coordinate in parametric space as discussed in Section 4.1.1. Combining equations (4.1), (4.2), and (4.4), the additional basis function R_F^* can be derived. To determine integration constants in (4.1), the boundary conditions of the simply-supported beam are used. This choice does not violate the interpolatory nature of the basis functions at the endpoints of the patch, thus the kinematic boundary conditions can still be easily prescribed at these points. Nevertheless, the new basis function has to be considered when the constraints are enforced by means of Lagrange multipliers discussed in Section 2.3.5. The analogical procedure can be used to derive the additional basis function R_M^* for the case of the concentrated moment load.

Resulting sets of basis functions for both (force and moment) load cases are illustrated in Figure 4.8. The discontinuous character of the basis functions must be taken into account during the numerical integration by splitting the affected knot span into two separate integration domains divided by the discontinuity location. With these extensions, the numerical solutions match the exact solutions, which can be observed in Figures 4.9 and 4.10.

Note that the derived enrichment will also work for beams subjected to different boundary conditions than the ones used for its derivation. This is due to the fact that different boundary conditions can be fully described by standard basis functions and a complete solution can be obtained by superposition. The same enrichment can also be used for the case of distorted mesh configurations (i.e. a non-constant mapping between x and ξ coordinates). It is convenient to derive the additional function R_F^* in the physical space to make the formulation independent of the mesh configuration. The mapping between the parametric and the physical space needs to be utilized only when the function is evaluated.

The proposed method can be easily implemented into an existing IGA code. It is necessary to extend the set of degrees of freedom and properly define the additional basis functions. Note that the use of the discontinuous additional functions requires modifying the numerical integration. The knot span where the discontinuity is located must be divided into two integration elements, so the discontinuity can be properly taken into account during numerical quadrature.

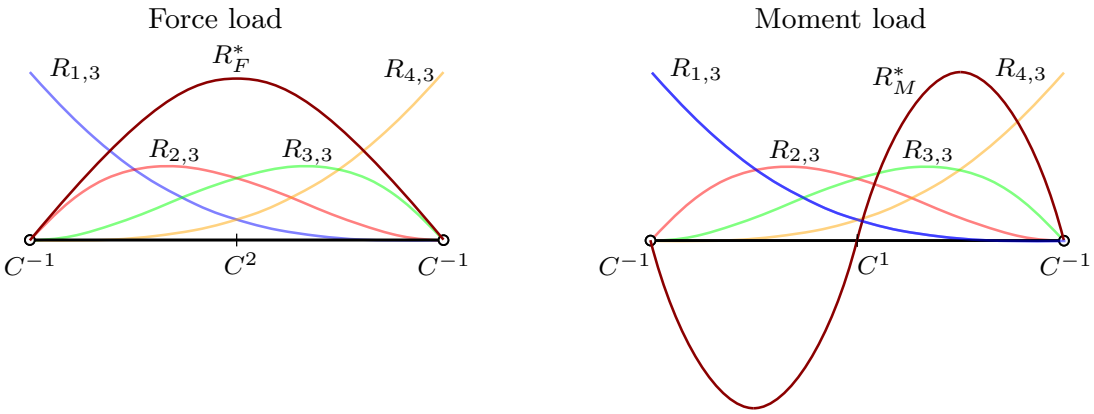

Figure 4.8.: Extended basis functions for cases of concentrated force load (left) and concentrated moment load (right) located at $\xi = 0.5$.

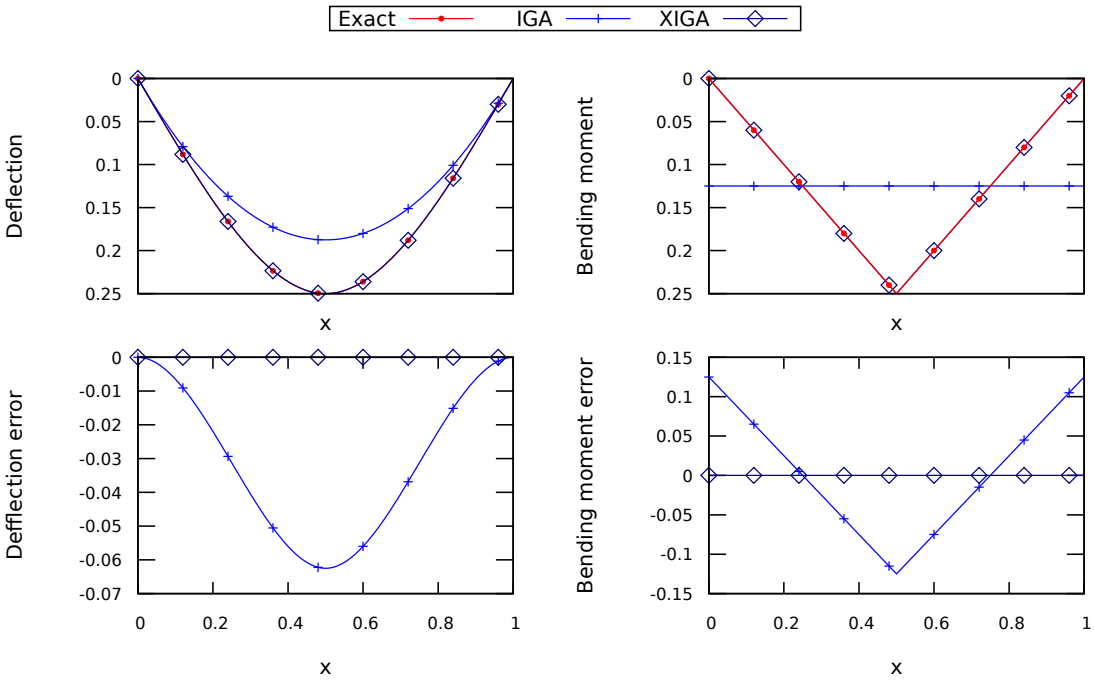

Figure 4.9.: Force load for Example 1 with numerical solution and error with respect to the exact solution for cubic approximation over one knot span (IGA) and the same approximation with basis extension (XIGA).

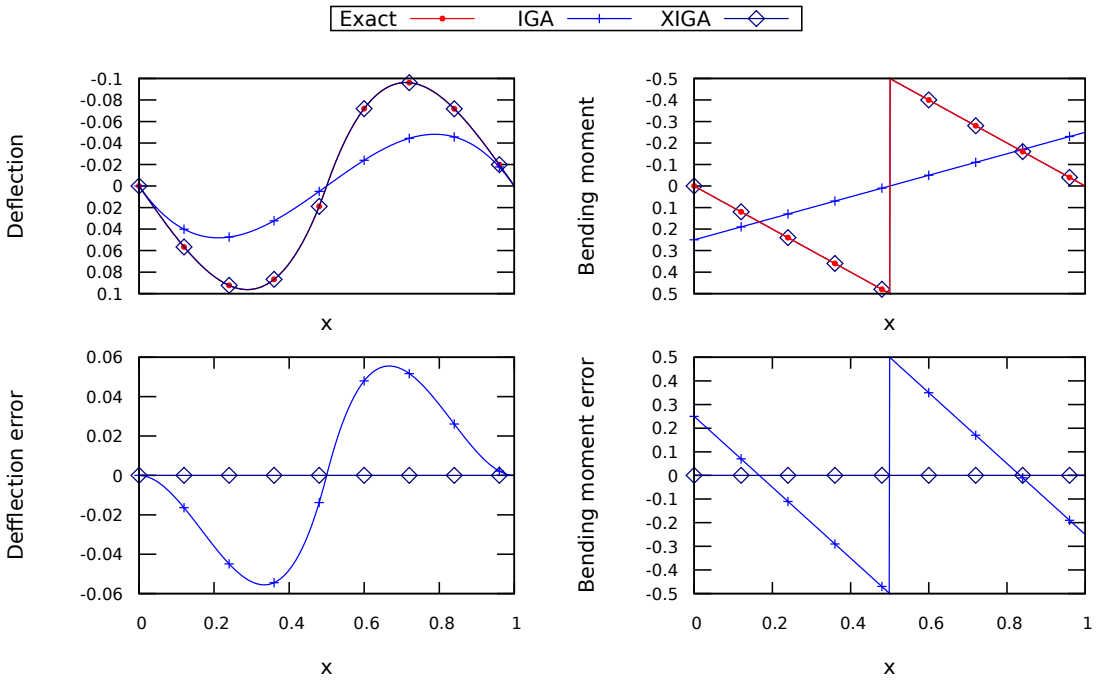

Figure 4.10.: Moment load for Example 1 with numerical solution and error with respect to the exact solution for cubic approximation over one knot span (IGA) and the same approximation with basis extension (XIGA).

4.1.3. Numerical example

To verify the performance of the presented methods, a more complex problem (Figure 4.11) has been assessed. The initial geometry is approximated using a single patch with one knot span. Since the beam is subjected to unit continuous loading, quartic approximation is used to enable an exact description of the solution.

The beam is additionally subjected to a unit concentrated moment load, thus one of the presented methods needs to be applied at that particular point. Moreover, special treatment is also required at the position of the sliding joint support because the enforcement of the constraint leads to the introduction of concentrated force load.

Knot insertion and multiplication

Due to the use of quartic approximation ($p = 4$), the continuity in a single knot is C^3. Knot multiplicity has to be increased to $m = 2$ and $m = 3$ to achieve C^2 and C^1 continuity at the location of concentrated force and moment, respectively. Thus a knot with multiplicity $m = 3$ needs to be inserted at the position of concentrated moment load and, at the position of the joint support, a knot with multiplicity $m = 2$ is required.

The resulting basis functions are illustrated in Figure 4.12 on the left. The changes lead to an increase in the number of control points from $n = 5$ to $n = 10$ and the single knot span is transformed by knot insertion into three knot spans. The use of the

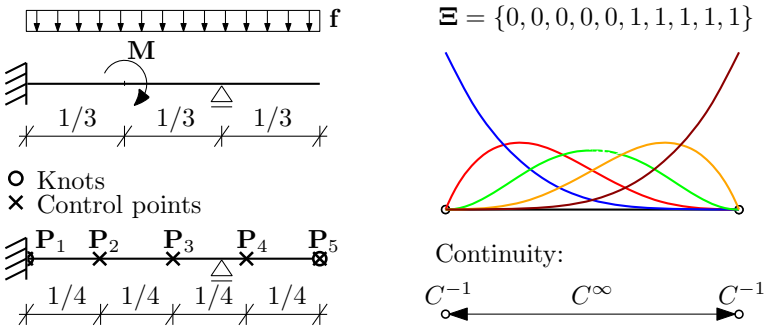

Figure 4.11.: Cantilever beam for Example 2 with intermediate sliding joint support subjected to the concentrated moment and continuous force load. The beam is approximated over one knot span using quartic B-spline basis functions.

modified basis functions leads to the following vector of unknown displacements

$$\mathbf{r}_v = \begin{matrix}[0.0000, 0.0000, -0.0108, -0.0066, 0.0961,\\ 0.0833, -0.0062, -0.0710, -0.1034, -0.1358]\end{matrix}^T, \tag{4.5}$$

which correspond to the exact solution, see Figure 4.13. The comparison to the quartic approximation over one or ten knot spans is also provided.

Extended basis

To sufficiently enrich the initial basis, two extra basis functions have been added. The functions derived in the previous section have been used, both differing from the functions in the first problem only in the position x_c. Function R_M^* provides C^1 continuity under the moment loading ($x_c = 1/3$); function R_F^* brings C^2 continuity at the position of the joint support ($x_c = 2/3$). The resulting set of basis functions are depicted in Figure 4.12 on the right.

This method keeps the initial configuration of five control points. There are two additional degrees of freedom corresponding to the coefficients of the added basis functions. The resulting vector of unknown displacements $\mathbf{r}_v$ and the vector of coefficients $\mathbf{r}_c$ for the basis functions R_M^*, R_F^* is as follows

$$\mathbf{r}_v = [0.0000, 0.6883, 0.6127, 0.0718, -0.1358], \tag{4.6}$$

$$\mathbf{r}_c = [2.6667, 6.3889]. \tag{4.7}$$

This solution again corresponds to the exact results (Figure 4.13).

4.1.4. Concluding remarks

Two different methods for overcoming the inability of B-spline basis functions to provide an exact representation of concentrated loading were presented here. Both approaches successfully introduced required discontinuities in the numerical solutions.

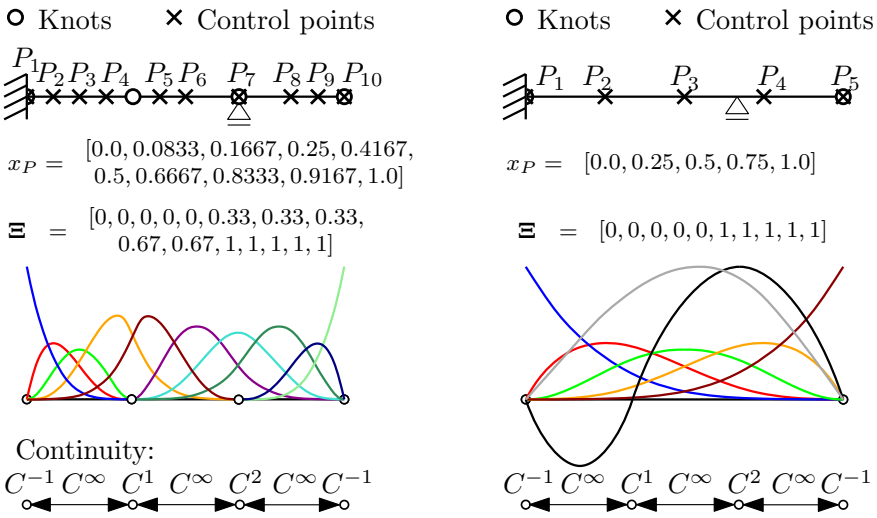

Figure 4.12.: Basis functions for Example 2 altered by knot insertion/multiplication obtained by placing a triple knot under the moment load and a double knot at the sliding joint position (left) and extended with newly-tailored functions (right).

Only a straight Bernoulli beam model was used to illustrate both approaches for clarity.

The use of knot insertion and multiplication could be seen as a more straightforward approach, especially for the automatic embedding within a CAD environment. This approach, regarding Bernoulli beams generally applicable only to straight beams with decoupled membrane and bending effects, uses standard algorithms to alter the initial B-spline basis functions leading to the introduction of the discontinuities in the numerical solution. In this approach, a strictly NURBS-based model was employed, thus all the main ideas of isogeometric analysis were preserved.

However, for some more complex settings, the proposed extension with specially-tailored basis functions seems to be much more convenient. While this approach introduces just one additional unknown per discontinuity (independently of the initial approximation), the method of knot insertion/multiplication depends on the approximation order: the higher the order, the higher the required knot multiplicity. Thus, the process can significantly increase the computational cost (especially for multiple concentrated loadings along a beam) because knot insertion and multiplication lead to more control points and related unknowns.

For some engineering problems, concentrated load can change position over time, e.g. when modeling a bridge subjected to a moving load. For a strategy based on knot insertion and multiplication, it seems inconvenient to recalculate the basis functions and control points for each time step since the position of the newly-inserted knot, which provides the required discontinuity, changes. For an extended basis, the additional basis function can be easily updated, only requiring a changing coordinate for the discontinuity. Extended basis seems to be more convenient also in case of analysis with several load cases, for the possibility to keep a single parametrization.

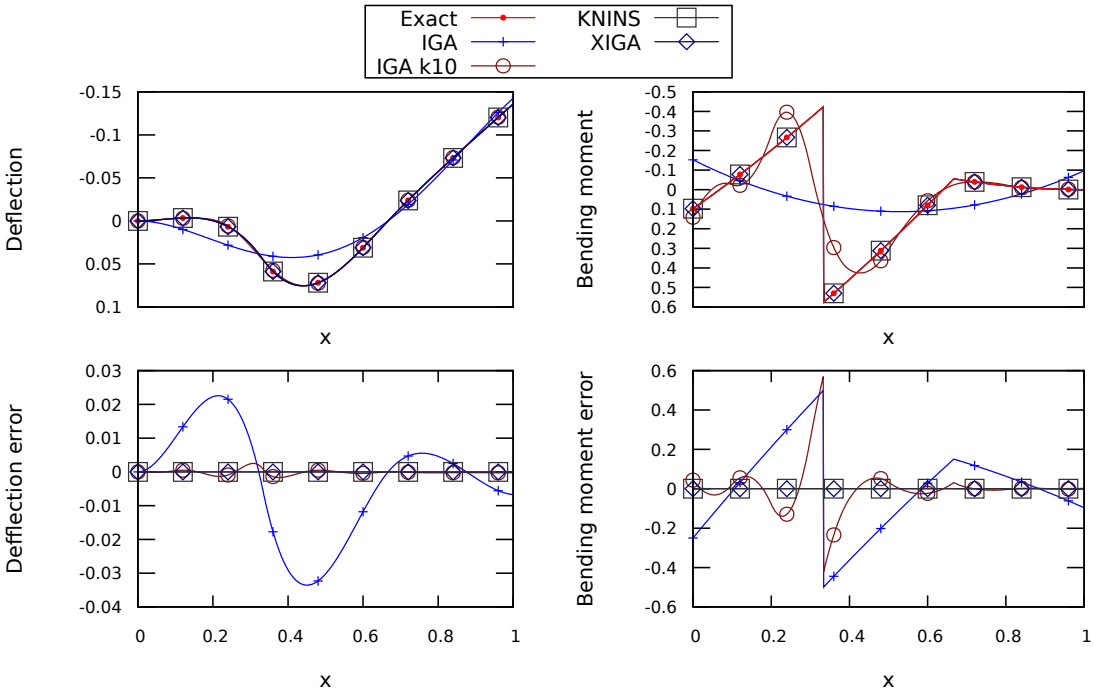

Figure 4.13.: Numerical solution and error with respect to the exact solution for Example 2 for quartic approximation over one or ten knot spans (IGA or IGA k10, respectively), quartic approximation over one knot span with the appropriate basis extension (XIGA) and quartic approximation over three knot spans with a double knot inserted at the position of sliding joint and triple knot inserted under the concentrated moment load (KNINS).

4.2. Two-dimensional curved Timoshenko beam

Following chapter is based on the author's original work [69]. For curved Timoshenko beam formulations, the problem with concentrated loadings can be avoided using a knot insertion and multiplication by enforcing C^0 continuity. This approach uses standard algorithms for handling NURBS resulting in different parametrization for various load cases, however. In many cases it is beneficial to use a single parametrization regardless of the applied load. This includes analyses with several load cases or with moving loads, where single parametrization can significantly simplify post-processing, for example. Here, the main focus is on adjusting the method of basis extension introduced in the previous section to the analysis of curved Timoshenko beams.

As proposed in the previous section, the resulting approximation is a combination of the initial NURBS basis functions and the newly-derived functions. For example for tangential displacement the approximation is designed as

$$u_t(\xi) \quad = \quad \sum_{i=1}^{n} R_i(\xi) u_t + \sum_{j=1}^{n^*_{u_t}} R^*_{u_t}(s(\xi)) u^*_{t,j}, \tag{4.8}$$

where $n^*_{u_t}$ is the number of additional basis functions $R^*_{u_t}(s(\xi))$ and $u^*_{t,j}$ are corresponding degrees of freedom. While the additional functions designed for straight Bernoulli beam enable to provide the exact solution, this goal is more complicated to be achieved in case of curved beam due to the coupling of the axial, shear and bending effects. The extension functions designed in the forthcoming text intentionally do not depend on particular geometry, which causes the exact solution is not obtained, however, the adaptive basis enrichment can reduce the error very efficiently. Additionally, once derived, the extension functions can be applied to the arbitrarily-curved beams.

The derivation of the additional functions starts from equilibrium equations by observation of discontinuities in the internal forces caused by the concentrated loading, see 4.2.1. Consequently, geometrical relations are used to identify the character of discontinuities in the displacements and rotation. Finally, the additional basis functions extending displacement and rotation approximations to capture the observed discontinuities in internal forces are designed. Three load cases are studied: tangential (longitudinal) force load F_t, perpendicular (transverse) force load F_n, and moment load M_l. All other concentrated loads can be obtained by means of a superposition. Although only a two-dimensional curved beam is considered here, the extension of this method to a three-dimensional curved beam is straightforward.

4.2.1. Identification of the discontinuities

The derivation starts from equilibrium equations on differetial element (see Fig 4.14)

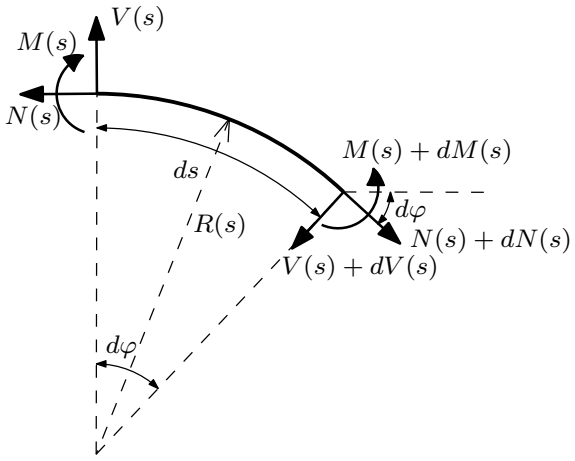

Figure 4.14.: Internal forces acting on differential element of an arbitrarily-curved beam.

$$
\begin{aligned}
-N(s) + (N(s) + dN(s))cos(d\varphi) - (V(s) + dV(s))sin(d\varphi) &= 0, && (4.9)\\
-V(s) + (V(s) + dV(s))cos(d\varphi) + (N(s) + dN(s))sin(d\varphi) &= 0, && (4.10)\\
-M(s) + (M(s) + dM(s)) - (N(s) + dN(s))R(s)(1 - cos(d\varphi)) & \\
-(V(s) + dV(s))R(s)sin(d\varphi) &= 0. && (4.11)
\end{aligned}
$$

Considering a small values of angle $d\varphi$ the following assumptions apply

$$
\begin{aligned}
cos(d\varphi) &\rightarrow 1, && (4.12)\\
sin(d\varphi) &\rightarrow d\varphi, && (4.13)\\
d\varphi &= \frac{ds}{R(s)}, && (4.14)
\end{aligned}
$$

where R is the radius of curvature. Substituting (4.12-4.14) into equilibrium equations (4.9-4.11) yields

$$
\begin{aligned}
dN(s) - (V(s) + dV(s))\frac{ds}{R(s)} &= 0, && (4.15)\\
dV(s) + (N(s) + dN(s))\frac{ds}{R(s)} &= 0, && (4.16)\\
dM(s) - (V(s) + dV(s))ds &= 0. && (4.17)
\end{aligned}
$$

By neglecting high order terms and considering a limit case $ds \rightarrow 0$, the following differential equilibrium equations are obtained

$$
\begin{aligned}
\frac{dN(s)}{ds} &= \frac{V(s)}{R(s)}, && (4.18)\\
\frac{dV(s)}{ds} &= -\frac{N(s)}{R(s)}, && (4.19)\\
\frac{dM(s)}{ds} &= V(s). && (4.20)
\end{aligned}
$$

Subsequently, by differentiating the above relations the equations for the second derivatives of internal forces are derived

$$\frac{d^2N(s)}{ds^2} = \frac{\frac{dV(s)}{ds}R(s) - V(s)\frac{dR(s)}{ds}}{R(s)^2}, \tag{4.21}$$

$$\frac{d^2V(s)}{ds^2} = -\frac{\frac{dN(s)}{ds}R(s) - N(s)\frac{dR(s)}{ds}}{R(s)^2}, \tag{4.22}$$

$$\frac{d^2M(s)}{ds^2} = \frac{dV(s)}{ds}. \tag{4.23}$$

The above equations (4.18-4.23) can be used to identify the discontinuities caused by the concentrated loading.

Tangential force load

Concentrated tangential load causes strong discontinuity (jump in a function value) in the normal force. Consequently, using the relations for the first and the second derivatives of the internal forces (4.18-4.23), the strong discontinuities can be identified in the first derivative of the shear force and the second derivatives of all internal forces. By expressing high order derivatives of internal forces it can be shown, that the strong discontinuities re-occur in all subsequent derivatives of all internal forces.

The corresponding discontinuities in the displacements and rotation are determined using a combination of geometrical and constitutive relations (3.20, 3.15). From (3.20, 3.15) it follows that the strong discontinuity in the second derivative of the bending moment implies a strong discontinuity in the third derivative of the rotation φ. The strong discontinuity in the normal force together with the continuous normal displacement u_n imply a jump in the first derivative of tangential displacement u_t. Discontinuity in the first derivative of shear force together with the continuous rotation derivative φ' and with consideration of the general material parameters also imply a jump in the second derivative of normal displacement u_n.

Following previous considerations, discontinuities in the high order derivatives can be determined. In sum, strong discontinuity is observed in the first, third and each higher derivative of the tangential displacement, in the second and higher derivatives of the normal displacement and in the third and higher derivatives of the rotation.

Perpendicular force load

Concentrated perpendicular load causes strong discontinuity in the shear force. Analogically to the tangential force load, the strong discontinuities can be subsequently identified in the first derivatives of the normal force and the bending moment, and the second derivatives of the normal and shear forces. Similarly to the case of tangential load F_t strong discontinuities re-occur again in third and all subsequent derivatives of all internal forces.

Assuming geometrical and constitutive equations (3.20, 3.15) the strong discontinuity in the first derivative of the bending moment implies a strong discontinuity in

	Internal forces			Unknowns		
	N	V	M	u_t	u_n	φ
F_t	0, 2, 3+	1, 2, 3+	2, 3, 4+	1, 3, 4+	2, 3, 4+	3, 4, 5+
F_n	1, 2, 3+	0, 2, 3+	1, 3, 4+	2, 3, 4+	1, 3, 4+	2, 4, 5+
M_l	-	-	0	3, 5, 7, ...	2, 4, 6, ...	1

Table 4.1.: Orders of strongly discontinuous derivatives in internal forces and unknown displacements and rotation.

the second derivative of the rotation φ. The strong discontinuity in the shear force together with the continuous tangential displacement u_t and rotation φ imply a jump in the first derivative of normal displacement u_n. Discontinuity in the first derivative of normal force together with consideration of the general material parameters also imply a jump in the second derivative of tangential displacement u_t.

Similarly to the case of tangential force load, discontinuities in the high order derivatives can be determined. In sum, strong discontinuity is observed in the second and every higher derivative of the tangential displacement, in the first, the third and every higher derivative of the normal displacement, and in the second, the fourth and every higher derivative of the rotation.

Moment load

Concentrated moment load causes strong discontinuity in the bending moment. This discontinuity does not propagate to other internal forces or their derivatives. According to geometrical and constitutive equations (3.20, 3.15) the strong discontinuity in the the bending moment implies a strong discontinuity in the first derivative of the rotation φ. Moreover, the strong discontinuity in the first derivative of the rotation φ together with the continuous normal force, normal displacement, and the first derivative of shear force imply a jump in the second derivative of normal displacement u_n. Consequently, discontinuity in the second derivative of normal displacement u_n together with continuous second derivative of normal force imply the strong discontinuity in the third derivative of the tangential displacement u_t. Following these considerations, the recurring occurrence of the strong discontinuities can be observed in each even derivative of the normal displacement u_n and in the third and higher odd derivatives of the tangential displacement u_t.

Table 4.1 summarizes the derivatives for which strong discontinuity is present in all three load cases.

4.2.2. Design of the extension function

Knowledge of the discontinuity patterns in displacements and rotation is essential for the design of additional basis functions extending displacement approximation. The proposed method introduces a sequence of extension functions for each discontinuity.

There are countless ways designing additional basis functions. In the present study, the functions were designed to be independent of the geometry of the problem. The only variable in the derived function is the force/moment location. This way, the derived functions can be reused for different geometries. The individual enrichment functions are derived by integrating the piecewise constant function with the jump at the force/ moment location.

Consider, for example, the discontinuity in the first derivative of the displacement (rotation). The enrichment function R^* is derived starting from the first derivative

$$R^{*\prime} = \begin{cases} a & \text{for } s \in \langle 0, s_F \rangle, \\ b & \text{for } s \in (s_F, L\rangle, \end{cases} \tag{4.24}$$

where $a \neq b$ are optional constants and s_F is the s-coordinate of the discontinuity. By integrating (4.24) the basis function R^* is derived as

$$R^* = \begin{cases} as + C_1 & \text{for } s \in \langle 0, s_F \rangle, \\ bs + C_2 & \text{for } s \in (s_F, L\rangle. \end{cases} \tag{4.25}$$

The constant a is chosen arbitrarily, while the requirement of $R^*(0) = R^*(L) = 0$ and the requirement of continuous displacement (rotation) at the force location are used to determine integration constants C_1 and C_2 and constant b. This choice does not violate the interpolatory nature of the basis functions at the endpoints of the patch; thus, the kinematic boundary conditions can still be easily prescribed at these points. An analogous procedure can be performed for the derivation of the basis function introducing the discontinuity into the high order derivatives.

It is obvious from the previous derivations, that several additional basis functions must be added in order to support a single concentrated load, see Table 4.1. The presented method proposes adding discontinuity enrichment functions in sets containing a single function for each degree of freedom (u_t, u_n, φ) starting from the low order derivatives. For example the first set for the tangential force load F_t contains functions with the discontinuity in the first derivative of tangential displacement u_t, the second derivative of normal displacement u_n, and the third derivative of the rotation φ. Table 4.2 summarizes the first and the second sets. See Appendix A for all fully-derived extension functions.

4.2.3. Numerical examples

To verify the performance of the presented method, three benchmark problems were considered. (1) A simply-supported circular beam problem was studied in detail, also with the aim of examining locking issues, (2) a parabolic beam, and (3) an s-shaped beam, were also analyzed in order to evaluate the performance of the method for cases with non-constant curvature and different boundary conditions. Performance was evaluated using relative L^2-error norm of resulting internal forces

$$||e||_{L^2,rel} = \frac{||(\cdot)^{ex} - (\cdot)^h||_{L^2}}{||(\cdot)^{ex}||_{L^2}}. \tag{4.26}$$

		u_t	u_n	φ
F_t	Set 1	1	2	3
	Set 2	3	3	4
F_n	Set 1	2	1	2
	Set 2	3	3	4
M_l	Set 1	3	2	1
	Set 2	5	4	-

Table 4.2.: Definition of sets of additional functions for each unknown displacement or rotation depending on the type of applied concentrated load. Numbers determine the order of the discontinuous derivative of the additional function.

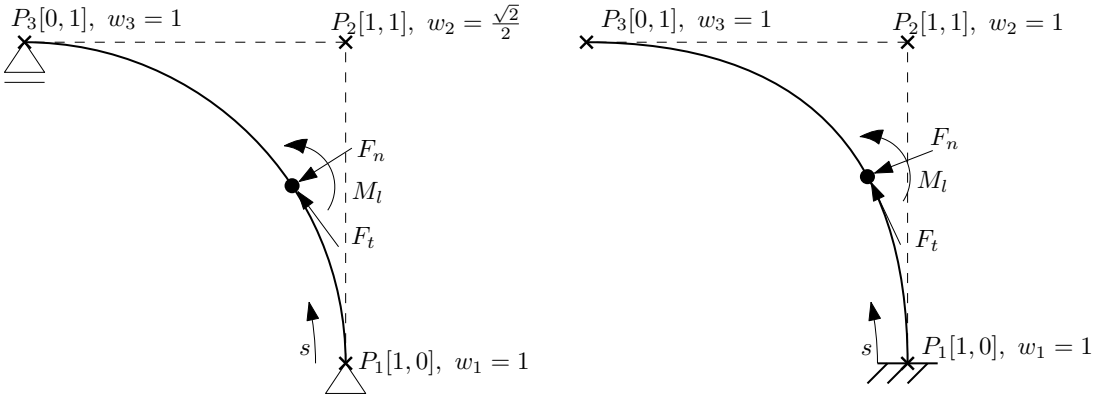

a) Circular beam b) Parabolic beam

Figure 4.15.: Geometry of a) the circular beam and b) the parabolic beam.

L^2-norms were calculated using numerical integration. Exact solutions of internal forces were calculated using equilibrium equations pointwise at each integration point. For statically indeterminate problems (s-shaped beam) the reactions were calculated using the force method. NURBS parametrization was used to obtain tangent and normal vectors necessary for the transformation. The same sets of enrichment functions have been used in all the examples.

4.2.4. Simply-supported circular beam

The geometry of the circular beam problem is depicted in Figure 4.15a. The initial geometry was parametrized using quadratic NURBS and three control points $P_1 = [1,0]$, $P_2 = [1,1]$, $P_3 = [0,1]$ with weights $w_1 = 1$, $w_2 = \frac{\sqrt{2}}{2}$, $w_3 = 1$. The finer meshes were obtained using *k*-refinement (degree elevation and subsequent knot insertion). The analysis was performed for the three concentrated load types: unit tangential force F_t, unit perpendicular force F_n, and unit moment M_l. The chosen position of the load was $s_F = 0.33$.

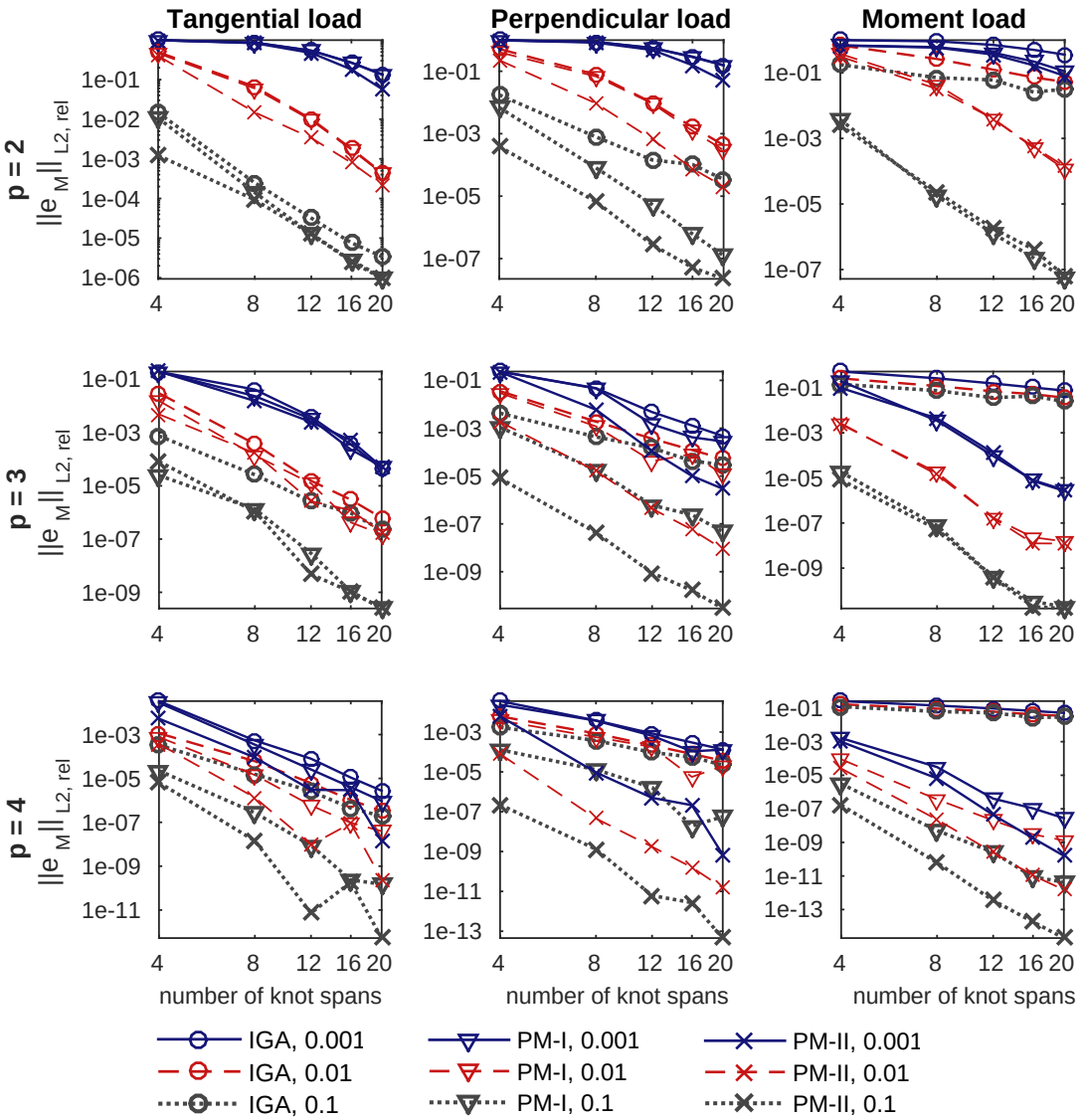

Figure 4.16.: Simply-supported circular beam: Convergence of moment field for 2^{nd}, 3^{rd}, and 4^{th} degree NURBS basis. Three thickness to length ratios are used: $h/L = 0.001$, $h/L = 0.01$, and $h/L = 0.1$. For thin beams, numerical locking is observed for standard IGA as well as for IGA enhanced by one (PM-I) or two (PM-II) sets of additional functions when low order approximation is used.

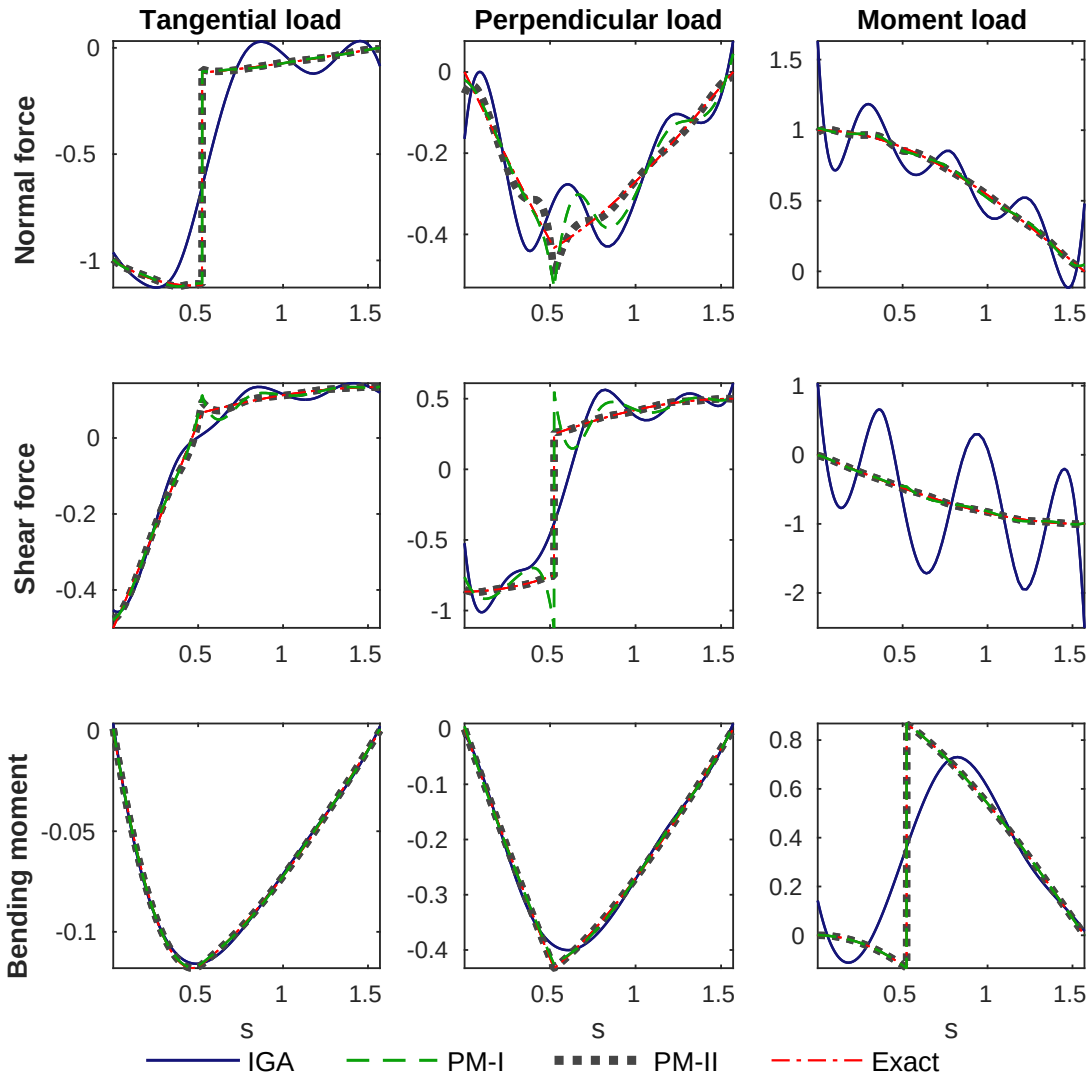

Figure 4.17.: Simply-supported circular beam: Profiles of internal forces along the length of the beam for standard 4^{th}-degree NURBS over 4 knot spans (IGA) and the same approximation extended by one (PM-I) or two (PM-II) sets of additional basis functions compared to the exact solution.

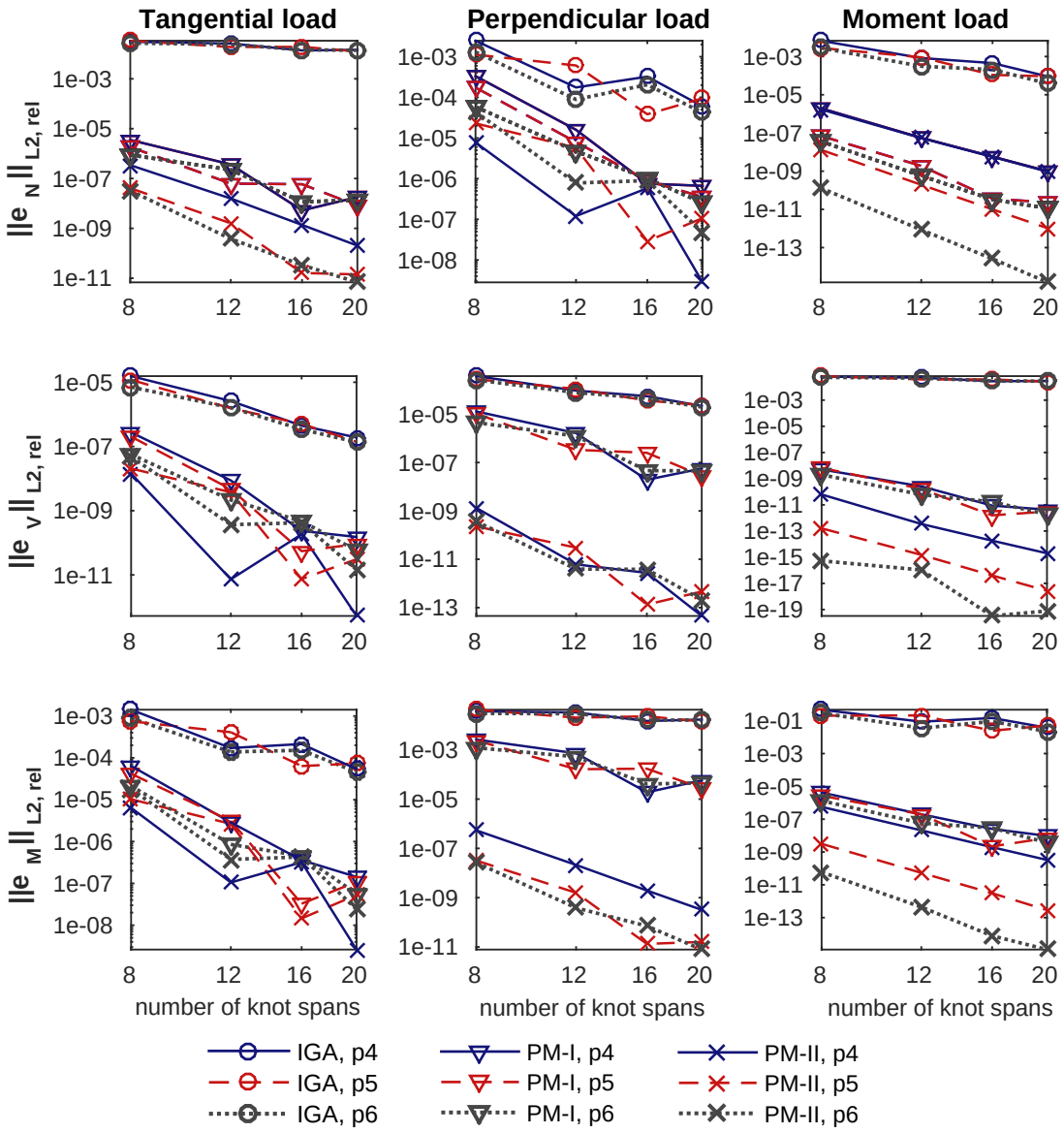

Figure 4.18.: Simply-supported circular beam: Relative L^2-error norms of internal forces for 4^{th}, 5^{th}, and 6^{th} degree NURBS basis. Superior performance of IGA enhanced by one (PM-I) or two (PM-II) sets of additional functions over standard IGA is demonstrated.

	Relative L^2-error norm of internal forces				% improvement		
Load		IGA	PM-I	PM-II		PM-I	PM-II
F_t	$\|\|e_N\|\|$	5.15e-02	2.35e-05	2.96e-05	I_N	99.9	99.9
	$\|\|e_V\|\|$	1.64e-02	3.78e-03	1.40e-03	I_V	76.9	91.4
	$\|\|e_M\|\|$	3.29e-04	2.25e-05	6.49e-07	I_M	93.1	98.0
F_n	$\|\|e_N\|\|$	7.70e-02	1.94e-02	4.31e-03	I_N	74.8	94.4
	$\|\|e_V\|\|$	7.84e-02	1.59e-02	4.40e-05	I_V	79.8	99.9
	$\|\|e_M\|\|$	1.73e-03	1.29e-04	2.55e-07	I_M	92.5	99.9
M_l	$\|\|e_N\|\|$	4.56e-02	4.49e-04	1.52e-04	I_N	99.0	99.7
	$\|\|e_V\|\|$	9.87e-02	4.73e-04	1.27e-04	I_V	99.9	99.9
	$\|\|e_M\|\|$	1.23e-01	3.08e-06	1.66e-07	I_M	99.9	99.9

Table 4.3.: Simply-supported circular beam: Relative L^2-error norms of internal forces (p=4, n=4) and percentage improvement I of the proposed method (PM-I, PM-II) over IGA.

The analysis was performed for three different thickness-length ratios in order to evaluate the effect of numerical locking. Figure 4.16 provides a plot for the relative L^2-error norm of bending moment. For the quadratic NURBS basis functions, numerical locking is observed for all three load cases. For the cubic NURBS basis functions, the locking phenomena is partially alleviated, while no locking can be observed when quartic NURBS basis functions are used. These observations correspond to Zhang et al. [12] and demonstrate that locking alleviation is not affected by introducing enrichment functions. Considering these results, only 4^{th}-order and higher basis functions were used in the subsequent examples. A single thickness-length ratio $h/L = 0.1$ was chosen for demonstrating the results.

The circular beam parameterized with quartic NURBS basis functions over four knot spans was analyzed in order to evaluate the performance of the proposed method. The internal forces obtained with standard NURBS approximation as well as the approximation enriched by one or two sets of additional basis functions are depicted in Figure 4.17, in which the superior performance of the presented method can be observed, especially when two sets of additional basis functions are used. The resulting relative L^2-error norms are summarized in Table 4.3. The percentage of improvement of the relative L^2-error norm given as $I = 1 - \dfrac{||e||^{IGA}_{L^2,rel}}{||e||^{PM}_{L^2,rel}}$ is also provided.

Finally, circular beam analysis was performed for approximation degrees $p = 4, 5, 6$ and number of knot spans $n = 8, 12, 16, 20$. The outstanding performance of approximation extended by two sets of additional basis functions over standard NURBS approximation can be observed in Figure 4.18, which plots the convergence of the relative L^2-error norm of internal forces.

	Relative L^2-error norm of internal forces				% improvement		
Load		IGA	PM-I	PM-II		PM-I	PM-II
F_t	$\|\|e_N\|\|$	3.03e-02	4.81e-06	4.04e-06	I_N	99.9	99.9
	$\|\|e_V\|\|$	2.68e-03	1.04e-04	5.04e-05	I_V	96.1	98.1
	$\|\|e_M\|\|$	5.20e-05	6.58e-07	1.53e-07	I_M	98.7	99.7
F_n	$\|\|e_N\|\|$	9.38e-03	2.37e-03	2.15e-03	I_N	74.7	77.0
	$\|\|e_V\|\|$	2.77e-02	5.57e-04	3.30e-05	I_V	98.0	99.9
	$\|\|e_M\|\|$	6.61e-04	3.27e-06	1.11e-07	I_M	99.5	99.9
M_l	$\|\|e_N\|\|$	5.65e-03	2.90e-03	2.40e-03	I_N	48.7	57.6
	$\|\|e_V\|\|$	3.50e-01	2.05e-04	1.64e-04	I_V	99.9	99.9
	$\|\|e_M\|\|$	2.93e-02	6.15e-08	4.31e-08	I_M	99.9	99.9

Table 4.4.: Parabolic cantilever beam: Internal forces relative L^2-error norms (p=4, n=8) and percentage improvement I of the proposed method (PM-I, PM-II) over IGA.

4.2.5. Cantilever parabolic beam

The initial geometry of the parabolic beam differed from the circular beam only in the weight of the second control point $w_2 = w_1 = w_3 = 1.0$, see Figure 4.15b. The beam was fixed at one of the ends. The same three concentrated loads used for the circular problem were considered at location $s_F = 0.33$.

The results for quartic approximation with 8 knot spans are shown in Figure 4.19 and tabulated in Table 4.4. Again, very good overall performance of the enhanced basis can be observed. Similarly to the circular beam, the results of the analysis using finer meshes with approximation degrees $p = 4, 5, 6$ and number of knot spans $n = 8, 12, 16, 20$ were used for the convergence study. Only the extension using two sets of additional functions was used, since the improved performance was proven in the previous example. Again, very good performance of the proposed method over standard NURBS approximation is proved, see Figure 4.20 for all the results.

4.2.6. S-shaped beam with both ends fixed

The geometry of the s-shaped beam problem fixed at both ends is depicted in Figure 4.21. The initial cubic geometry was parameterized using four nodes $P_1 = [0, 0]$, $P_2 = [1, 0]$, $P_3 = [1, 1]$, $P_4 = [2, 1]$ with weights $w_1 = w_2 = w_3 = w_4 = 1$. The finer mesh was again obtained by k-refinement. To be consistent with the previous examples, three concentrated loads at $s_F = 0.33$ were applied.

The results for quartic approximation with 8 knot spans are shown in Figure 4.22 and tabulated in Table 4.5. Very good improvement over standard IGA is shown for the most of the cases. For the moment load, a low improvement of the normal force was obtained. However, an excellent improvement was achieved for the shear force and the bending moment, where the initial error was more significant than the error

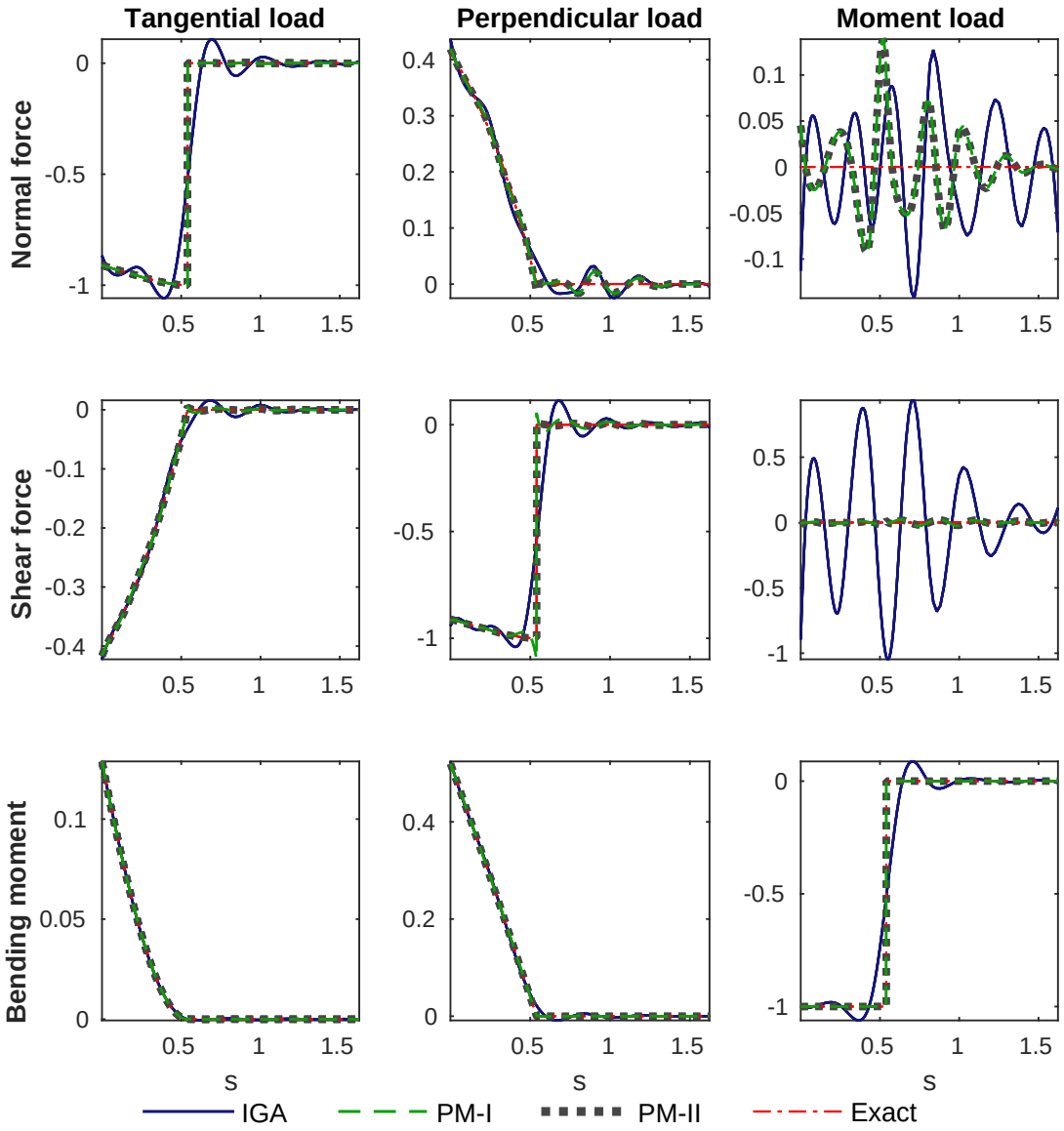

Figure 4.19.: Parabolic cantilever beam: Profiles of internal forces along the length of the beam for standard 4^{th}-order NURBS over 4 knot spans (IGA) and the same approximation extended by one (PM-I) or two (PM-II) sets of additional basis functions compared to the exact solution.

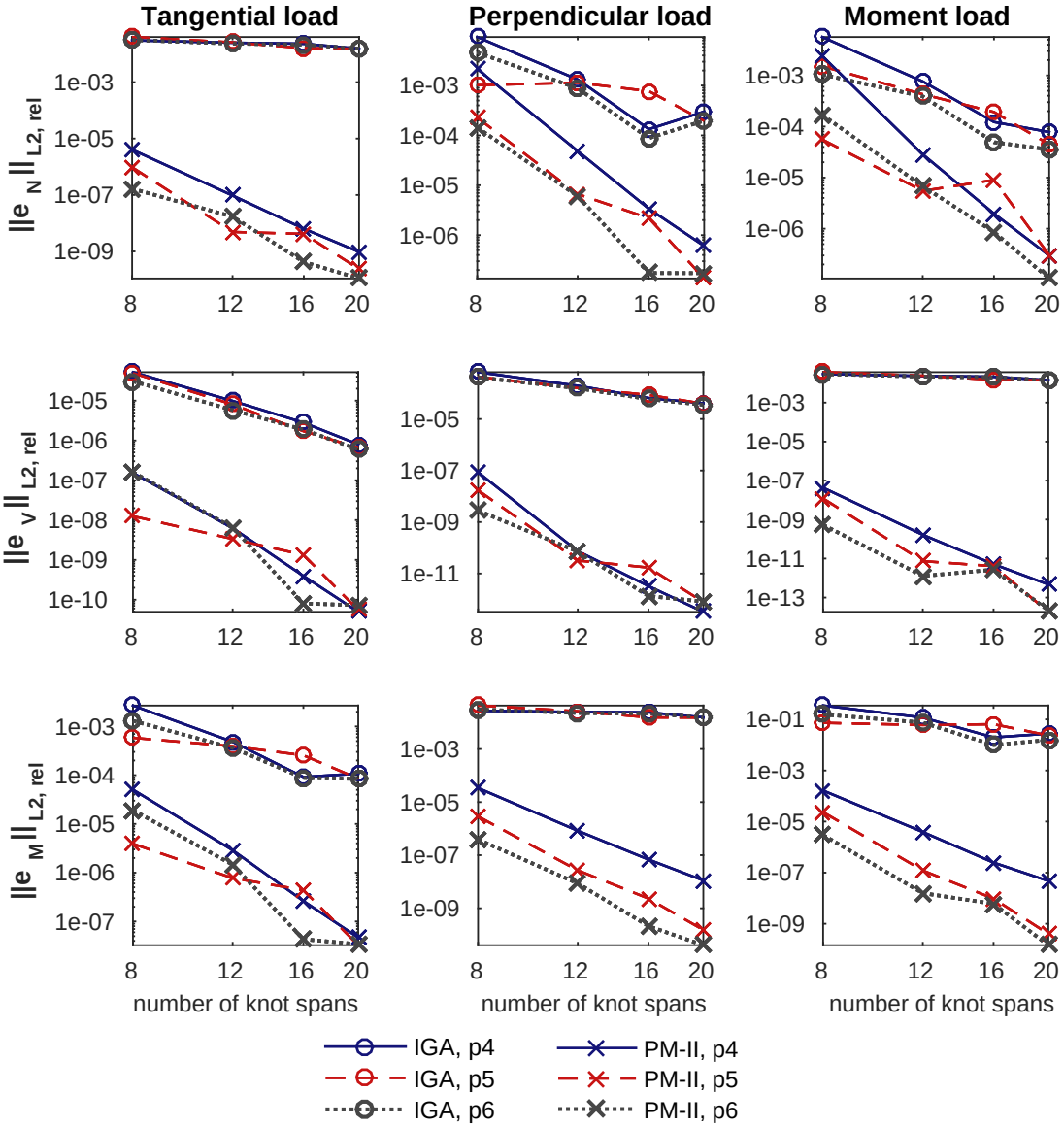

Figure 4.20.: Parabolic cantilever beam: Relative L^2-error norms of internal forces for 4^{th}, 5^{th}, and 6^{th} degree NURBS basis. Superior performance of IGA enhanced by two (PM-II) sets of additional functions over standard IGA is demonstrated.

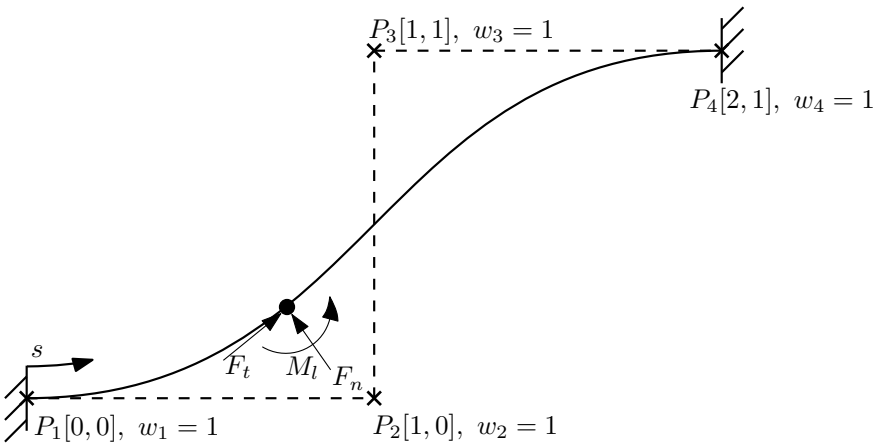

Figure 4.21.: Geometry of the s-shaped beam.

of the normal force. The results of the analysis with degrees $p = 4, 5, 6$ and number of knot spans $n = 8, 12, 16, 20$ are provided in Figure 4.23. For this problem, the superior overall performance of the proposed method was documented.

	Relative L^2-error norm of internal forces				% improvement		
Load		IGA	PM-I	PM-II		PM-I	PM-II
F_t	$\|\|e_N\|\|$	4.51e-02	8.73e-05	4.81e-05	I_N	99.8	99.9
	$\|\|e_V\|\|$	2.04e-03	2.76e-04	2.41e-04	I_V	86.5	88.1
	$\|\|e_M\|\|$	8.55e-05	4.64e-06	3.04e-06	I_M	94.6	96.4
F_n	$\|\|e_N\|\|$	1.22e-03	3.07e-04	2.67e-04	I_N	74.8	78.1
	$\|\|e_V\|\|$	4.73e-02	6.28e-04	6.24e-05	I_V	98.7	99.9
	$\|\|e_M\|\|$	2.55e-03	5.80e-06	1.30e-06	I_M	99.8	99.9
M_l	$\|\|e_N\|\|$	1.11e-02	9.99e-03	9.86e-03	I_N	9.95	11.1
	$\|\|e_V\|\|$	3.90e-01	2.41e-04	2.39e-04	I_V	99.9	99.9
	$\|\|e_M\|\|$	1.35e-01	6.49e-07	6.33e-07	I_M	99.9	99.9

Table 4.5.: S-shaped beam with both ends fixed: Internal forces relative L^2-error norms (p=4, n=8) and percentage improvement I of the proposed method (PM-I, PM-II) over IGA.

4.2.7. Concluding remarks

The original method based on approximation enrichment for overcoming the NURBS basis functions' inability to provide exact representations of concentrated loading was extended for the use in analysis of curved Timoshenko beams. Extension functions for arbitrarily-curved beams were designed, and the superior performance of the method was documented using three benchmark problems. Three load cases were studied; all

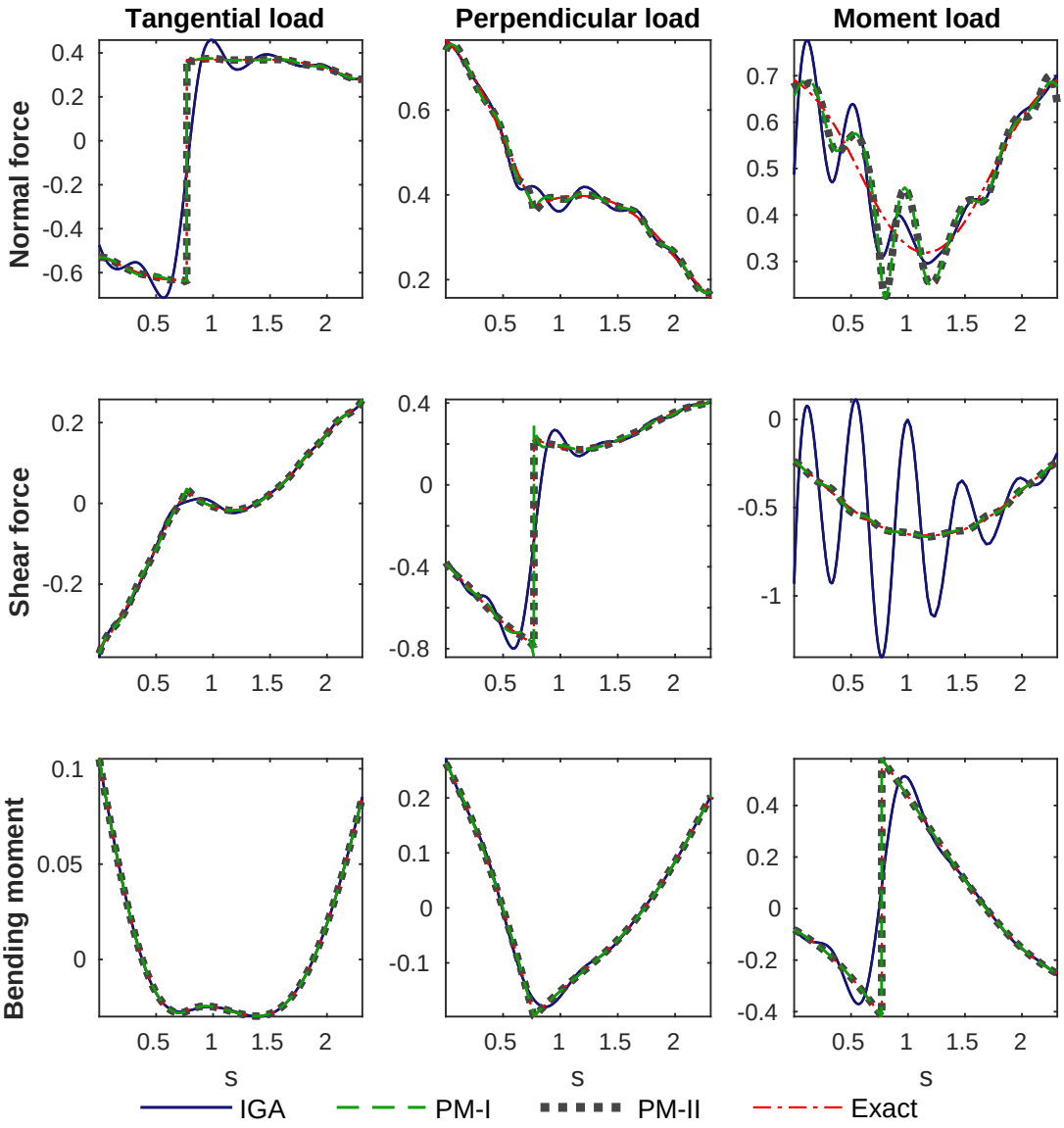

Figure 4.22.: S-shaped beam with both ends fixed: Profiles of internal forces along the length of the beam for standard 4^{th}-order NURBS over 4 knot spans (IGA) and the same approximation extended by one (PM-I) or two (PM-II) sets of additional basis functions compared to the exact solution.

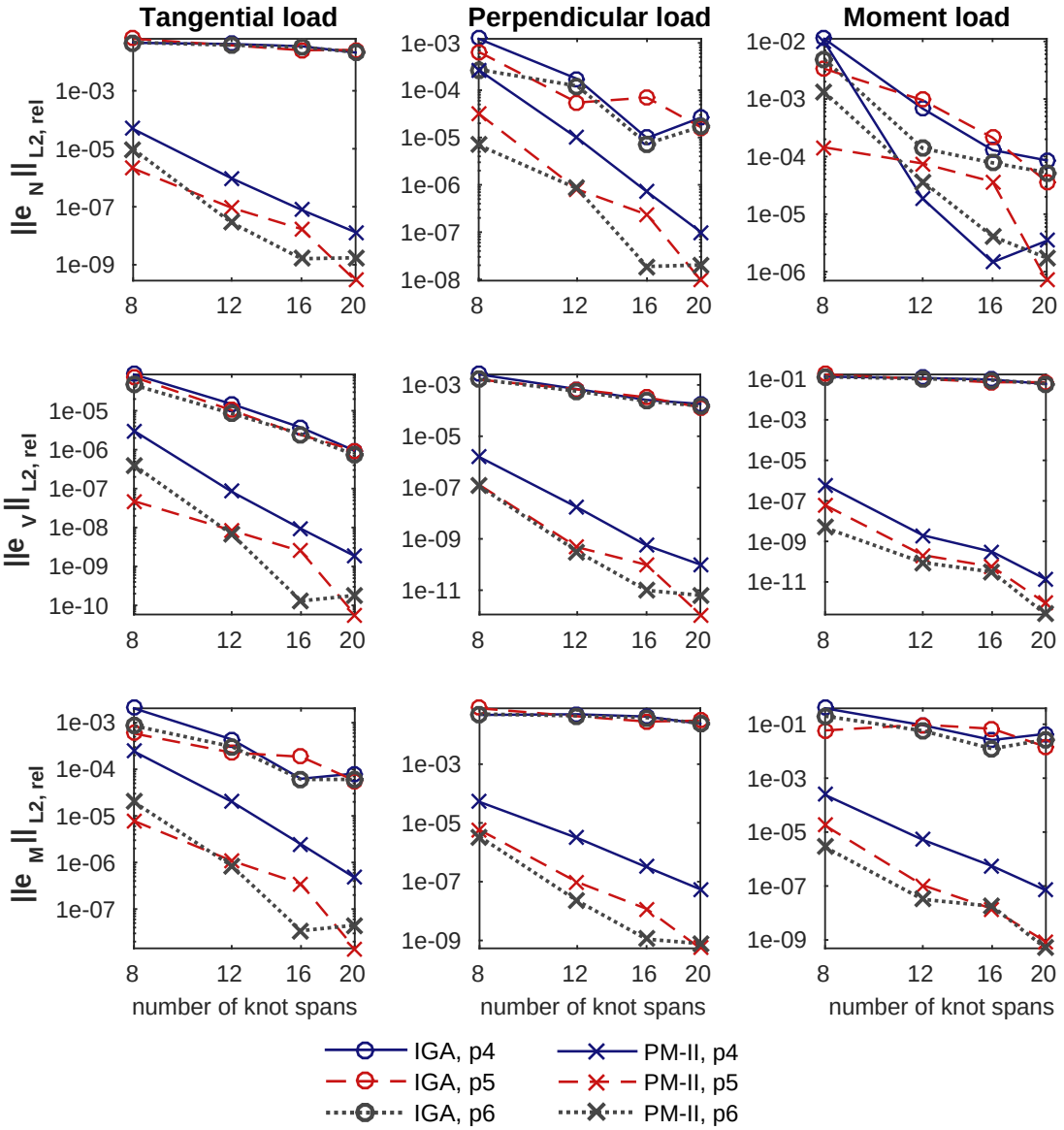

Figure 4.23.: S-shaped beam with both ends fixed: Relative L^2-error norms of internal forces for 4^{th}, 5^{th}, and 6^{th} degree NURBS basis. Superior performance of IGA enhanced by two (PM-II) sets of additional functions over standard IGA is demonstrated.

other concentrated loading (as well as the combination of concentrated and continuous loading) can be obtained by means of superposition (for linear problems).

This study of the discontinuities in the internal forces of arbitrarily-curved beam subjected to concentrated loading shows the recurring occurrence of strong discontinuities. This observation initiated the use of several extension functions to support a single discontinuity. The presented procedure suggests adding functions in sets containing an extension for each displacement and rotation, starting from the low order derivatives. The proposed additional functions were designed to depend only on concentrated load locations and not on the particular geometry of the beam. The superior performance of this method was documented when two sets of basis functions were used.

This method could be additionally improved by taking into account the geometry of the problem during the design of the additional functions, but in that case, genericity (i.e. the ability of applying the functions to various geometries) would be lost. Nevertheless, the performance of the proposed geometrically-independent enrichment is excellent and the use of proposed approach for arbitrarily-curved beams can be recommended.

CHAPTER

FIVE

CONCLUSIONS

The presented thesis focuses on the application of isogeometric analysis to arbitrarily curved beams. The main aspects of the isogeometric approach were discussed. Beam formulations based on both Timoshenko and Bernoulli beam theories were introduced and implemented.

Regarding Timoshenko beams, both two- and three-dimensional formulations with locking treatment methods were provided. Three different locking treatments were implemented and tested: reduced integration, DSG method and $\bar{\mathbf{B}}$ method. The implementation was verified and the performance of the locking removal techniques was evaluated by means of several tests. The best results in unlocking elements were achieved using a formulation with $\bar{\mathbf{B}}$ method or DSG method, which provided almost the same results. Bernoulli beam element was also implemented. Additionally, the formulation chosen for the implementation accounts also for the geometrically nonlinear analysis. The verification of the element implementation was performed using benchmarks involving both linear and nonlinear analysis.

Two platforms were used for the implementation of the elements. Matlab was used for the initial implementation and for the evaluation of the newly developed methods (two-dimensional Timoshenko beam formulations, Bernoulli beam, basis extension). All of the presented Timoshenko beam formulations were implemented in open-source finite element solver OOFEM. Along with the implementation in OOFEM, an automatic input file generator and an interactive design tool were developed. These tools ease the creation of the input file and for the two-dimensional Timoshenko beam are even able to automatically visualize the results of the analysis within a CAD environment.

Finally, the inability of NURBS basis functions to represent the discontinuities in the numerical solution when a beam is subjected to the effect of concentrated loading within a patch was demonstrated and two possible methods overcoming this problem were introduced for straight Bernoulli beam: knot insertion and multiplication, and basis extension. While the first approach is suitable only for the straight beams and uses available algorithms, the method based on basis extension is a novel approach that can be modified for various beam formulations including initially curved beams.

After initial verification of the proposed method enhancing a solution on the straight Bernoulli beam formulation, the method was further extended for two-dimensional Timoshenko curved beams. The derived basis extension functions can be directly applied to the analysis of arbitrarily curved beams. The superior results were obtained proving the capability and adequacy of the proposed method. The idea of the method can also be applied to other beam formulations or approximation bases or to resolve other cases leading to the discontinuous character of the solution. The proposed method is an original contribution of the author and is considered as the major achievement of the presented work.

LIST OF FIGURES

LIST OF TABLES

REFERENCES

[1] R. Courant, Variational methods for the solution of problems of equilibrium and vibrations, Bulletin of the American Mathematical Society 49 (1943) 1–23.

[2] J. H. Argyris, S. Kelsey, Energy theorems and structural analysis, Vol. 60, Springer, 1960.

[3] P. Bézier, Definition numerique des courbes et surface, Automatisme 11 (4) (1966) 625–632.

[4] P. De Casteljau, Outillages méthodes calcul, Andr e Citro en Automobiles SA, Paris 4 (1959) 25.

[5] T. J. R. Hughes, J. A. Cottrell, Y. Bazilevs, Isogeometric analysis: CAD, finite elements, NURBS, exact geometry and mesh refinement., Comput. Methods Appl. Mech. Engrg. 194 (2005) 4135–4195.

[6] W. A. Wall, M. A. Frenzel, C. Cyron, Isogeometric structural shape optimization, Computer Methods in Applied Mechanics and Engineering 197 (33) (2008) 2976 – 2988. doi:https://doi.org/10.1016/j.cma.2008.01.025.
URL http://www.sciencedirect.com/science/article/pii/S0045782508000509

[7] I. Temizer, P. Wriggers, T. Hughes, Contact treatment in isogeometric analysis with NURBS, Computer Methods in Applied Mechanics and Engineering 200 (9) (2011) 1100 – 1112. doi:https://doi.org/10.1016/j.cma.2010.11.020.
URL http://www.sciencedirect.com/science/article/pii/S0045782510003440

[8] H. Gomez, T. J. Hughes, X. Nogueira, V. M. Calo, Isogeometric analysis of the isothermal Navier-Stokes-Korteweg equations, Computer Methods in Applied Mechanics and Engineering 199 (25) (2010) 1828 – 1840. doi:https://doi.org/10.1016/j.cma.2010.02.010.
URL http://www.sciencedirect.com/science/article/pii/S004578251000068X

[9] Y. Bazilevs, V. M. Calo, T. J. R. Hughes, Y. Zhang, Isogeometric fluid-structure interaction: theory, algorithms, and computations, Computational Mechanics 43 (1) (2008) 3–37. doi:10.1007/s00466-008-0315-x.
URL https://doi.org/10.1007/s00466-008-0315-x

[10] R. Bouclier, T. Elguedj, Locking free isogeometric formulations of curved thick beams., Comput. Methods Appl. Mech. Engrg. 245-246 (2012) 144–162.

[11] R. Echter, M. Bischoff, Numerical efficiency, locking and unlocking of NURBS finite elements., Comput. Methods Appl. Mech. Engrg. 199 (2010) 374–382.

[12] G. Zhang, R. Alberdi, K. Khandelwal, Analysis of three-dimensional curved beams using isogeometric approach., Engineering Structures 117 (2016) 560–574.

[13] L. Greco, M. Cuomo, B-spline interpolation of Kirchhoff-Love space rods, Computer Methods in Applied Mechanics and Engineering 256 (2013) 251 – 269. doi:https://doi.org/10.1016/j.cma.2012.11.017.
URL http://www.sciencedirect.com/science/article/pii/S0045782512003660

[14] A. Bauer, M. Breitenberger, B. Philipp, R. Wüchner, K.-U. Bletzinger, Nonlinear isogeometric spatial Bernoulli beam, Computer Methods in Applied Mechanics and Engineering 303 (2016) 101–127.

[15] J. Kiendl, K.-U. Bletzinger, J. Linhard, R. Wüchner, Isogeometric shell analysis with Kirchhoff-Love elements, Computer Methods in Applied Mechanics and Engineering 198 (49) (2009) 3902 – 3914. doi:https://doi.org/10.1016/j.cma.2009.08.013.
URL http://www.sciencedirect.com/science/article/pii/S0045782509002680

[16] D. Benson, Y. Bazilevs, M.-C. Hsu, T. Hughes, Isogeometric shell analysis: the Reissner–Mindlin shell, Computer Methods in Applied Mechanics and Engineering 199 (5-8) (2010) 276–289.

[17] J. Fish, T. Belytschko, A first course in finite elements, Wiley, 2007.

[18] T. Elguedj, Y. Bazilevs, V. M. Calo, T. J. Hughes, B and F projection methods for nearly incompressible linear and non-linear elasticity and plasticity using higher-order NURBS elements, Computer methods in applied mechanics and engineering 197 (33-40) (2008) 2732–2762.

[19] L. B. da Veiga, C. Lovadina, A. Reali, Avoiding shear locking for the Timoshenko beam problem via isogeometric collocation methods, Computer Methods in Applied Mechanics and Engineering 241 (2012) 38–51.

[20] F. Auricchio, L. B. Da Veiga, J. Kiendl, C. Lovadina, A. Reali, Locking-free isogeometric collocation methods for spatial Timoshenko rods, Computer Methods in Applied Mechanics and Engineering 263 (2013) 113–126.

[21] A. Cazzani, M. Malagù, E. Turco, F. Stochino, Constitutive models for strongly curved beams in the frame of isogeometric analysis, Mathematics and Mechanics of Solids 21 (2) (2016) 182–209.

[22] J. Kiendl, F. Auricchio, T. J. Hughes, A. Reali, Single-variable formulations and isogeometric discretizations for shear deformable beams, Computer Methods in Applied Mechanics and Engineering 284 (2015) 988–1004.

[23] A.-T. Luu, J. Lee, Non-linear buckling of elliptical curved beams, International Journal of Non-Linear Mechanics 82 (2016) 132–143.

[24] A. Hashemian, S. F. Hosseini, Nonlinear bifurcation analysis of statically loaded free-form curved beams using isogeometric framework and pseudo-arclength continuation, International Journal of Non-Linear Mechanics 113 (2019) 1–16.

[25] D. Vo, P. Nanakorn, A total Lagrangian Timoshenko beam formulation for geometrically nonlinear isogeometric analysis of planar curved beams, Acta Mechanica 231 (7) (2020) 2827–2847.

[26] S. Raknes, X. Deng, Y. Bazilevs, D. Benson, K. Mathisen, T. Kvamsdal, Isogeometric rotation-free bending-stabilized cables: Statics, dynamics, bending strips and coupling with shells, Computer Methods in Applied Mechanics and Engineering 263 (2013) 127–143.

[27] Z. Huang, Z. He, W. Jiang, H. Qiao, H. Wang, Isogeometric analysis of the nonlinear deformation of planar flexible beams with snap-back, Acta Mechanica Solida Sinica 29 (4) (2016) 379–390.

[28] A. Borković, S. Kovačević, G. Radenković, S. Milovanović, M. Guzijan-Dilber, Rotation-free isogeometric analysis of an arbitrarily curved plane Bernoulli–Euler beam, Computer Methods in Applied Mechanics and Engineering 334 (2018) 238–267.

[29] L. Greco, M. Cuomo, An implicit G1 multi patch B-spline interpolation for Kirchhoff–Love space rod, Computer Methods in Applied Mechanics and Engineering 269 (2014) 173–197.

[30] L. Piegl, W. Tiller, The NURBS Book, Springer-Verlag Berlin Heidelberg, New York, 1997.

[31] J. A. Cottrell, T. J. Hughes, Y. Bazilevs, Isogeometric analysis: toward integration of CAD and FEA, John Wiley & Sons, 2009.

[32] Voight notation, Voight notation — Wikipedia, the free encyclopedia, [Online] (2022).
URL `https://en.wikipedia.org/wiki/Voigt_notation`

[33] T. J. Hughes, A. Reali, G. Sangalli, Efficient quadrature for NURBS-based isogeometric analysis, Computer methods in applied mechanics and engineering 199 (5-8) (2010) 301–313.

[34] F. Auricchio, F. Calabro, T. J. Hughes, A. Reali, G. Sangalli, A simple algorithm for obtaining nearly optimal quadrature rules for NURBS-based isogeometric analysis, Computer Methods in Applied Mechanics and Engineering 249 (2012) 15–27.

[35] D. Schillinger, S. J. Hossain, T. J. Hughes, Reduced Bézier element quadrature rules for quadratic and cubic splines in isogeometric analysis, Computer Methods in Applied Mechanics and Engineering 277 (2014) 1–45.

[36] D. Rypl, B. Patzák, Object oriented implementation of the T-spline based isogeometric analysis, Advances in Engineering Software 50 (2012) 137–149.

[37] V. P. Nguyen, C. Anitescu, S. P. Bordas, T. Rabczuk, Isogeometric analysis: an overview and computer implementation aspects, Mathematics and Computers in Simulation 117 (2015) 89–116.

[38] J. A. Cottrell, A. Reali, Y. Bazilevs, T. J. Hughes, Isogeometric analysis of structural vibrations, Computer methods in applied mechanics and engineering 195 (41-43) (2006) 5257–5296.

[39] C. Adam, S. Bouabdallah, M. Zarroug, H. Maitournam, Improved numerical integration for locking treatment in isogeometric structural elements, Part I: Beams, Computer Methods in Applied Mechanics and Engineering 279 (2014) 1–28.

[40] T. J. Hughes, The finite element method: linear static and dynamic finite element analysis, Courier Corporation, 2012.

[41] T. Belytschko, W. K. Liu, B. Moran, K. Elkhodary, Nonlinear finite elements for continua and structures, John wiley & sons, 2014.

[42] E. Rank, R. Krause, K. Preusch, On the accuracy of p-version elements for the Reissner–Mindlin plate problem, International Journal for Numerical Methods in Engineering 43 (1) (1998) 51–67.

[43] S. F. Pawsey, R. W. Clough, Improved numerical integration of thick shell finite elements, International journal for numerical methods in engineering 3 (4) (1971) 575–586.

[44] O. Zienkiewicz, R. Taylor, J. Too, Reduced integration technique in general analysis of plates and shells, International Journal for Numerical Methods in Engineering 3 (2) (1971) 275–290.

[45] G. Prathap, G. Bhashyam, Reduced integration and the shear-flexible beam element, International journal for numerical methods in engineering 18 (2) (1982) 195–210.

[46] C. R. Babu, G. Prathap, A linear thick curved beam element, International Journal for Numerical Methods in Engineering 23 (7) (1986) 1313–1328.

[47] C. R. Babu, G. Subramanian, G. Prathap, Mechanics of field-consistency in finite element analysis—a penalty function approach, Computers & structures 25 (2) (1987) 161–173.

[48] C. Adam, T. J. Hughes, S. Bouabdallah, M. Zarroug, H. Maitournam, Selective and reduced numerical integrations for NURBS-based isogeometric analysis, Computer Methods in Applied Mechanics and Engineering 284 (2015) 732–761.

[49] C. Adam, S. Bouabdallah, M. Zarroug, H. Maitournam, Improved numerical integration for locking treatment in isogeometric structural elements. Part II: Plates and shells, Computer Methods in Applied Mechanics and Engineering 284 (2015) 106–137.

[50] K.-U. Bletzinger, M. Bischoff, E. Ramm, A unified approach for shear-locking-free triangular and rectangular shell finite elements, Computers & Structures 75 (3) (2000) 321–334.

[51] G. Farin, Curves and surfaces for computer-aided geometric design: a practical guide, Elsevier, 2014.

[52] Q. Hu, Y. Xia, S. Natarajan, A. Zilian, P. Hu, S. Bordas, Isogeometric analysis of thin reissner-mindlin plates and shells: locking phenomena and b-bar method, arXiv preprint arXiv:1709.00402.

[53] J. S. Dai, Euler–Rodrigues formula variations, quaternion conjugation and intrinsic connections, Mechanism and Machine Theory 92 (2015) 144–152.

[54] A. Ibrahimbegovic, Nonlinear solid mechanics: theoretical formulations and finite element solution methods, Vol. 160, Springer Science & Business Media, 2009.

[55] MATLAB, version 8.5.0 (R2015a), The MathWorks Inc., Natick, Massachusetts, 2015.

[56] B. Patzák, OOFEM—an object-oriented simulation tool for advanced modeling of materials and structures, Acta Polytechnica 52 (6).

[57] Octave - Nurbs (2021). arXiv:https://octave.sourceforge.io/nurbs/.

[58] J. W. Eaton, D. Bateman, S. Hauberg, R. Wehbring, GNU Octave version 5.2.0 manual: a high-level interactive language for numerical computations (2020). URL `https://www.gnu.org/software/octave/doc/v5.2.0/`

[59] Rhinoceros (2017). arXiv:http://www.rhino3d.com/.

[60] Grasshopper (2017). arXiv:http://www.grasshopper3d.com/.

[61] L. Svoboda, J. Novák, L. Kurilla, J. Zeman, A framework for integrated design of algorithmic architectural forms, Advances in Engineering Software 72 (2014) 109–118.

[62] Z. Bittnar, J. Šejnoha, Numerické metody mechaniky, Vol. 1, Vydavatelství ČVUT, 1992.

[63] E. Dvořáková, B. Patzák, Isogeometric bernoulli beam element with an exact representation of concentrated loadings, Computer Methods in Applied Mechanics and Engineering 361 (2020) 112745.

[64] T. Belytschko, T. Black, Elastic crack growth in finite elements with minimal remeshing, International journal for numerical methods in engineering 45 (5) (1999) 601–620.

[65] N. Moës, J. Dolbow, T. Belytschko, A finite element method for crack growth without remeshing, International journal for numerical methods in engineering 46 (1) (1999) 131–150.

[66] D. J. Benson, Y. Bazilevs, E. De Luycker, M.-C. Hsu, M. Scott, T. Hughes, T. Belytschko, A generalized finite element formulation for arbitrary basis functions: from isogeometric analysis to XFEM, International Journal for Numerical Methods in Engineering 83 (6) (2010) 765–785.

[67] I. Babuška, J. M. Melenk, The partition of unity method, International journal for numerical methods in engineering 40 (4) (1997) 727–758.

[68] R. Gracie, H. Wang, T. Belytschko, Blending in the extended finite element method by discontinuous Galerkin and assumed strain methods, International Journal for Numerical Methods in Engineering 74 (11) (2008) 1645–1669.

[69] E. Dvořáková, B. Patzák, Isogeometric Timoshenko curved beam element with an enhanced representation of concentrated loadings, Computers & Structures (submitted).

APPENDIX

A

EXTENSION FUNCTIONS

A.1. General definitions

$$\begin{aligned} \bar{s}_F &= s_F/L \\ \bar{s} &= s/L \\ f' &= \frac{df}{d\bar{s}} \end{aligned} \tag{A.1}$$

A.2. Function with discontinuous 1^{st} derivative

$$\begin{aligned} a &= 1 \\ b &= a\bar{s}_F/(\bar{s}_F - 1) \\ C_1 &= 0 \\ D_1 &= a\bar{s}_F - b\bar{s}_F \end{aligned} \tag{A.2}$$

for $\bar{s} \in (0, \bar{s}_F)$

$$\begin{aligned} R^* &= a\bar{s} + C_1 \\ R^{*\prime} &= a \end{aligned} \tag{A.3}$$

for $\bar{s} \in (\bar{s}_F, 1)$

$$\begin{aligned} R^* &= b\bar{s} + D_1 \\ R^{*\prime} &= b \end{aligned} \tag{A.4}$$

A.3. Function with discontinuous 2^{nd} derivative

$$\begin{aligned} a &= 0 \\ b &= 1 \\ C_1 &= b\bar{s}_F - a\bar{s}_F - b/2 + a\bar{s}_F^2/2 - b\bar{s}_F^2/2 \\ C_2 &= 0 \\ D_1 &= a\bar{s}_F^2/2 - b/2 - b\bar{s}_F^2/2 \\ D_2 &= b\bar{s}_F^2/2 - a\bar{s}_F^2/2 \end{aligned} \tag{A.5}$$

for $\bar{s} \in (0, \bar{s}_F)$

$$\begin{aligned} R^* &= a\bar{s}^2/2 + C_1\bar{s} + C_2 \\ R^{*\prime} &= a\bar{s} + C_1 \end{aligned} \tag{A.6}$$

for $\bar{s} \in (\bar{s}_F, 1)$

$$\begin{aligned} R^* &= b\bar{s}^2/2 + D_1\bar{s} + D_2 \\ R^{*\prime} &= b\bar{s} + D_1 \end{aligned} \tag{A.7}$$

A.4. Function with discontinuous 3^{rd} derivative

$$\begin{aligned} a &= 0 \\ b &= 1 \\ C_1 &= b\bar{s}_F - a\bar{s}_F - b/3 + a\bar{s}_F^2 - a\bar{s}_F^3/3 - b\bar{s}_F^2 + b\bar{s}_F^3/3 \\ C_2 &= 0 \\ C_3 &= 0 \\ D_1 &= a\bar{s}_F^2 - b/3 - a\bar{s}_F^3/3 - b\bar{s}_F^2 + b\bar{s}_F^3/3 \\ D_2 &= b\bar{s}_F^2/2 - a\bar{s}_F^2/2 \\ D_3 &= a\bar{s}_F^3/6 - b\bar{s}_F^3/6 \end{aligned} \tag{A.8}$$

for $\bar{s} \in (0, \bar{s}_F)$

$$\begin{aligned} R^* &= as^3/6 + C_1s^2/2 + C_2s + C3 \\ R^{*\prime} &= as^2/2 + C_1s + C_2 \end{aligned} \tag{A.9}$$

for $\bar{s} \in (\bar{s}_F, 1)$

$$\begin{aligned} R^* &= bs^3/6 + D_1s^2/2 + D_2s + D_3 \\ R^{*\prime} &= bs^2/2 + D_1s + D_2 \end{aligned} \tag{A.10}$$

A.5. Function with discontinuous 4^{th} derivative

$$\begin{aligned} a &= 0 \\ b &= 1 \\ C_1 &= b\bar{s}_F - a\bar{s}_F - b/2 + a\bar{s}_F^3 - a\bar{s}_F^4/2 - b\bar{s}_F^3 + b\bar{s}_F^4/2 \\ C_2 &= b/12 + a\bar{s}_F^2/2 - 2a\bar{s}_F^3/3 + a\bar{s}_F^4/4 - b\bar{s}_F^2/2 + 2b\bar{s}_F^3/3 - b\bar{s}_F^4/4 \\ C_3 &= 0 \\ C_4 &= 0 \\ D_1 &= a\bar{s}_F^3 - b/2 - a\bar{s}_F^4/2 - b\bar{s}_F^3 + b\bar{s}_F^4/2 \\ D_2 &= b/12 - 2a\bar{s}_F^3/3 + a\bar{s}_F^4/4 + 2b\bar{s}_F^3/3 - b\bar{s}_F^4/4 \\ D_3 &= a\bar{s}_F^3/6 - b\bar{s}_F^3/6 \\ D_4 &= b\bar{s}_F^4/24 - a\bar{s}_F^4/24 \end{aligned} \tag{A.11}$$

for $\bar{s} \in (0, \bar{s}_F)$

$$\begin{aligned} R^* &= as^4/24 + C_1s^3/6 + C_2s^2/2 + C_3s + C_4 \\ R^{*\prime} &= as^3/6 + C_1s^2/2 + C_2s + C_3 \end{aligned} \tag{A.12}$$

for $\bar{s} \in (\bar{s}_F, 1)$

$$\begin{aligned} R^* &= bs^4/24 + D_1s^3/6 + D_2s^2/2 + D_3s + D_4 \\ R^{*\prime} &= bs^3/6 + D_1s^2/2 + D_2s + D_3 \end{aligned} \tag{A.13}$$

A.6. Function with discontinuous 5^{th} derivative

$$
\begin{aligned}
a &= 0; \\
b &= 1; \\
C_1 &= b\bar{s}_F - a\bar{s}_F - 2b/5 + 2a\bar{s}_F^3 - 2a\bar{s}_F^4 + 3a\bar{s}_F^5/5 - 2b\bar{s}_F^3 + 2b\bar{s}_F^4 - 3b\bar{s}_F^5/5 \\
C_2 &= b/20 + a\bar{s}_F^2/2 - a\bar{s}_F^3 + 3a\bar{s}_F^4/4 - a\bar{s}_F^5/5 - b\bar{s}_F^2/2 + b\bar{s}_F^3 - 3b\bar{s}_F^4/4 + b\bar{s}_F^5/5 \\
C_3 &= 0 \\
C_4 &= 0 \\
C_5 &= 0 \\
D_1 &= 2a\bar{s}_F^3 - 2b/5 - 2a\bar{s}_F^4 + 3a\bar{s}_F^5/5 - 2b\bar{s}_F^3 + 2b\bar{s}_F^4 - 3b\bar{s}_F^5/5 \\
D_2 &= b/20 - a\bar{s}_F^3 + 3a\bar{s}_F^4/4 - a\bar{s}_F^5/5 + b\bar{s}_F^3 - 3b\bar{s}_F^4/4 + b\bar{s}_F^5/5 \\
D_3 &= a\bar{s}_F^3/6 - b\bar{s}_F^3/6 \\
D_4 &= b\bar{s}_F^4/24 - a\bar{s}_F^4/24 \\
D_5 &= a\bar{s}_F^5/120 - b\bar{s}_F^5/120
\end{aligned}
\tag{A.14}
$$

for $\bar{s} \in (0, \bar{s}_F)$

$$
\begin{aligned}
R^* &= as^5/120 + C_1 s^4/24 + C_2 s^3/6 + C_3 s^2/2 + C_4 s + C_5 \\
R^{*\prime} &= as^4/24 + C_1 s^3/6 + C_2 s^2/2 + C_3 s + C_4
\end{aligned}
\tag{A.15}
$$

for $\bar{s} \in (\bar{s}_F, 1)$

$$
\begin{aligned}
R^* &= bs^5/120 + D_1 s^4/24 + D_2 s^3/6 + D_3 s^2/2 + D_4 s + D_5 \\
R^{*\prime} &= bs^4/24 + D_1 s^3/6 + D_2 s^2/2 + D_3 s + D_4
\end{aligned}
\tag{A.16}
$$